공학박사학위논문

Soft Morphing Textile Actuators using Shape Memory Effect

형상 기억 효과를 활용한 소프트 모핑 섬유 구동기

2017 년 8 월

서울대학교 대학원

기계항공공학부

한 민 우

Soft Morphing Textile Actuators using Shape Memory Effect

형상기억효과를 활용한 소프트 모핑 섬유 구동기

지도교수 안 성 훈

이 논문을 공학박사 학위논문으로 제출함

2017년 5월

서울대학교 대학원
기계항공공학부
한 민 우

한민우의 공학박사 학위논문을 인준함

2017년 6월

위 원 장 : 김종원

부위원장 : 안 성훈

위 원 : 차 석원

위 원 : 조 규진

위 원 : Hugo Rodrigue

Abstract

Soft Morphing Textile Actuators using Shape Memory Effect

Han, Min-Woo
Department of Mechanical and Aerospace Engineering
The Graduate School
Seoul National University

Soft morphing structures execute biologically inspired motions more effectively through flexible body mechanisms than conventional rigid-bodied structures. Their softness and compliance allow them to mimic muscle-like biological locomotion and possess many degrees of freedom, compared with rigid bodies. To demonstrate the morphing in various modes, including three-dimensional (3D) volumetric transformation, textile actuators are presented based on woven and knitted structures.

First, a woven type smart soft composite (SSC) consisting of shape memory alloy (SMA) wires and a glass fiber-reinforced composite was introduced for generating a large deformation using the inherent properties of woven textiles. The embedded SMA wires were divided into independently controlled groups to create asymmetrical bending through unequal power input and/or current feed times. By controlling the power input, symmetric/asymmetric actuation modes were achieved.

To determine the characteristics of the woven SSCs, different configurations of the composite were tested in terms of the diameters of the SMA wires, numbers of embedded SMA wires, and numbers of glass-fiber fabric lamina. The proposed woven type SSC was implemented as the trailing edge of a spoiler on a small ($\frac{1}{8}$)-scale car and as variable winglets of an unmanned aerial vehicle. To confirm their aerodynamic performance, wind tunnel experiments were conducted under various wind speeds, angles of attack, and actuation modes of the soft morphing wings.

Second, to demonstrate the morphing in various modes, including 3D volumetric transformation, a smart morphing knit was developed that was made from a thermally responsive fiber, allowing the creation of 3D morphologies with no auxiliary materials or an elastomeric matrix. A knitting method was used in the manufacturing process of the smart textile structure, and four combinations of loop patterns (plan, garter, rib, and seed patterns) were used to explore a variety of morphing shapes. Open and closed geometries of 14 knitting structures were used to characterize their morphing behaviors. Using the knitting methods, morphing flowers (a lily-like, a daffodil-like, a gamopetalous, and a calla-like flower) were fabricated and their blooming motion was demonstrated by controlling the current to actuate the petals selectively.

Keywords: Smart soft composite actuator, Smart textile, Soft robot, Artificial muscle, Shape memory alloy, Biomimetic actuator, Morphing wing, Soft exosuit

Student Number: 2013-30954

Table of Contents

Chapter 3. Applications of woven actuators 48

Chapter 4. Smart morphing knit...108

List of Figures

List of Table

Chapter 1.

Introduction

1.1. Actuators for morphing systems

Morphing is a proposed technology used to adapt shape to diverse operational conditions without discrete parts [1]. Generally, morphing technology has been applied to aerospace applications that are affected by fluidic forces because it can reduce the efficiency loss of a fluid by continuous shape changing. Not limited to aerospace applications, however, biomimetic robot applications, such as an inch worm robot and robot fish, have been developed using the advantages of morphable structures [2].

To make better use of morphing adaptability, smart materials have been introduced as an alternative to ‘conventional’ actuators. They permit an integrated approach to meet multi-disciplinary requirements and a continuous surface during actuation without discrete sections, as well as reduce the complexity of the actuating system and generation of curvilinear motion, which require convoluted elements in engineering design [3-5].

One of the major approaches is to create adaptable structures using piezoelectric materials. Schultz *et al.* reported a bistable asymmetric composite laminate, operated by bonded piezoelectric actuators; a Rayleigh–Ritz technique was applied to the model [3]. A two-dimensional theory for a multilayered piezoelectric shell was investigated by Ossadzow-David *et al.* [4], including the displacements and electrostatic potential at the layer interfaces and boundary conditions. Kogl *et al.* [5] proposed a topological optimized design of piezoelectric actuators in multiple lamina of plate/shell structures; a piezoelectric material model was developed based on solid isotropic material with penalization.

An alternative to using piezoelectric materials is to use shape memory alloy (SMA) elements with a morphable structure via external attachment or embedding of the SMA within the structure. Lee *et al.* [6] presented a saddle-shaped morphing panel actuated by implementation of a SMA spring actuator; a Rayleigh–Ritz approximation was used to investigate the proposed mechanism. SMA-embedded hybrid composite actuators have been investigated with soft composites to generate non-discrete deformation, which corresponds to biomimetic motions [7-9]. Bending behaviors of an E-glass/epoxy composite [10] and an epoxy matrix composite [11], subjected to a SMA-embedded composite in a longitudinal direction, were characterized experimentally. Buckling and postbuckling behaviors of the SMA-embedded laminated composite were analyzed considering the external and thermal loads on the composite by Lee *et al.* [12]. A soft morphing actuator capable of pure twisting motion [13, 14] and multiple mode of actuation [15, 16] using a pair of SMA wires embedded in a composite were investigated with regard to achieving complicated movements by actuating the multiple SMA wires selectively. To derive a coupling effect for in-plane/bending/twisting deformations, an anisotropic materials-embedded composite, a smart soft composite (SSC), was proposed by Ahn *et al.* [17]. Its use as a fast-bending actuator capable of realizing large deformation [18] was developed based on coupling effects from three-dimensional (3D) deformation. Also, there have been attempts to derive multifunctional properties using SMA materials for health monitoring systems [19], stiffness control [20], and shape retention without additional energy after deformation [21, 22] as well as using actuators capable of producing deformations.

1.2. Soft morphing actuators

Soft robotics has attempted to emulate numerous nature-inspired characteristics through mechanical systems, such as flexible and compliant motions. To demonstrate the nature-inspired flexible motions capable of 3D volumetric transformations, including bending, twisting, and torsional deformation, soft morphing technologies have been proposed. Soft morphing allows smooth and continuous deformations to change a structural configuration by adjusting environmental conditions. Properties required of soft morphing actuators include the following:

- Soft materials-based
- Autonomous
- Largely deformable
- Reversible

The soft morphing concept makes it possible to explore applications in the field of soft robotics, for example, fiber-based composites used in aerospace and automobile applications, soft exosuits, and nature-inspired robots. Figure

1-1 shows several examples of soft morphing actuators and robots. ("Soft morphing" terminology reference: Choi *et al.*, Fundamental Technology for Biomimetic Soft Morphing, 2009.)

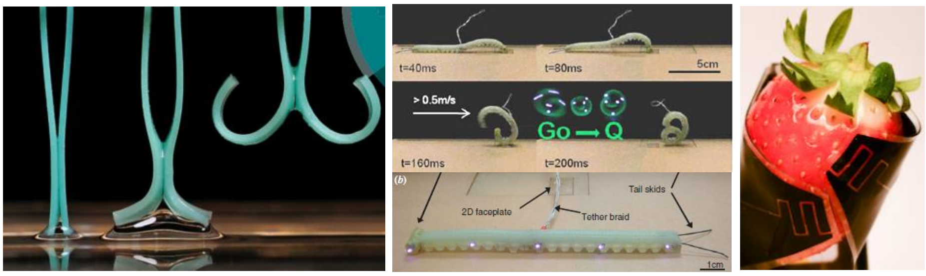

Elastocapillarity gripper
(Boston Univ., Prof. D.P. Holmes's group, 2016)

GoQBot
(Tufts Univ., Prof. B. Trimmer's group, 2011)

Soft DEA gripper
(EPFL, Prof. H. Shea's group, 2016)

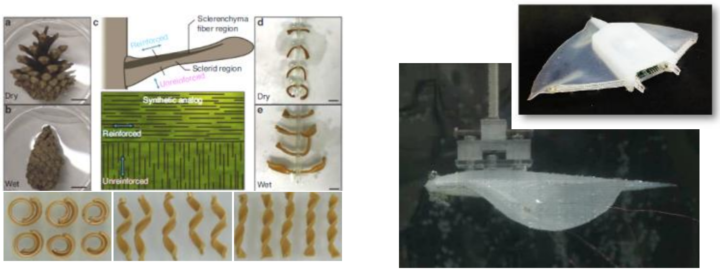

Self-shaping composites
(ETH Zurich, Prof. Andre's group, 2013)

Ray robot
(SNU, Prof. Ahn's group, 2016)

Figure 1-1. Soft morphing actuators and robots

1.3. Textile platform-based actuators

Textiles show high resilience and elasticity, in that they return to their original form after bending, twisting, or even crushing. Also, they show high flexibility, and can be flexed repeatedly without being ruptured. There are many types of textile manufacturing; representative cases include weaving and knitting. Both are readily mass producible and widely used.

To offer added-value functionality to a fabric, smart materials capable of performing dynamic behavior are combined with conventional static fibers. Smart textiles have multifunctional properties that enable sensing, adapting, and reacting to the surrounding environment. In a different way, to perform multifunctional properties based on textile platform, an external source (e.g., pneumatic, hydraulic, or smart-material sources) can be attached or linked to the passive textile platform. Figure 1-2 shows textile platform-based actuators.

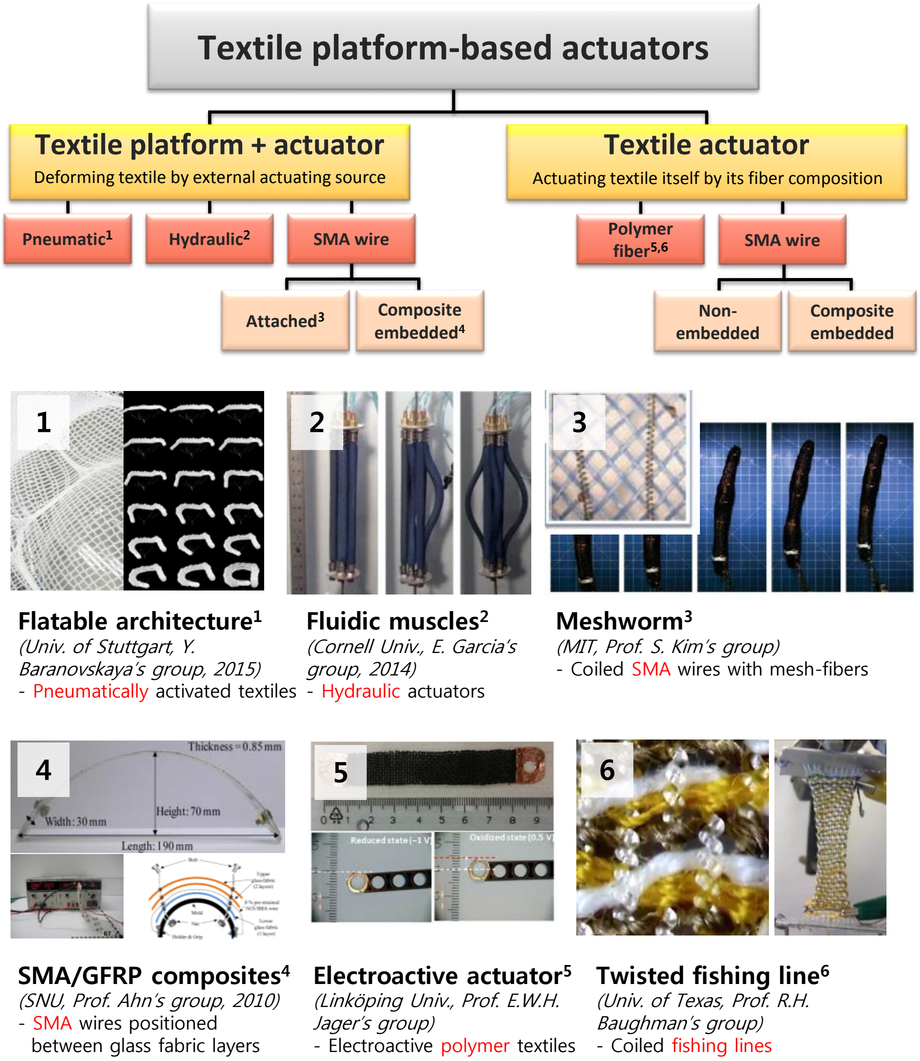

Flatable architecture[1]
(Univ. of Stuttgart, Y. Baranovskaya's group, 2015)
- Pneumatically activated textiles

Fluidic muscles[2]
(Cornell Univ., E. Garcia's group, 2014)
- Hydraulic actuators

Meshworm[3]
(MIT, Prof. S. Kim's group)
- Coiled SMA wires with mesh-fibers

SMA/GFRP composites[4]
(SNU, Prof. Ahn's group, 2010)
- SMA wires positioned between glass fabric layers

Electroactive actuator[5]
(Linköping Univ., Prof. E.W.H. Jager's group)
- Electroactive polymer textiles

Twisted fishing line[6]
(Univ. of Texas, Prof. R.H. Baughman's group)
- Coiled fishing lines

Figure 1-2. Textile platform-based actuators

1.4. Textile manufacturing technologies

Textiles are defined as any product manufactured from fibers, filaments, or yarns. Weaving and knitting are major processes, accounting for approximately 70% of textile production.

Woven structures show strong, high-density, and stable properties, which can allow stable deformation even with thin structures. Woven-based actuators can be used to generate shell-like deformation, such as in morphing skins. In this research, soft morphing wings for transportation were developed using woven-type SSC actuators, which require a lightweight and simple structure to reduce the mass of vehicles, thereby increasing aerodynamic performance.

Knitted structures can have highly stretchable properties, which can be used for making complex shapes. Knitted structure-based actuators have the potential to generate complex and varied modes of deformation and are, thus, advantageous in the field of soft robotic applications, such as nature-inspired systems and soft exo-suits. The types of textile manufacturing technologies are shown in Figure 1-3.

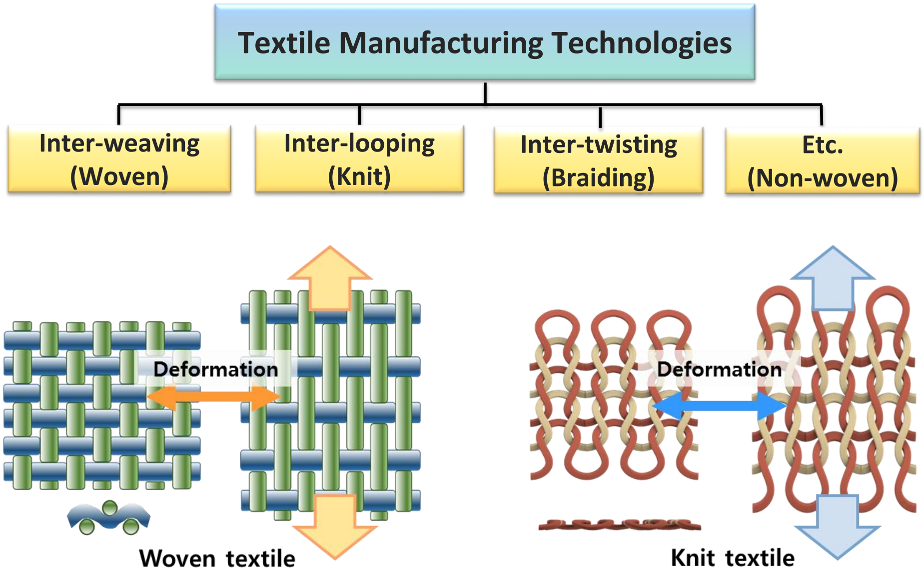

Figure 1-3. Types of textile manufacturing technologies

1.5. Goals of this research

The goal of this research is to develop soft morphing actuators using smart textile composites to achieve morphing actuation. Two types of actuators with different textile designs, woven and knitted, are used to carry out different actuation properties and applications.

To improve previous woven-based actuators, SMA-embedded woven composites are presented, made by weaving SMA wires and glass fibers together. The embedded SMA wires are divided into independently controlled groups to create asymmetrical bending through unequal power input and/or current feed times. By controlling the power input, symmetric/asymmetric actuation modes are achieved. Also, to determine the characteristic of the woven SSC, differing configurations of the composite are tested in terms of the diameters of SMA wires, numbers of embedded SMA wires, and numbers of glass-fiber fabric lamina.

Additionally, a new method for a soft morphing structure is presented, in which loop-linked structures made from functional fibers allow the creation of 3D morphologies, including flowers. Based on the design methodology of loop patterning, the proposed morphing structures enable 3D volumetric transformations, including bending, twisting, and torsional deformation, through reconfiguration of the loop geometries. A knitting method, in which yarn loops are used to create subsequent loops, is used in the manufacture of a smart textile structure. Each of the knitting patterns, which originate from common methods used in the textile industry, demonstrates unique capabilities in generating deformations.

Chapter 2.

Woven type smart soft composite actuators*

2.1. Design

The woven type SSC consists of a glass fiber-reinforced smart actuator made from commercially available SMA wires (Ni: 55 wt%, Ti: 45 wt%; Dynalloy, Inc.) and glass fibers interwoven using a plain weave method. The SMA wires were used as an actuator to realize the deformation of the structure, and the anisotropic properties of the glass fibers were used for controlling the direction of the deformation by changing the disposition of the embedded fibers.

To fabricate the woven type SSC, the SMA wires were first positioned on the loom in the lengthwise direction, and then glass fibers were interwoven perpendicularly with the SMA wires. The fabricated woven structure was then

---

*Chapter 2 and 3 were published as regular articles:

[1] Han, M.-W., et al., 2016, "Woven type Smart Soft Composite for Soft Morphing Car Spoiler," Compos. Part B-Eng., Vol. 86, pp. 285-298.

[2] Han, M.-W., et al., 2016, "Shape Memory Alloy/Glass Fiber Woven Composite for Soft Morphing Winglets of Unmanned Aerial Vehicles," Compos. Struct., Vol. 140, pp. 202-212.

[3] Han, M.-W., et al., 2014, "Design and Performance Evaluation of Soft Morphing Car-spoiler," ASME IDETC/CIE 2014.

[4] Han, M.-W., 2013, "Fabrication of Morphing Structure using Woven type Smart Soft Composite," Master thesis, Seoul National University.

[5] Han, M.-W., et al., 2017, "Behavior of Fiber-Reinforced Smart Soft Composite Actuators According to Material Composition," Trans. Korean Soc. Mech. Eng. A, Vol. 41, No. 2, pp. 81-85.

combined with PDMS (Sylgard 184, Dow Corning), a soft polymer with isotropic properties, and cured in a temperature-controllable oven. Before curing the composite structure, additional layers of glass-fiber fabric were layered on the woven structure such that the SMA-embedded active layer was positioned eccentrically from the neutral plane. The behavior characteristics of the SSC structure are affected by the stacking order, number, and orientation of the glass-fiber fabric and woven layers, and allows for modifying the mechanical properties and deformation quantity of the actuator to achieve a desired performance. Figure 2-1 shows the concept of the woven type SSC, and the typical material properties of the glass fiber and the PDMS are shown in Table 1 and Table 2.

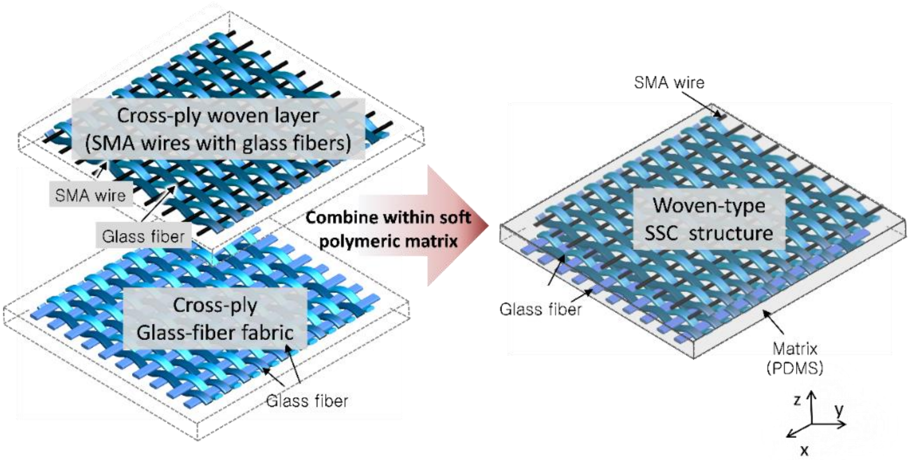

Figure 2-1. Conceptual diagrams of woven type SSC

Table 1. Material properties of the glass fiber (E-glass fiber, KPI Co., Ltd)

Parameter	Value (Unit)
Tensile strength	1470 MPa
Specific gravity	2.54
Max. elongation	4 %
Softening point	846 ℃

Table 2. Material properties of the PDMS (sylgard 184, Dow corning)

Parameter	Value (Unit)
Young’s modulus	1.84 MPa
Tensile strength	6.7 MPa
Specific gravity (when cured)	1.03
Density	965 kg/m^3

2.2. Materials and fabrication

2.2.1. Active component

To generate a deformation of the woven type SSC, SMA wires are used by applying electric currents selectively to SMA wires embedded in the soft matrix. The use of SMA as an actuator is advantageous in implementing complicated movements that demand lightweight, large force, and a simple system. In particular, soft or compliant actuators based on non-traditional materials, including SMA, have been developed to achieve novel motions that have been of particular interest for morphing applications [7, 23, 24].

The SMA wires can be contracted in their axial direction through Joule heating and then relaxed by cooling them. When the SMA wires are heated over the phase transformation temperature, a contractile force is generated which deforms the surrounding matrix. After the SMA wire cools down to below the phase transformation temperature, the structure recovers its original shape due to the elastic recovery force of the structure. In this case, the woven type SSC uses the thermal shape memory effect of SMA in two reversible stable phases, austenite and martensite, during actuation. Because the microstructural arrays are rearranged during the phase transition, the mechanical properties of SMA including the yield strength and the Young's modulus are altered [25-28].

Figure 2-2 shows the structural variations in SMA caused by external loading and temperature. Using the contraction and restoration of the SMA wires, the structure in which the SMA wires are embedded undergoes a deformation which is affected by the eccentricity of the SMA wires in the matrix, meaning that the SMA wires are positioned at a certain distance from the neutral plane of the structure.

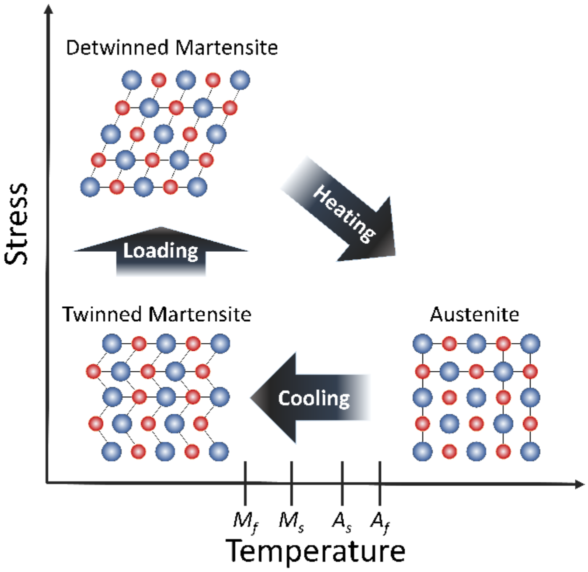

Figure 2-2. Phase transformation of SMA (M_f: Martensite finish temperature, M_s: Martensite start temperature, A_s: Austenite start temperature, A_f: Austenite finish temperature)

2.2.2. Fabrication

The morphing shell is composed of woven structures and soft polymeric matrix. At first, two sets of threads (SMA wires as warp threads and glass fibers as weft threads) are interlaced each other, which the warp threads are fixed at the loom in longitudinally and the weft threads pass through in laterally. The raising and lowering sequence with the position of the warp threads determined the types of the weaving structure. In this case, plain weave method was used which possessing for strong and low stretchable properties by aligning the warp and weft threads in a criss-cross pattern. This woven fabric is layered with the additional woven fabrics, and the stacking conditions are following required modes of actuation. The laminate is placed between release films for the vacuum bag molding process after the PDMS of mixing ratio of 10:1 base to curing agent is degassed and poured into the woven fabrics. Finally, the assembly is cured at a temperature of 50℃ for 10 hours (Figure 2-3).

The vacuum bag molding process allows for producing a quality composite by applying a vacuum pressure at the resin and reinforcements. The following refinements can be taken as a result of this process: Impregnation a liquefied PDMS into the woven fabric uniformly, elimination air pockets during curing process, a smooth and even surface, ratio control of resin and fabrics, higher adhesion between layers, and reinforcement concentrations of the specimen.

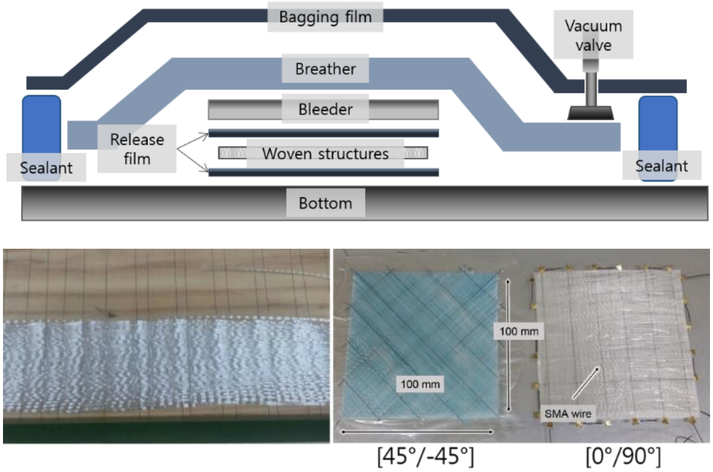

Figure 2-3. Fabrication of the morphing shell; (a) smart woven fabric composed of SMA wires and glass fibers, (b) Conceptual view of the vacuum bag molding process, (c) Soft morphing shells of [0/90], [-45/45]

Using the machinery system, the woven structures are made with different fiber compositions (Figure 2-4). The woven machine makes mass production possible in a high quality woven structures. Warp or weft threads can be selectable following design parameters. The magnified view of the woven structure and fabricated woven structures with different threads compositions are shown in figure 2-5.

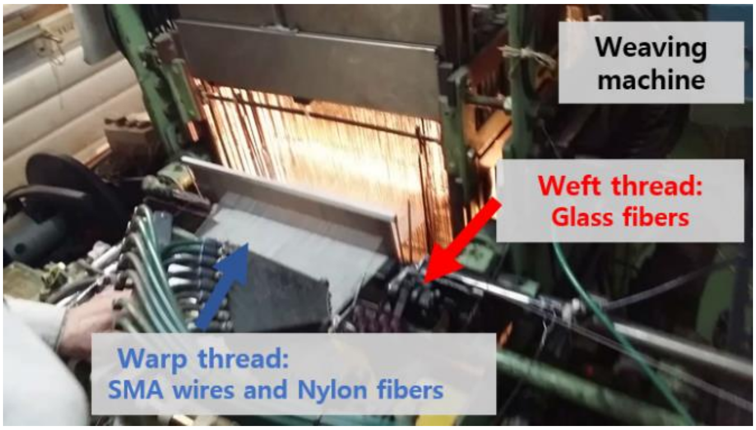

Figure 2-4. Fabrication of woven structure using machine

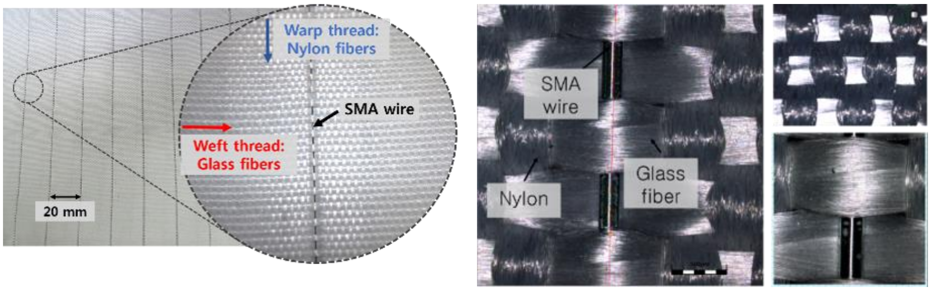

(a) Magnified view of woven structure

(b) Woven structure
(Warp: SMA wire/Glass-fiber,
Weft: Glass-fiber)

(c) Woven structure
(Warp: SMA wire/Nylon fiber
Weft: Glass-fiber)

Figure 2-5. Fabricated woven structures using machine

2.3. Beam-type soft actuators

2.3.1. Deformation behavior

A parametric study of the woven type SSC was conducted using beam-shaped specimens. Specimens were fabricated by layering glass-fiber fabric onto the woven structure and then embedded in a PDMS matrix. One to five additional layers of glass-fiber fabric were embedded into the matrix as shown in Figure 2-6, in order to investigate the effect of the number of layers on the performance of the structure. A single SMA wire was used in the middle of the first layer of a beam (dimension: 84 mm X 11 mm). For each number of layer, specimens were built with various SMA wires sizes ranging from 200 µm to 500 µm in order to see the correlation between these two factors. Furthermore, different types of weaving methods (plain and satin) were used to make the woven type SSC with various fiber compositions.

The results of the bending test are shown in figure 2-7. For structures with one additional glass-fiber fabric layer, SMA wires with diameters of 200 µm provided the largest bending deformation producing a tip angle of around 390 degrees. With an increase in the number of glass-fiber fabric layers, the bending deformation was also decreased. The actuator with 400 µm SMA wires produced the largest deformation for structures with two to five layers of glass-fiber fabric. However, for the structure with five layers of glass-fiber fabric, the bending deformation nearly converged for all SMA wire diameters. In case of the different types of weaving methods, the plain woven actuator consisting of the warp threads of SMA wire and nylon-fiber while the weft threads of glass-fiber provided the largest bending deformation (Figure 2-7(b)). Also, the angle of the additional layer which is layered on the SMA woven structure was rotated to generate a bend-twist deformation intended to make coupling deformation in a single structure. The largest deformation with pure bending mode was measured for the 45 angled specimen and the bend-twist deformation was generated for the 30 and 60 angled specimen (Figure 2-7(c)).

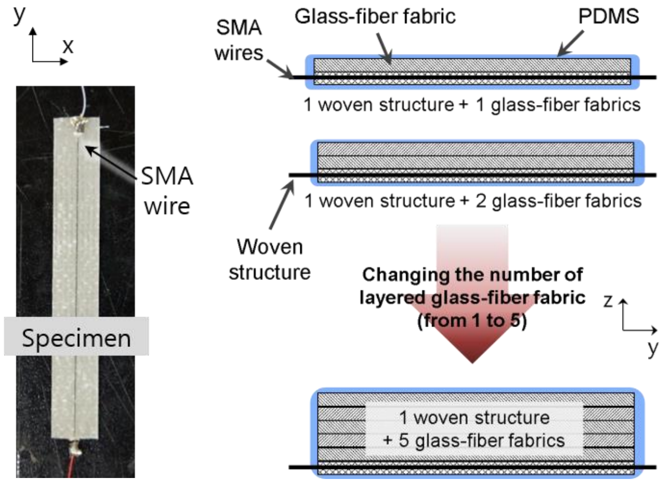

(a) Beam-shape actuator with different layers of glass-fiber fabric

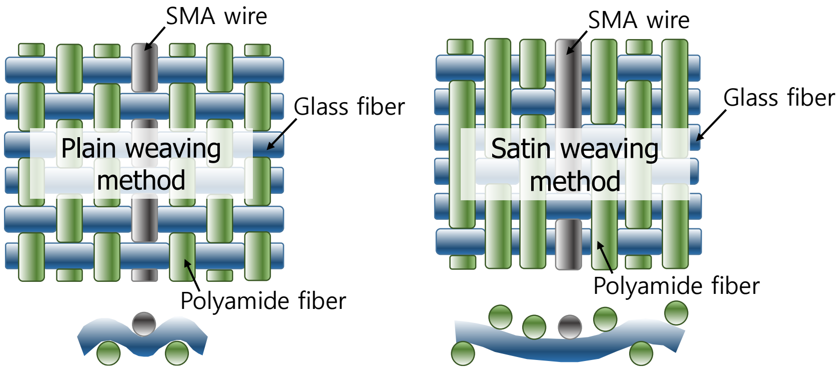

(b) Different types of woven textiles

Figure 2-6. Beam-shape specimen for parametric test

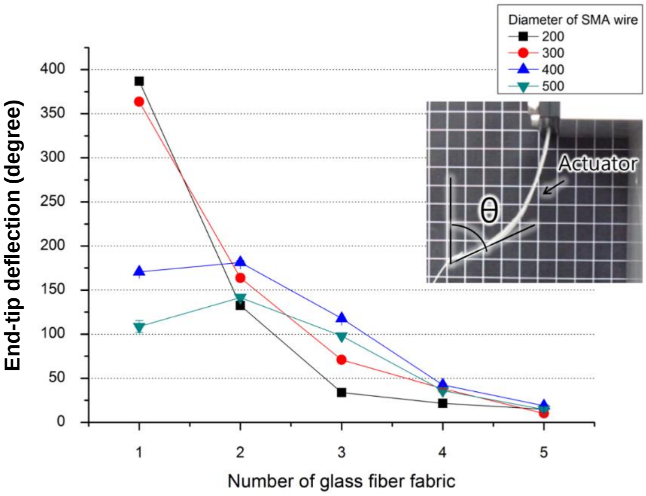

(a) Bending test with different SMA diameters and the number of glass-fiber fabric layers (Plain weaving : warp is SMA wire and weft is glass-fibers)

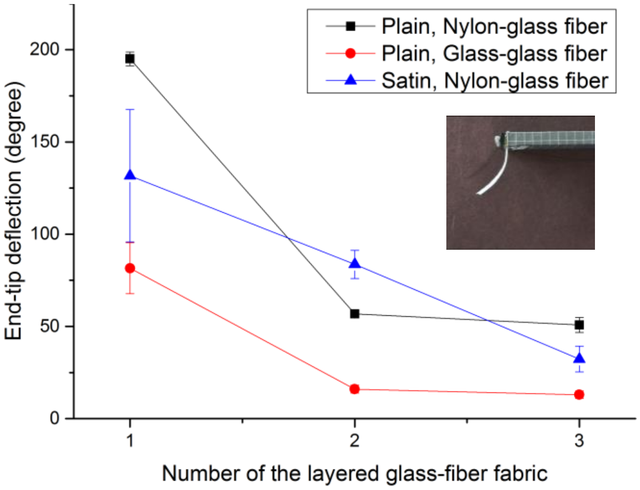

(b) Bending test with various weaving methods (Black line : Plain weaving with warp threads of SMA/Nylon-fibers and weft threads of glass-fibers, Red line : Plain weaving with warp threads of SMA/Glass-fibers and weft threads of glass-fibers, Blue line : Satin weaving with warp threads of SMA/Nylon-fibers and weft threads of glass-fibers)

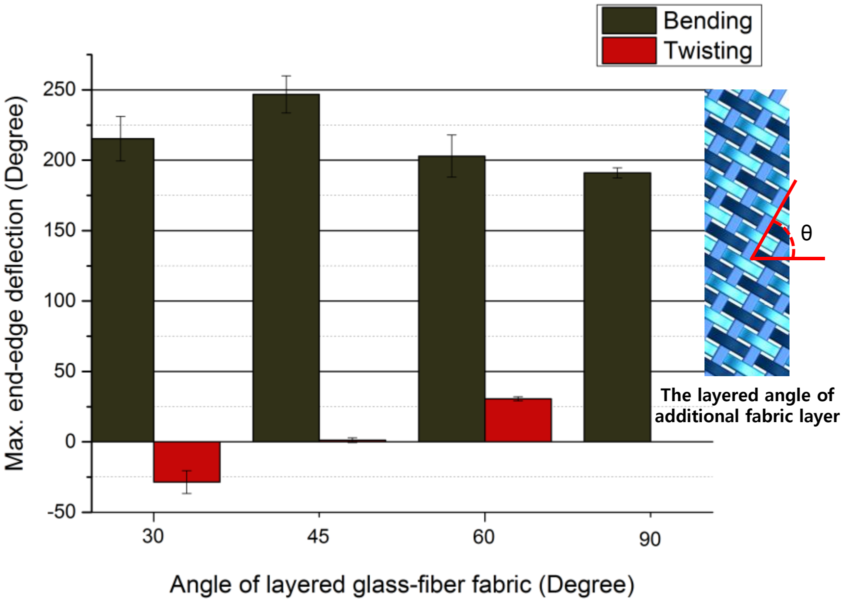

(c) Bending test with different layered angle of additional fabric layer (Plain weaving with warp threads of SMA/Nylon-fibers and weft threads of glass-fibers)

Figure 2-7. Results of bending test of the beam-shape woven type SSC

The thermally activated behavior of the SMA wires was initiated by applying a current to heat the SMA wires for transforming the phase of the alloy. To observe the maximum end-edge deflection and the time to a fully deformed state following resistive heating with different currents, one end of the woven

SSC actuator was anchored at room temperature. Figure 2-8(a) shows the end-edge deflection as a function of the current. In these tests, when I = 0.5 A, the final deflected angle was approximately 10% of the maximum deformation of the actuator. Larger currents generated larger angles of the end-edge deflection, which plateaued at approximately 400° when I = 1.0 A. The response time to reach the saturated deflection with actuation current is shown in Figure 2-8(b).

Figure 2-9 shows the temperature–time curves for the 30-mm beam actuator at room temperature. In these measurements, the current was switched off when the actuator became saturated in the deformed state. The peak temperatures correspond to the surface temperature when the actuator reached maximum deformation in the range of $I \geq 0.7$ A. For the ranges of the currents, the maximum end-edge deflection did not increase even when the current was applied to further raise the temperature. For currents $I \leq 0.6$ A, the actuators remained at that level for the states of plateau temperature by continuing to supply current to generate the more deflection; however, the temperature did not show any significant further increase, and nor did the deflection. In case of the cooling response of the actuators, it was similar in all cases. Figure 2-10 shows the heating and cooling sequences of the actuator with a current of 1.0 A.

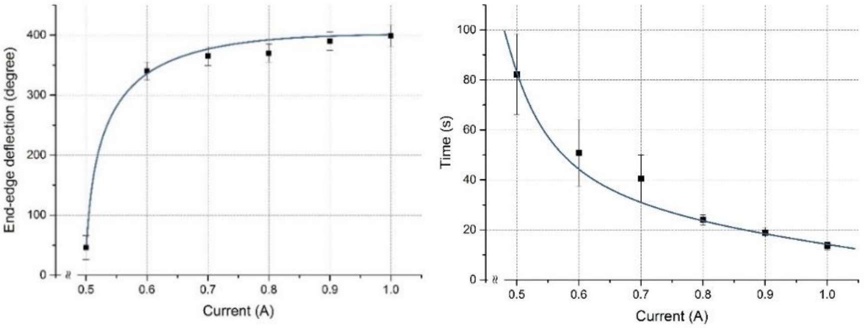

(a) End-edge deflection as a function of the current

(b) The time to reach a fully deformed state as a function of the current

Figure 2-8. Deformation behaviors of woven SSC actuator

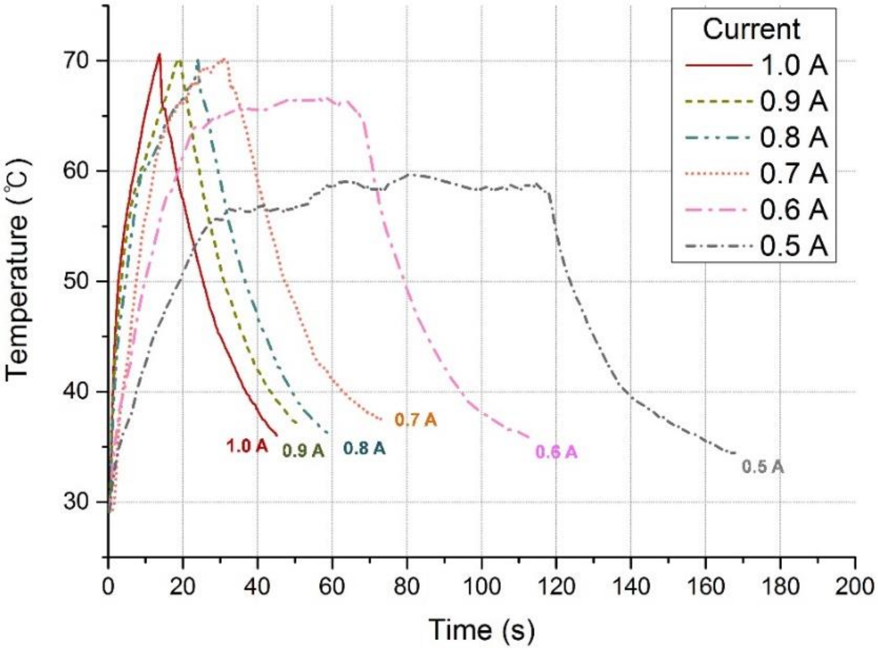

Figure 2-9. Surface temperature of the woven SSC actuator as a function of the time, where Joule heating was used to deform the SMA wire with currents in the range of 0.5–1.0 A

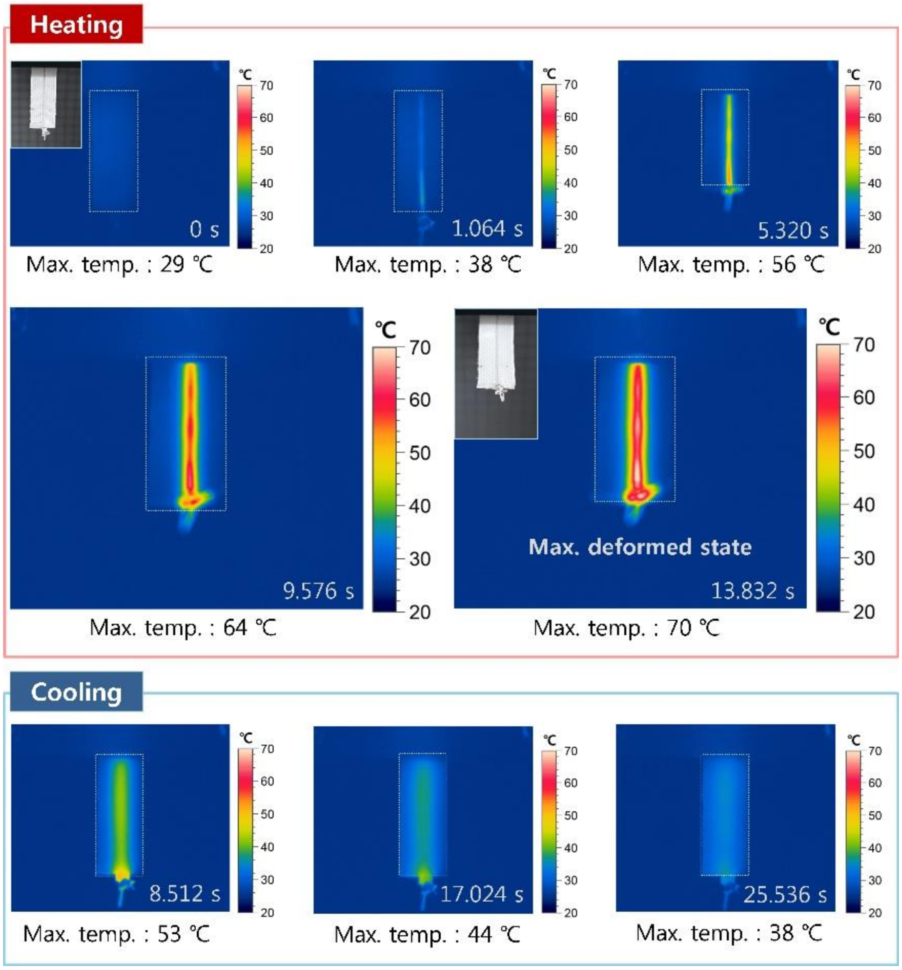

Figure 2-10. Time-series images showing the heating and cooling of the surface of woven SSC actuator with a current of 1.0 A

2.3.2. Blocking force

The actuating force for the beam-shape specimens was measured using the experimental setup shown in Figure 2-11. The specimen was fixed at the top of an acrylic wall on one side and the dynamometer (Type 9256C1, Kistler) on the other side without interval space to minimize the deformation of the actuator.

The actuating force of each sample was measured 5 times and the results are shown in Figure 2-12. The results show that larger SMA wire diameters produced a larger actuating force, with a maximum actuating force of about 6.6 N for the 500 µm SMA wire with 3 layers of glass-fiber fabric. However, the actuating force decreased sharply with additional layers of glass-fiber fabric in case of specimens with 500 µm SMA. Also, when the woven actuators were made with different types of fiber compositions, a maximum actuating force was measured for the fiber combinations of warp threads of SMA and nylon-fibers and weft threads of glass-fibers (Figure 2-12(b)).

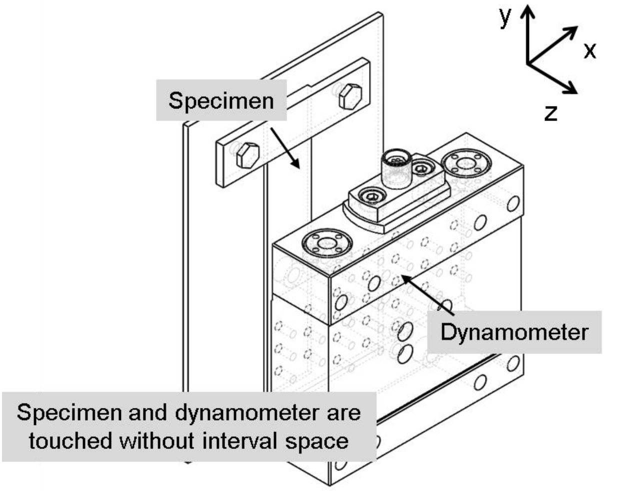

Figure 2-11. Experimental set-up of force measurement

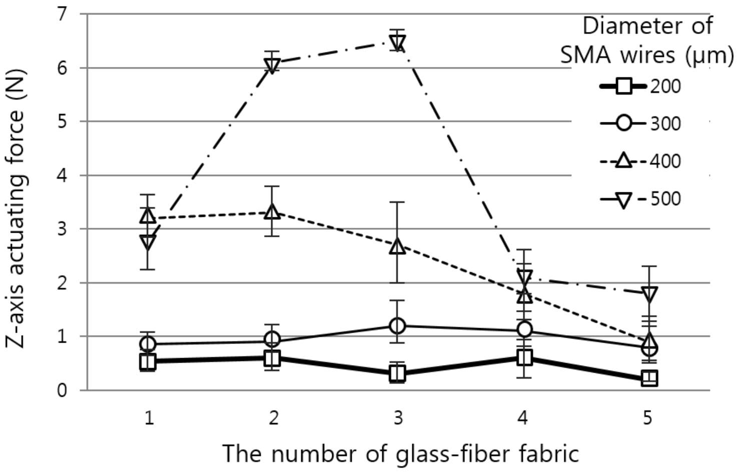

(a) Blocking force test with different SMA diameters and the number of glass-fiber fabric layers (Plain weaving : warp is SMA wire and weft is glass-fibers)

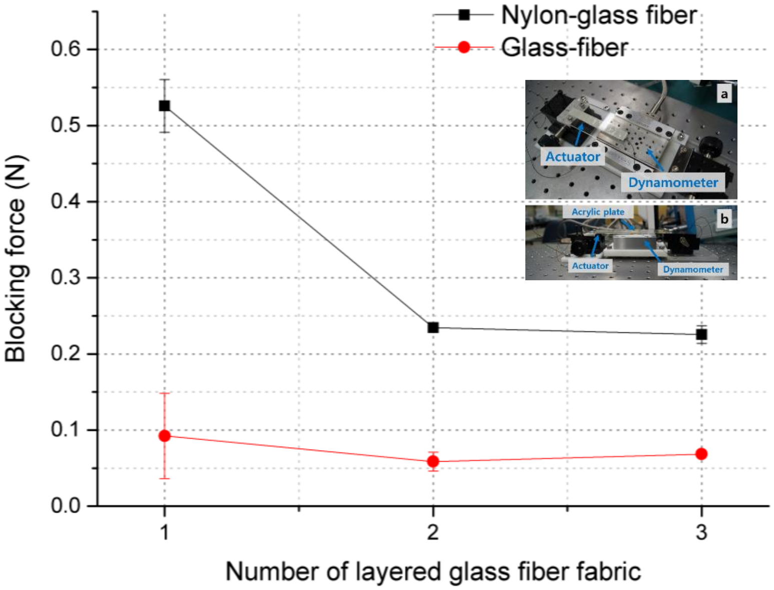

(b) Blocking force test with different types of weaving fibers (Black line : Plain weaving with warp threads of SMA/Nylon-fibers and weft threads of glass-fibers, Red line : Plain weaving with warp threads of SMA/Glass-fibers and weft threads of glass-fibers)

Figure 2-12. Results of force measurement of the beam-shape woven type SSC

2.3.3. Mechanical properties and analysis

To determine the flexural stress-stiffness of the actuator, woven SSC beams with different configurations were investigated using three-point bending tests. For the experiments, actuators were prepared with span lengths of 25.4 mm, and cross-sectional dimensions of 12 mm × 1 mm. The flexural behavior of the composite beams was investigated for various diameters of embedded

SMA wire ranging from 200 μm to 500 μm, and with the number of stacked layers of glass fiber fabric ranging from 1 to 5. A universal testing machine (5948 Microtester, Instron, US) with a three-point flexure fixture (2810-400, Instron, US) was used to test the specimens in a monotonical loading speed. Each test was carried out following the ASTM D790-03 standard with a strain rate of 0.1 mm/mm/min. The flexural stress at the midpoint was calculated as follows considering the deflection of the beam during tested exceeds 10% of the support span:

$$\sigma_f = \left(\frac{3PL}{2bd^2}\right)\left[1 + 6\left(\frac{D}{L}\right)^2 - 4\left(\frac{d}{L}\right)\left(\frac{D}{L}\right)\right] \qquad (1)$$

where P is the load at a given point on the load–deflection curve (N), L is the support span (mm), b is the width of the beam (mm), d is the depth of the tested beam (mm), and D is the deflection of the centerline of the specimen at the middle of the support span (mm).

The flexural strain in response to the nominal fractional change in the length of the outer surface of the beam at the midpoint was calculated as follows:

$$\epsilon_f = \left(\frac{6Db}{L^2}\right) \qquad (2)$$

Figure 2-13(a) shows the test results with the flexural stress and strains in the beam calculated using equations 1 and 2 respectively. For a given strain, the flexural stress increased as the number of layers of glass fiber and the diameter of the SMA wires increased. Figure 2-13(b) shows the flexural stress at 5% strain for each of the actuators. With 200-μm-diameter SMA wires for five layers of glass fiber fabric, the flexural stress at 5% strain was 27.94 MPa, which represents an increase of 1860% compared with a single layer of glass fiber fabric incorporating 200-μm-diameter SMA wires (1.43 MPa). With a single layer of glass fiber fabric, the flexural stress increased from 1.43 MPa to 3.50 MPa as the diameter of the SMA wire increased from 200 μm to 500 μm (an increase of approximately 245%). During the experiments, none of the specimens yielded or failed before the 5% strain limit.

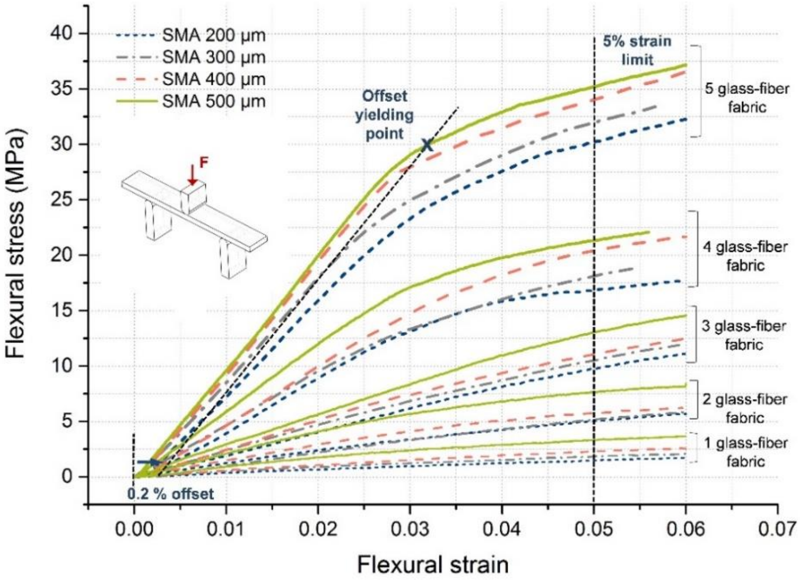

(a) Flexural stress–strain curves of the woven SSC with various diameters of SMA wires and various numbers of layers of glass fiber fabric

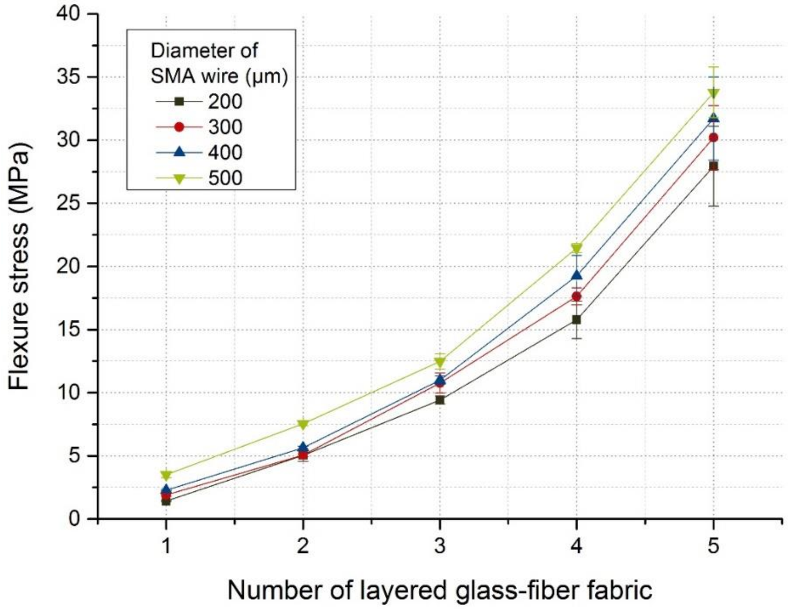

(b) Flexural stress at 5% strain as a function of the number of layered glass fiber fabric and of the diameter of the SMA wires

Figure 2-13. Flexural properties of the woven SSC

Several analytical modeling methods have been reported to calculate the strain of a composite actuator [16, 22, 29-32]. Because the soft actuator undergoes large deformation upon phase change of the SMA, an SMA-based soft composite model was used to calculate the direction and magnitude of the deformation [22, 29-31]. Figure 2-14 shows a schematic diagram of the operating principle of the woven SSC.

The constitutive relationship for the SMA actuator includes the strain, phase fraction of martensite, and thermal expansion. The relationship can be expressed as follows:

$$\sigma - \sigma_0 = E(\varepsilon - \varepsilon_0) + \Omega(\xi - \xi_0) + \Theta(T - T_0) \qquad (3)$$

where σ is the stress, E is the Young's modulus, ε is the strain, Ω is the transformation coefficient, ξ is the martensite fraction within the SMA, Θ is the thermoelastic coefficient, and T is the temperature in the SMA. Using this relationship, we can determine the strain as follows by assuming zero initial stress, a negligible thermoelastic coefficient, and a fully phase-transformed state ($\xi - \xi_0 = 0 - 1$) [22, 31]:

$$\varepsilon = \frac{EI\varepsilon_i}{E_A A_{SMA} h^2 - EI} \qquad (4)$$

where E_A is the elastic modulus of the SMA when in the austenitic state, A_{SMA} is the cross-sectional area of the SMA wire, and *EI* is the bending stiffness of the actuator.

From the results of the three-point bending tests, the physical properties of the woven SSC (including Young's modulus) were calculated for various diameters of SMA and numbers of layers of glass fiber fabric. Using the values obtained from the experiments, the deformation angle can be calculated with equation 5.

$$\Delta\theta = \frac{\Delta\varepsilon\ell_i}{h} \qquad (5)$$

where ℓ_i is the length of the actuator and h is the distance between the SMA wire and the neutral plane of the actuator.

For a structure with multiple embedded SMA wires, an analytical model based on the transfer matrix method for flexible beams can be used [29, 30]. The moment generated by multiple fully actuated SMA wires was calculated as follows:

$$M_{act} = nfh \qquad (6)$$

where n is the number of SMA wires and f is the actuation force of each wire. In this approach, the actuator is divided into *N* segments, in which each segment is an infenetisimal compared with the total length of the beam where the sum of all infenetisimal lengths gives the magnitude of the deformation for the entire beam. The load vector at a local node *i* is given by

$$x_i(x_i) = \left[P_i(x_i), V_{y(i)}(x_i), V_{Z(i)}(x_i), M_{x(i)}(x_i), M_{y(i)}(x_i), M_{z(i)}(x_i), 1\right]^T$$

(7)

where $P_i(x_i)$ is the axial force on the i-th node, $V_{y(i)}(x_i)$ and $V_{Z(i)}(x_i)$ are the transverse loads in the local Y and Z directions on the i-th node, respectively, and $M_{x(i)}(x_i), M_{y(i)}(x_i)$ and $M_{z(i)}(x_i)$ are the moments in the local X, Y, and Z directions on the i-th node. Using the load vector, we can calculate $\frac{\mathrm{d}v_i}{\mathrm{d}x_i}$ at the end nodes of the beam elements as follows:

$$\frac{\mathrm{d}v_i}{\mathrm{d}x_i}(0) = -\frac{\ell_i}{3}\frac{\mathrm{d}^2 v_i}{\mathrm{d}x_i^2}(0) - \frac{\ell_i}{6}\frac{\mathrm{d}^2 v_i}{\mathrm{d}x_i^2}(\ell_i) \qquad (8)$$

$$\frac{\mathrm{d}v_i}{\mathrm{d}x_i}(\ell_i) = \frac{\ell_i}{6}\frac{\mathrm{d}^2 v_i}{\mathrm{d}x_i^2}(0) + \frac{\ell_i}{3}\frac{\mathrm{d}^2 v_i}{\mathrm{d}x_i^2}(\ell_i) \qquad (9)$$

where v_i is the elastic deformation caused by loading the beam.

From the calculated values of $\frac{\mathrm{d}v_i}{\mathrm{d}x_i}(0)$ and $\frac{\mathrm{d}v_i}{\mathrm{d}x_i}(\ell_i)$, the behavior of the beam can be obtained in terms of the elastic rotation angle with the updated rotational transformation matrix. Figure 2-15 shows the results of the calculations and the experiments for the woven SSC beam actuators where one SMA wire was embedded in a structure with different diameters of SMA wires and various numbers of layers of glass fiber fabric.

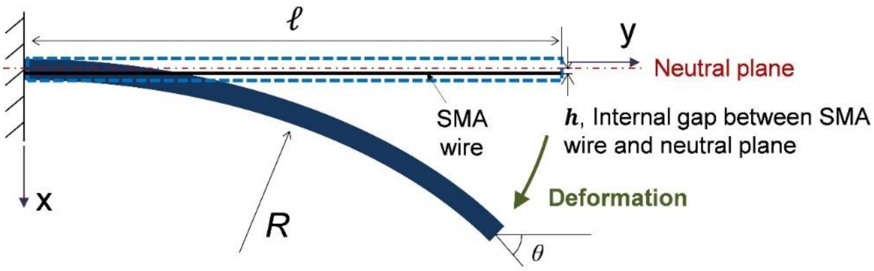

Figure 2-14. Schematic diagram of the woven SSC

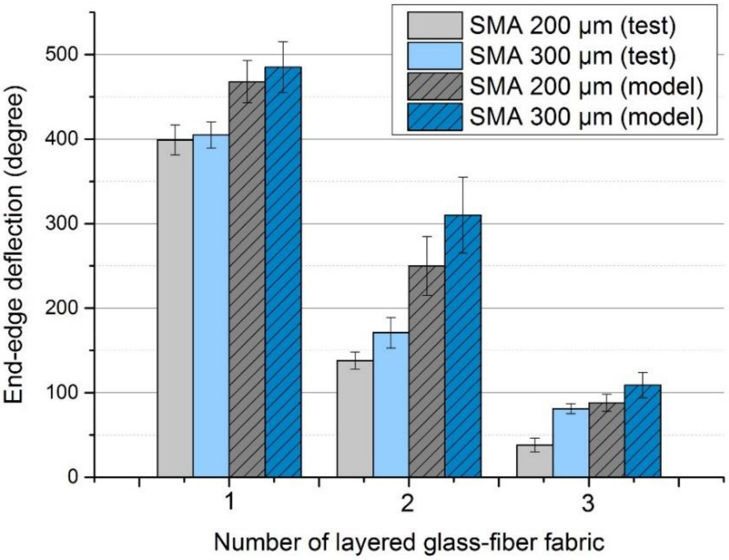

Figure 2-15. End-edge deflection of the woven SSC actuator

2.4. Shell-type soft actuators

2.4.1. Concept and design

The design for the soft morphing shell is that of the woven type smart soft composite enabling implementation of the achievement of the multistable deformed state and the adaptable morphing in large area with fabric type smart materials. The woven structures consists of the smart materials and the engineering fibers by woven together, and those are embedded in an elastomer to possess capabilities both of retaining the original shape and elastic restoring force against the actuating direction. In this work, SMA wires with a diameter of 200 μm are woven with glass-fibers for making smart weaving fabric which is that of the warp threads (SMA wires) and weft threads (glass fibers). The fabricated woven structures are embedded in a polydimethylsiloxane (PDMS) and the process of vulcanization including vacuum, which is the process of creating the PDMS into a stable solid state, are conducted for making soft morphing shell.

The main purpose of the woven structures used in this research is that of a multistable morphing shell capable of soft deformation with changeable deformation characteristic depends on which SMA wires are actuated. By using different combinations to compose composite shells, the actuation behaviors such as the mode, direction, and an amount of deformation could be generated. The characteristics of the described morphing shells are determined by the layering factors; the orientation of each woven layers, the sequence of the layered woven layers, the number of woven layers, and the composing elements of the woven layer; the number of SMA wires, the woven direction of the SMA wires and glass fibers, the volume fraction of the glass fibers in one woven structure. Figure 2-16(a) shows the multistable morphing by actuating SMA wires selectively, and the concept of the multilayered woven shell is shown in Figure 2-16(b).

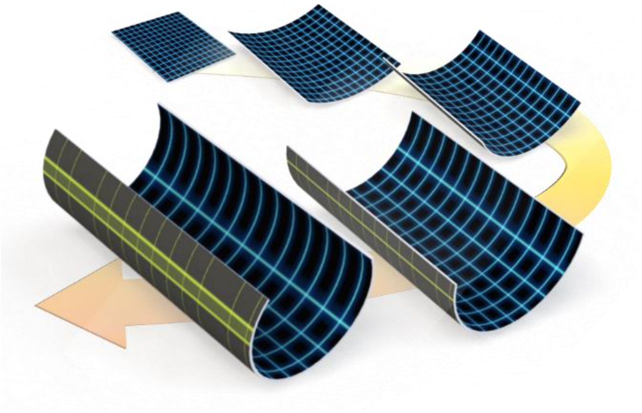

(a) Multistable morphing by actuating SMA wires selectively

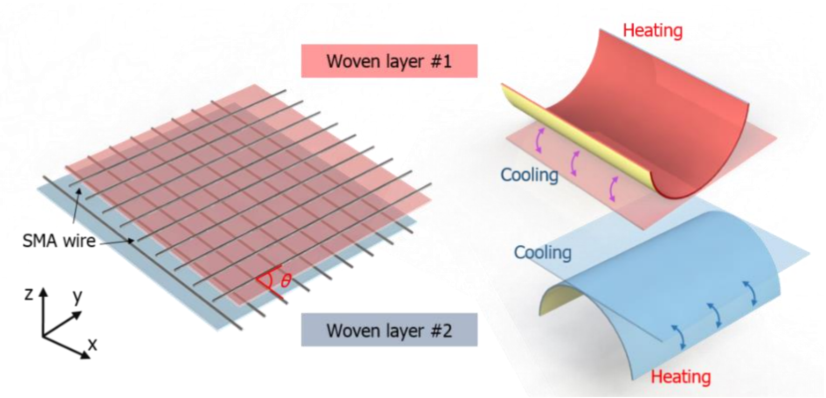

(b) Conceptual views of the soft morphing shell

Figure 2-16. Concepts of soft morphing shell

2.4.2. Theoretical analysis

The Young's modulus of the unidirectional fiber reinforced composites depends on the embedded fiber orientation. In order to study on the variations of the Young’s modulus in different fiber angles, the theoretical analysis was conducted. The total strain is related to the stress and the stiffness matrix, given as

$$\sigma = \boldsymbol{D}\varepsilon$$

Assuming the composites as a transverse isotropy material, the transformed stiffness matrix with different orientation of fibers is derived as follows

$$\sigma' = \boldsymbol{T_1}(\alpha)\sigma$$

$$\varepsilon' = \boldsymbol{T_2}(\alpha)\varepsilon$$

$$\boldsymbol{D}' = \boldsymbol{T_1}(\alpha)\boldsymbol{D}\boldsymbol{T_2^{-1}}(\alpha)$$

$$\begin{Bmatrix} \varepsilon_{11} \\ \varepsilon_{22} \\ \varepsilon_{33} \\ \gamma_{12} \\ \gamma_{13} \\ \gamma_{23} \end{Bmatrix} = \begin{bmatrix} 1/E_t & -v_{pt}/E_p & -v_{pt}/E_t & 0 & 0 & 0 \\ -v_{tp}/E_t & 1/E_p & -v_p/E_p & 0 & 0 & 0 \\ -v_{tp}/E_t & -v_p/E_p & 1/E_p & 0 & 0 & 0 \\ 0 & 0 & 0 & 1/G_t & 0 & 0 \\ 0 & 0 & 0 & 0 & 1/G_t & 0 \\ 0 & 0 & 0 & 0 & 0 & 1/G_p \end{bmatrix} \begin{Bmatrix} \sigma_{11} \\ \sigma_{22} \\ \sigma_{33} \\ \sigma_{12} \\ \sigma_{13} \\ \sigma_{23} \end{Bmatrix}$$

where the subscript of *p* and *t* describe the in-plane and transverse, v is the poisson’s ratio, *G* is the shear modulus, and *E* is the Young’s modulus. On the assumption that the composite is a transversely isotropy material, which is symmetric about the normal to an isotropic plane, the material parameters are given as $E_t = E_{11} > E_{22} = -E_{33} = -E_P$. Using relations between the elastic and shear constants for homogeneous isotropic materials, which is $G_P = E_P/2(1 + v_P)$, and transformation matrix $\boldsymbol{T_1}(\alpha)$ and $\boldsymbol{T_2^{-1}}(\alpha)$.

$$\boldsymbol{T_1}(\alpha) = \begin{bmatrix} \cos^2\alpha & \sin^2\alpha & 0 & \sin 2\alpha & 0 & 0 \\ \sin^2\alpha & \cos^2\alpha & 0 & -\sin 2\alpha & 0 & 0 \\ 0 & 0 & 1 & 0 & 0 & 0 \\ -\frac{1}{2}\sin 2\alpha & \frac{1}{2}\sin 2\alpha & 0 & \cos 2\alpha & 0 & 0 \\ 0 & 0 & 0 & 0 & \cos\alpha & \sin\alpha \\ 0 & 0 & 0 & 0 & -\sin\alpha & \cos\alpha \end{bmatrix}$$

$$\boldsymbol{T_2^{-1}}(\alpha) = \begin{bmatrix} \cos^2\alpha & \sin^2\alpha & 0 & -\frac{1}{2}\sin 2\alpha & \sin 2\alpha & 0 \\ \sin^2\alpha & \cos^2\alpha & 0 & \frac{1}{2}\sin 2\alpha & -\sin 2\alpha & 0 \\ 0 & 0 & 1 & 0 & 0 & 0 \\ \sin 2\alpha & -\sin 2\alpha & 0 & \cos 2\alpha & 0 & 0 \\ 0 & 0 & 0 & 0 & \cos\alpha & -\sin\alpha \\ 0 & 0 & 0 & 0 & \sin\alpha & \cos\alpha \end{bmatrix}$$

The three-dimensional and phenomenological model for the constitutive SMA model has been presented. The shape memory effect of the SMA, which is responded the temperature change between the austenite and martensite phase, exhibits a large residual strain. From the Liang's constitutive model for the SMA behaviors, the constitutive relation is given as under assumptions that all material functions are constants,

$$\sigma_{SMA} - \sigma_{0,SMA} = \beta\left(\varepsilon_{SMA} - \varepsilon_{0,SMA}\right) + \Omega(\xi - \xi_0) + \varphi(T - T_0)$$

where β is the modulus function of the SMA material, Ω is the transformation tensor, φ is the thermal coefficient related with the SMA expansion, and ξ is the martensite fraction factor. Assuming the phase transformation from the initial conditions of $\left(\sigma_{0,SMA} = \varepsilon_{0,SMA} = \xi_0 = 0\right)$ to the final conditions of $(\sigma_{SMA} = 0,\ \varepsilon_{SMA} = \varepsilon_{L,SMA},\ \xi = 1)$ is occurred by perfect transforming from the austenite to the detwinned martensite ($\xi = 0$ to $\xi = 1$), the transformation tensor relationship is derived as

$$\Omega = -\varepsilon_{L,SMA}\beta$$

The empirical model for the transformation from martensite to austenite can be described by

$$\xi = \frac{\xi_0}{2}\left\{\cos\left[\alpha_A\left(T - A_S - \frac{\sigma_{SMA}}{C_A}\right)\right] + 1\right\}$$

$$\text{for } C_A\left(T - A_f\right) < \sigma_{SMA} < C_A(T - A_S)$$

The material constants C_A describes the relationship of temperature and the critical stress, which is assumed to be a continuously constant value over all ranges of temperature and α_A is given as

$$\alpha_A = \pi/\left(A_f - A_S\right)$$

For the unit beam element of the morphing shell, the end-edge deflection can be define as follows with assumption of an Euler beam behavior.

$$\Delta L_m / L = F_{SMA} / E_m A_m$$

$$\theta / (L_m - \Delta L_m) = F_{SMA} d / E_m I_m$$

where ΔL_m is the axial contraction, E_m is the elastic modulus of the morphing actuator, A_m is the cross-sectional area, I_m is the moment of area moment of the morphing actuator. During actuation, the morphing actuator is assumed to be a circular geometry with holding the SMA wire at an original position with the force concentration for bending deformation regardless of the shear, torsional, and axial deformation.

2.4.3. Actuation evaluation

For measurement of the three-dimensional surface morphing, a motion capture system with video cameras. The motion capture system collects a data from 8 Vicon cameras with 250 fps to trace along the trajectories of 8 reflective markers attached on the morphing shell. 8 reflective markers are mounted on the half of the specimen since it is assuming that the morphing direction and quantity are symmetry diagonally across the center of the morphing shell. The center of the morphing shell is fixed with the rigid bar and applied currents through the embedded SMA wires. Figure 2-17 shows the experimental setup for measuring the morphing performance and figure 2-18 shows the results of deformation.

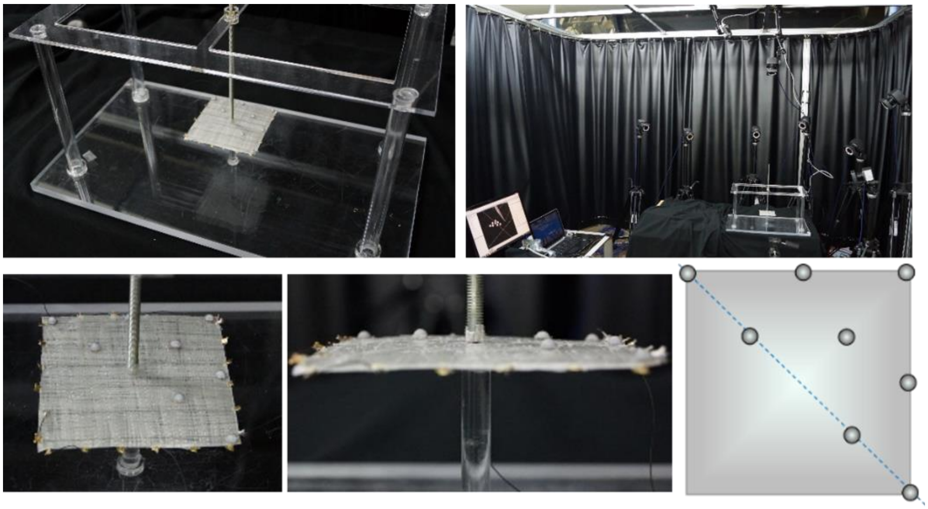

Figure 2-17. Experimental setup for measuring the morphing performance

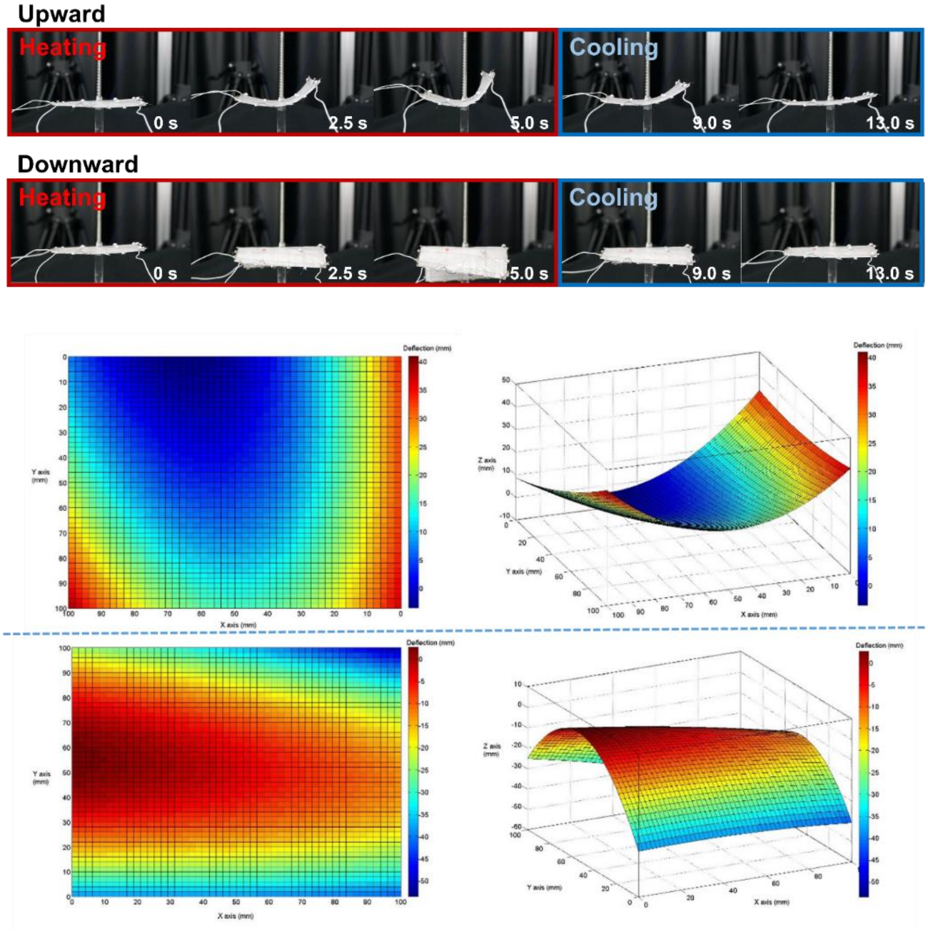

(a) [0/90] morphing shell

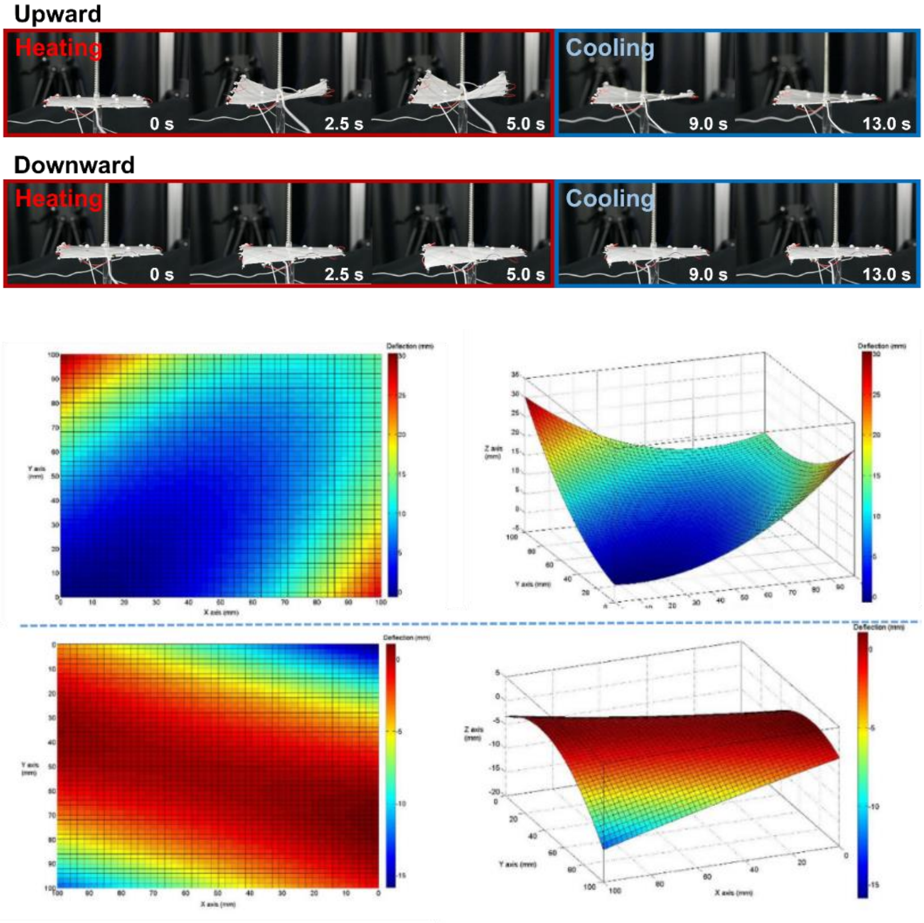

(b) [45/-45] morphing shell

Figure 2-18. Deformation results of the morphing shell

Also, a parametric study of the woven type SSC was conducted using shell-shaped specimens. The actuator consists of different individual laminas of the glass-fiber fabric that are embedded in a polymeric matrix. To characterize its deformation behavior, the composition of the actuator was changed by changing the matrix material and the number of the glass-fiber fabric layers.

In addition, current of various magnitudes were applied to each actuator to study the effect of the heating of SMA wires on applying current. The specimen and results of the bending test are shown in figure 2-19 and 2-20. For structures with one additional glass-fiber fabric layer embedded in a PDMS matrix, the soft actuator provided the largest bending deformation producing a tip angle of around 145 degrees by applying the current of 0.9 A.

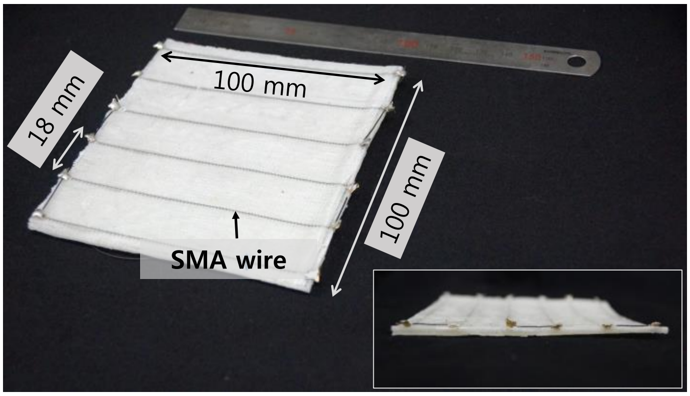

(a) Shell-type smart soft composite actuator

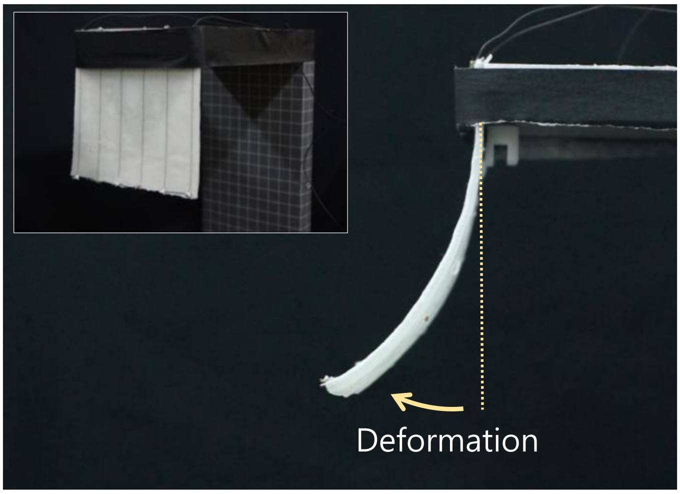

(b) End-edge deflection of shell-type actuator

Figure 2-19. Shell-type smart soft composite actuator and its end-edge deflection achieved by the embedded SMA actuation

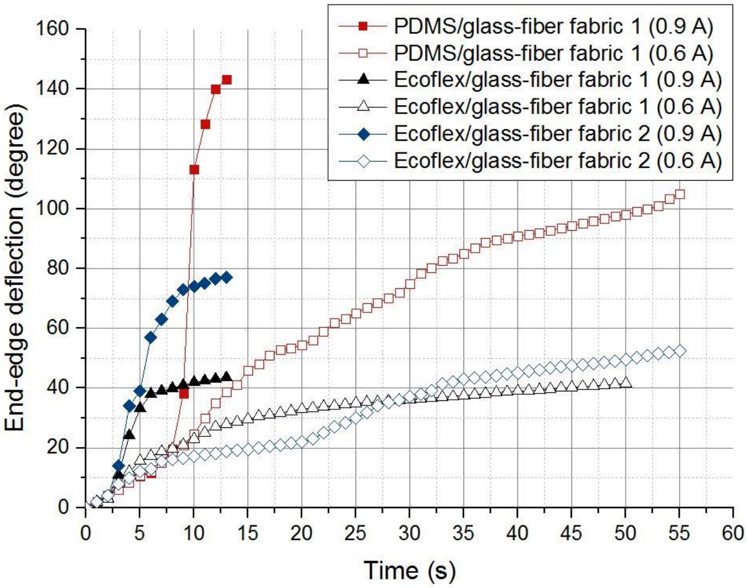

(a) End-edge deflection by heating of the SMA wires

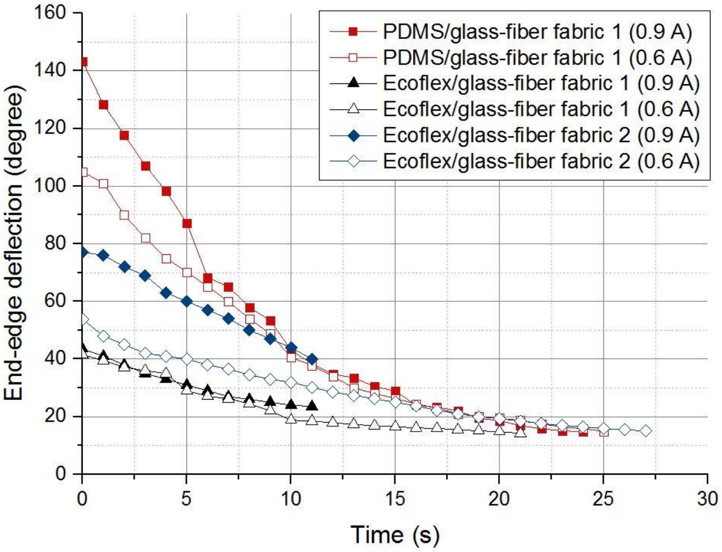

(b) Recovery by cooling of the SMA wires

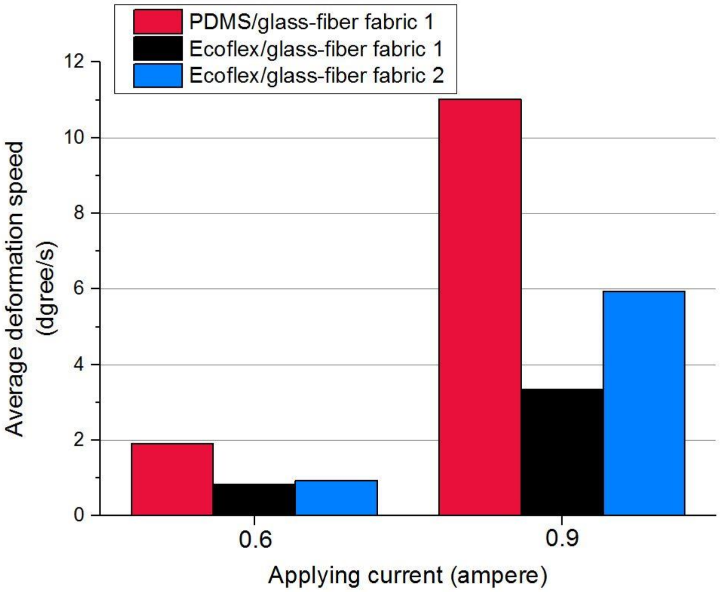

(c) Average deformation speed for reaching the maximum deformation as a function of applying current

(d) Detailed specifications of each actuators

No.	Specification
#1	PDMS matrix, Woven layer (Glass fiber/SMA wires), 1 layer of Glass fiber fabric
#2	Ecoflex matrix, Woven layer (Glass fiber/SMA wires), 1 layer of Glass fiber fabric
#3	Ecoflex matrix, Woven layer (Glass fiber/SMA wires), 2 layer of Glass fiber fabric

Figure 2-20. End-edge deflection variation with the matrix material, the number of the glass-fiber fabric layers, and the magnitudes of applying current

Chapter 3.

Applications of woven actuators*

3.1. Rear-spoiler for ground vehicles

3.1.1. Introduction

The driving performance of ground vehicles is influenced by various factors that can be characterized as external or internal to the body. To improve efficiency, the fundamental elements of the internal structure of a car have been researched extensively, including the internal combustion engine, the steering apparatus, and the power train. However, for a long time, the aerodynamic properties of cars were not recognized as a significant factor in car performance. Since the 1960s, car aerodynamics, which was affected as the car exterior evolved, became a crucial and low-cost technology that could lead to better vehicle performance as other features reached a mature stage [33, 34]. In driving, friction-like forces, including the downforce generated by the

---

*Chapter 2 and 3 were published as regular articles:

[1] Han, M.-W., et al., 2016, "Woven type Smart Soft Composite for Soft Morphing Car Spoiler," Compos. Part B-Eng., Vol. 86, pp. 285-298.

[2] Han, M.-W., et al., 2016, "Shape Memory Alloy/Glass Fiber Woven Composite for Soft Morphing Winglets of Unmanned Aerial Vehicles," Compos. Struct., Vol. 140, pp. 202-212.

[3] Han, M.-W., et al., 2014, "Design and Performance Evaluation of Soft Morphing Car-spoiler," ASME IDETC/CIE 2014.

[4] Han, M.-W., 2013, "Fabrication of Morphing Structure using Woven type Smart Soft Composite," Master thesis, Seoul National University.

moving vehicle, have a considerable effect on the performance of the vehicle in terms of braking, cornering, and acceleration. These forces are related to the vertical load and friction coefficients of each tire. By modifying the external shape of the vehicle, the adhesion forces on the tires related to the normal force of the vehicle with the ground can be controlled to improve running ability in cornering and braking. Especially, wings mounted on vehicles have been used primarily to apply aerodynamic forces to increase the downforce exerted on the tires without increasing the vehicle's weight with minimal drag [33-35].

A spoiler is an aerodynamic device that is used to generate aerodynamic forces using the airflow over the vehicle. Specifically, a rear spoiler diffuses airflow, minimizing vortexes at the rear of the vehicle while inducing downward pressure. To improve the aerodynamic efficiency of vehicles using spoilers, various types of spoilers have been investigated. With respect to the shape of the spoiler, fundamental research has been performed on shapes ranging from flat panels to inverted airfoils [36]. Studies of single-element wings including NACA airfoil were performed using computational fluid dynamics (CFD) analyses and wind tunnel experiments considering diverse ground effects (i.e., moving ground and fixed ground) [37-42]. Furthermore, multi-element wings with deflecting parts such as flaps to reinforce air-induced forces were investigated [43-47].

Recently, various types of morphing wings for aerial vehicles have been investigated to improve efficiency over a wider range of flight environments by changing its shape to adapt to the vehicle's running condition [1, 48]. To realize the morphing mechanism, smart materials such as shape memory materials and piezoelectric materials or adaptive structures were used to change the shape of the system [49-51]. Shape memory materials are characterized by the ability to recover their shape after deformation under specific conditions [22]. Among the shape memory materials, shape memory alloy (SMA) materials are widely used in the design of shape memory structures due to their superelasticity, their high power to weight ratio, and also due to their shape memory effect [52]. In the aerospace field, many of SMA applications are intended to amplify aerodynamic performance using deformable wings while reducing the complexity of the actuating system [53]. Analysis on the capability of adaptive wings consisting of sandwich structures, flexible ribs, and a flexible skin was simulated to determine whether SMA devices can generate enough force to realize the deformation of the wings [54].

A morphing wing was controlled using shape memory alloy actuators to improve the aerodynamic efficiency of the wing in terms of the lift-to-drag ratio (C_L/C_D) and laminar flow extension over the upper surface of the wing with a hardware-in-the-loop control strategy [55]. SMA actuators were used to create a discretized curvature approximation in the hyperelliptical cambered span wing inspired by the bird morphology [56]. To store the elastic energy and to obtain a larger deformation than by using SMA wires, SMA springs were used for a changeable skin of the wing [57]. To be used for a twist morphing wing, a soft morphing actuator capable of twisting motion using a pair of SMA wires was investigated [8]. Also, smart soft composite (SSC) actuators in which smart materials and anisotropic materials are embedded together in an elastomers was presented to with a coupled in-plane/bending/twisting deformation of the structure [17]. The SSC is categorized by its composition of anisotropic materials that exert an influence on actuation as a scaffold type and a woven type. The performance characteristic of each types of the SSC was evaluated and multiple applications have been presented [16, 21, 58, 59].

This study looks at the design and fabrication of a soft morphing structure to be used as a small-scale car spoiler following previously researched morphing wing concepts in order to improve the aerodynamic efficiency using a compact system [1, 48-51]. Since car spoilers are similar to airplane wings in form and function, morphing wing concepts could also be applied to spoilers in order to improve the driving performance further than with current mechanical spoiler systems. In the study, a new type of soft morphing spoiler was developed and evaluated to determine its aerodynamic performance in terms of the negative C_L/C_D and yawing moment. For the morphing part, a woven type SSC consisting of SMA wires and glass fibers woven together within a polydimethylsiloxane (PDMS) matrix was fabricated and implemented as a spoiler similar to a deflectable flap. Using the woven type SSC, the morphing spoiler achieved a large deformation at the trailing edge of the spoiler, and both a symmetric and asymmetric bending deformation of the spoiler were generated depending on which SMA wires were actuated. The aerodynamic characteristic of the spoiler was verified under various conditions of wind speeds, angles of attack, and actuation modes using an open-circuit blowing-type wind tunnel. Furthermore, wind tunnel experiments were conducted to compare the morphing spoiler with a symmetric airfoil, NACA 0010 with a flap, which has a deflecting element at the rear of the airfoil. Finally, the soft morphing spoiler was mounted on the small-scale vehicle and the effect of its actuation on the aerodynamic performance was measured through wind tunnel testing.

3.1.2. Design and actuation behaviors

As shown in Figure 3-1(a), soft morphing car-spoiler consists of two parts where one is a rigid part made of acrylonitrile butadiene styrene (ABS) using a 3D printer, which serves as a fixed leading edge, and the other is the woven type SSC structure which functions as a trailing edge capable of morphing its shape. To amplify the dynamic grip force between the vehicle and the ground, the trailing edge of the spoiler is designed to be actuated vertically upward. The dimensions of the morphing car spoiler are 300 mm in span (S_1), 93 mm in length (L_1), and 9 mm in height (H_1), according to the dimensions of the small-scale car (⅛ scale) to be mounted (Fig. 3-1(b)). The size of the SSC soft morphing structure is 300 mm (span-wise, S_1), 60 mm (stream-wise, L_2), and 1.1 mm (vertically, H_2).

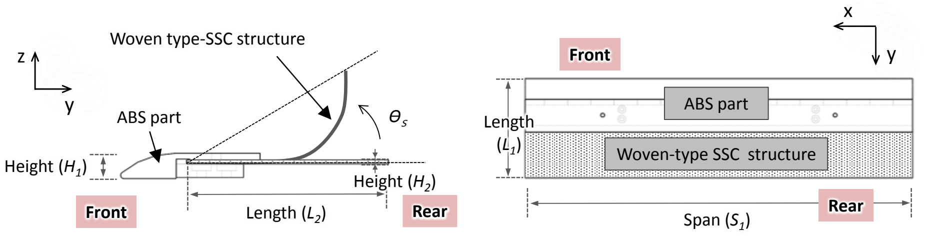

(a) Dimension of the morphing car spoiler

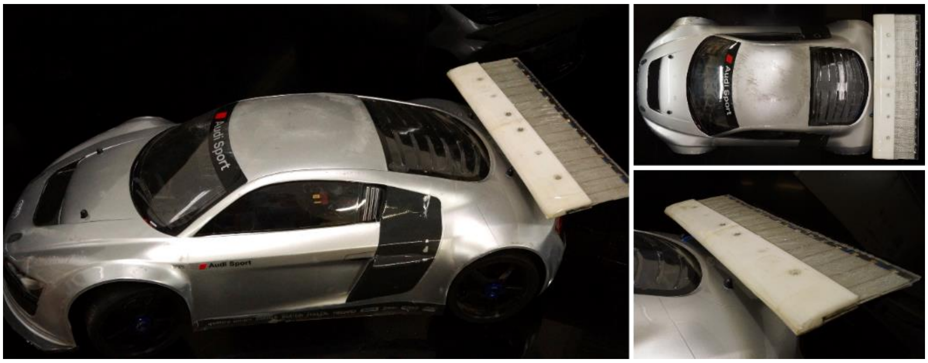

(b) Morphing spoiler with small-scale car ($\frac{1}{8}$ scale)

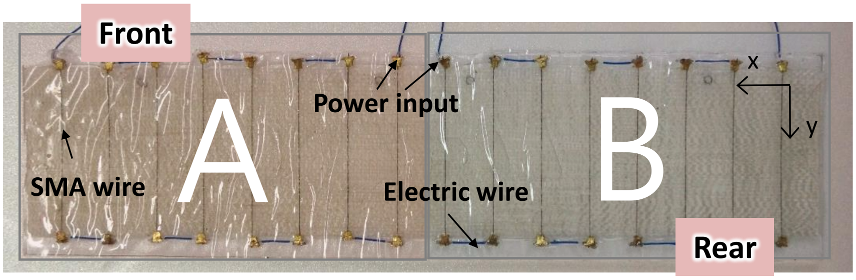

(c) Divided current channels in the woven type SSC

Figure 3-1. Diagrams of the morphing car spoiler

In total, 16 SMA wires were embedded in the spoiler at equally spaced horizontal intervals, and the SMA wires were divided into two independently controlled groups of eight SMA wires connected in series, as shown in Figure 3-1(c). These sections can be controlled independently to create asymmetrical bending of the structure through unequal power input and/or current feeding time. In this case, 200 μm SMA wires were used in preparing the spoiler. While current is applied to the SMA wires, the spoiler bends up, and then recovers its original shape without external force after the applied current is turned off. The bending speed is dependent on the heating rate of the SMA which is related to the input power, feeding time, heat dissipation, environmental temperature and others. Figure 3-2 shows that the morphing sequence of the fabricated spoiler according to the phase transformation of the SMA wires with an applied current of 1.5 A for 12 seconds at room temperature and then during cooling without an applied current.

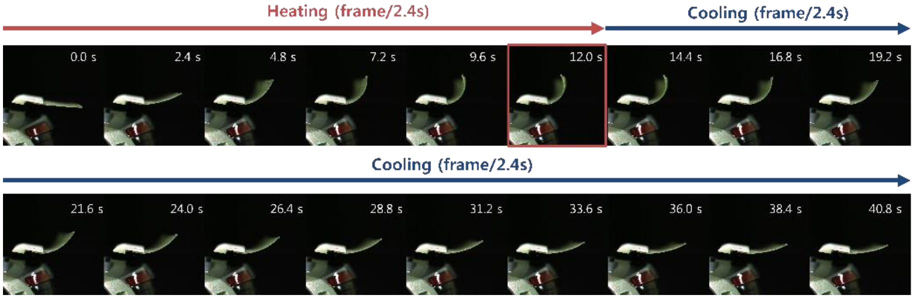

Figure 3-2. Deformation behavior of soft morphing spoiler by phase change of embedded SMA wires

To observe the aerodynamic performance of a general wing in the prepared experimental setup, a symmetrical airfoil (NACA 0010) was fabricated in accordance with the thickness ratio of the spoiler for a comparative test of the performance. Figure 3-3(a) shows the conceptual diagrams of the airfoil model; its size is 300 mm in width (S_2), 80 mm in length (L_3), and 8 mm in height (H_3). The flap of the airfoil was built modularly with two independent sections which can be moved separately. By varying the left and right flap angles, the geometry of the trailing edge of the airfoil can be changed to produce both symmetrical and asymmetrical shapes, as shown in Figure 3-3(b), and 3-3(c).

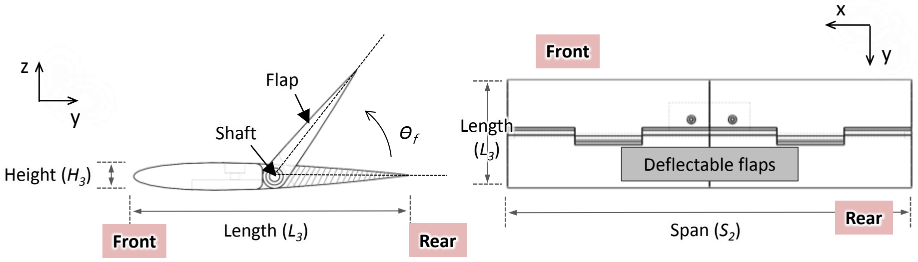

(a) Dimensions of the fabricated airfoil

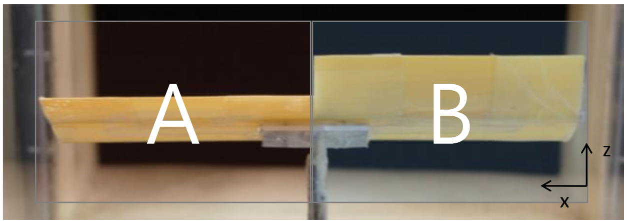

(b) Rear view of the divided flap parts of the airfoil

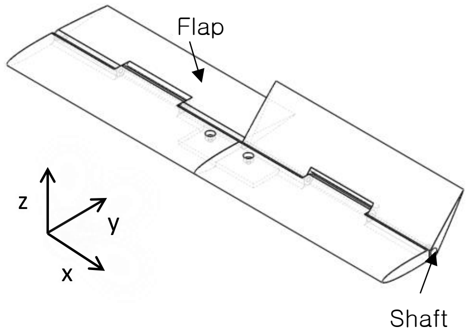

(c) Isometric view of the airfoil

Figure 3-3. Diagrams of the symmetrical airfoil

3.1.3. Modeling

To describe the generated strain within the SMA caused by the phase change, the constitutive relations with regards to infinitesimal strain tensor which given by the martensite reversible phase transformation are defined as follows [60-64]

$$\varepsilon = -\rho\frac{\partial G}{\partial \sigma} = S(\xi)\sigma + \alpha(T - T_0) + \varepsilon^t \qquad (1)$$

where G is the Gibbs free energy, σ is the stress, ξ is the total martensite volume fraction, $S(\xi)$ is the fourth-order effective compliance tensor, α is the second-order effective thermal expansion tensor, T is the absolute temperature, and ε^t is the recoverable inelastic transformation. Using the rule of mixtures, $S(\xi)$ is obtained as

$$S(\xi) = S^A + \xi(S^M - S^A) = S^A + \xi\Delta S \qquad (2)$$

where the superscripts A and M are the austenitic and martensitic phases. By assuming that the phase transformation to martensite occurs as a result of changing the martensite volume fraction without martensitic variant reorientation [61], the evolution of the transformation strain over time as a rate of the martensitic volume fraction during the forward and reverse transformations is given as

$$\dot{\varepsilon}^t = \Lambda\dot{\xi} \qquad (3)$$

$$\Lambda = \frac{3}{2}H\frac{\sigma'}{\bar{\sigma}}\ ;\ \left(\dot{\xi} > 0\right),\ \Lambda = \frac{\varepsilon^{t-r}}{\xi^r}\ ;\ \left(\dot{\xi} < 0\right) \qquad (4)$$

where Λ is the transformation direction tensor, H is a material parameter for transformation strain, σ' is the deviatoric stress tensor, $\bar{\sigma}$ is the effective stress, ε^{t-r} is the transformation strain at the reversal point, and ξ^r is the martensitic volume fraction at the reversal point.

For defining the martensitic volume fraction during phase change, the transformation function (Φ^t) is adopted which represents the transformation surface $0 \leq \xi \leq 1$ with $\xi = 0$ and $\xi = 1$ representing the fully austenite and martensite states, respectively. Following the Kuhn-Tucker conditions, the transformation functions which ensure positive dissipation during the forward and reverse transformations are given as follows [60, 62-64]

$$\Phi_{fwd}^{t}; \quad 0 \leq \xi < 1; \quad \dot{\xi} \geq 0 \qquad (5)$$

$$\Phi_{rev}^{t}; \quad 0 < \xi \leq 1; \quad \dot{\xi} \leq 0 \qquad (6)$$

$$\Phi_{fwd}^{t} = (1-D)H\bar{\sigma} + \tfrac{1}{2}\sigma : \Delta S\sigma + \rho\Delta s_0 T - \rho\Delta u_0 - \left[\tfrac{1}{2}a_1(1+\xi^{n1} + (1-\xi)^{n2}) + a_3\right] - Y^t \qquad (7)$$

$$\Phi_{rev}^{t} = -(1+D)\frac{\sigma : \varepsilon^{t-r}}{\xi^{r}} - \tfrac{1}{2}\sigma : \Delta S\sigma - \rho\Delta s_0 T + \rho\Delta u_0 + \left[\tfrac{1}{2}a_2(1+\xi^{n3} + (1-\xi)^{n4}) - a_3\right] - Y^t \ (8)$$

The deflecting motion of the woven type SSC can be described with a nonlinear transfer matrix method for the elastic curved beams, which is capable of analyzing large spatial deformations [29, 65]. In this method, the beam is divided into segments with each having own coordinates capable of translation and rotation along with their axes following the direction of the deformation. Figure 3-4 shows the geometric parameters which is used for describing the structural behavior of the deformation of the beam.

Each segments defined by two nodal points i and $i+1$, and the position vector of each point along the beam axis is r. The local cartesian coordinates for each segment are defined as $x_{(i)}$, $y_{(i)}$, and $z_{(i)}$, and at the origin and end of the segment are $x_{(i)} = 0$, $x_{(i)} = L_{(i)}$ respectively.

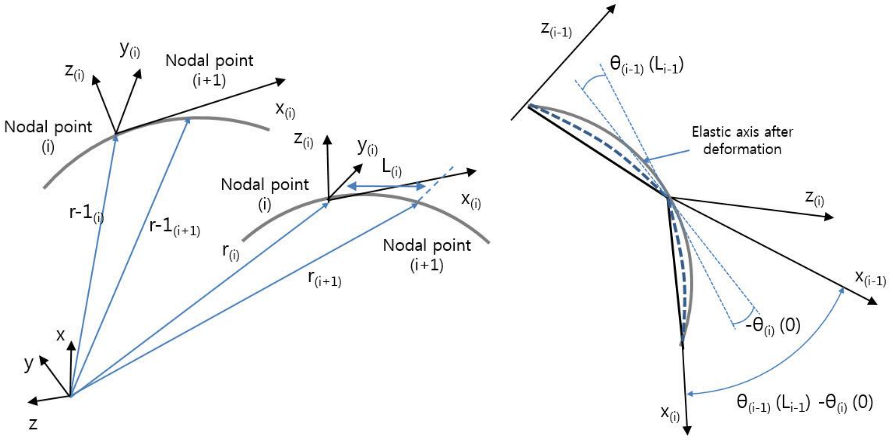

Figure 3-4. Geometric parameters of elastic beam deformation

Under the assumption that materials in the confined segment have an infinitesimal strain defined as $(L_{(i)}+\delta_{(i)}L_{(i)})=L_{(i)}$, where $\delta_{(i)}$ is the local displacement vector of each point along the elastic axis of the i_{th} segment, and elastic torsional rotation is $\varphi_{(i)}(0)=0$, then the lateral displacement and elastic torsional rotation are defined as

$$v,w_{(i)}\left(x_{(i)}\right)=\frac{\mathrm{d}v,w_{(i)}}{\mathrm{d}x_{(i)}}(0)\cdot x_{(i)}+\frac{1}{L_{(i)}}\cdot\left[-2\frac{\mathrm{d}v,w_{(i)}}{\mathrm{d}x_{(i)}}(0)-\frac{\mathrm{d}v,w_{(i)}}{\mathrm{d}x_{(i)}}\left(L_{(i)}\right)\right]\cdot x_{(i)}^{2}+\frac{1}{L_{(i)}^{2}}\cdot\left[\frac{\mathrm{d}v,w_{(i)}}{\mathrm{d}x_{(i)}}(0)-\frac{\mathrm{d}v,w_{(i)}}{\mathrm{d}x_{(i)}}\left(L_{(i)}\right)\right]\cdot x_{(i)}^{3} \qquad (9)$$

$$\varphi_{(i)}\left(x_{(i)}\right)=\frac{\mathrm{d}\varphi_{(i)}}{\mathrm{d}x_{(i)}}(0)\cdot x_{(i)}+\frac{1}{2\cdot L_{(i)}}\cdot\left[\frac{\mathrm{d}\varphi_{(i)}}{\mathrm{d}x_{(i)}}\left(L_{(i)}\right)-\frac{\mathrm{d}\varphi_{(i)}}{\mathrm{d}x_{(i)}}(0)\right]\cdot x_{(i)}^{2} \qquad (10)$$

The rotation matrix considering the elastic rotation angles $\theta_{(i-1)}(x_{(i-1)})$ and $\theta_{(i)}(x_{(i)})$ are defined as

$$E_{(i)}x_{(i)} = \begin{bmatrix} \cos\left(\theta_{(i)}x_{(i)}\right) & 0 & -\sin\left(\theta_{(i)}x_{(i)}\right) \\ 0 & 1 & 0 \\ \sin\left(\theta_{(i)}x_{(i)}\right) & 0 & \cos\left(\theta_{(i)}x_{(i)}\right) \end{bmatrix} \qquad (11)$$

By including the equilibrium force and the moment for each segment, the state loading vector is defined as follows

$$x_{(i)}\left(L_{(i)}\right) = A_{(i)} \cdot x_{(i)}(0) \qquad (12)$$

$$A_{(i)} = \begin{bmatrix} 1 & 0 & 0 & 0 & 0 & 0 & -F^e_{x(i)} \\ 0 & 1 & 0 & 0 & 0 & 0 & -F^e_{y(i)} \\ 0 & 0 & 1 & 0 & 0 & 0 & -F^e_{z(i)} \\ 0 & 0 & 0 & 1 & 0 & 0 & -Q^e_{x(i)} \\ 0 & 0 & L_{(i)} & 0 & 1 & 0 & -F^e_{z(i)} \cdot \frac{L_{(i)}}{2} \cdot -Q^e_{y(i)} \\ 0 & -L_{(i)} & 0 & 0 & 0 & 1 & F^e_{y(i)} \cdot \frac{L_{(i)}}{2} \cdot -Q^e_{z(i)} \\ 0 & 0 & 0 & 0 & 0 & 0 & 1 \end{bmatrix} \qquad (13)$$

Utilizing the above equations (9-13) with the Euler beam theory, the relations to calculate the deformation of the segments as a function of the resultant forces and moments including the bending stiffness of the actuator are obtained as follows

$$\frac{\mathrm{d}v,w_{(i)}}{\mathrm{d}x_{(i)}}(0) = -\frac{L_{(i)}}{3}\cdot\frac{\mathrm{d}^2v,w_{(i)}}{\mathrm{d}x_{(i)}^2}(0) - \frac{L_{(i)}}{6}\cdot\frac{\mathrm{d}^2v,w_{(i)}}{\mathrm{d}x_{(i)}^2}\left(L_{(i)}\right) \qquad (14)$$

$$\frac{\mathrm{d}v,w_{(i)}}{\mathrm{d}x_{(i)}}\left(L_{(i)}\right) = \frac{L_{(i)}}{6}\cdot\frac{\mathrm{d}^2v,w_{(i)}}{\mathrm{d}x_{(i)}^2}(0) + \frac{L_{(i)}}{3}\cdot\frac{\mathrm{d}^2v,w_{(i)}}{\mathrm{d}x_{(i)}^2}\left(L_{(i)}\right) \qquad (15)$$

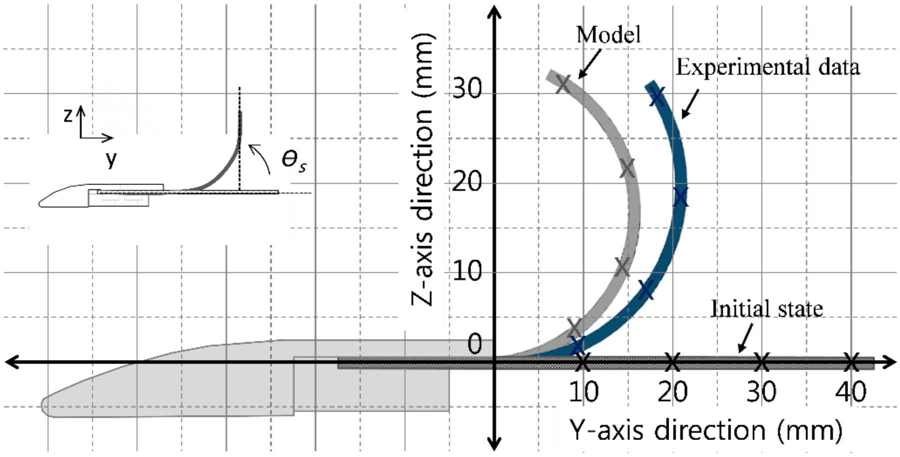

Figure 3-5. Deformation profiles of the morphing spoiler with respect to the analytical modeling and experimental result

Table 3. Specification of the woven actuator

Parameter	Value (Unit)
Number of the layers for glass-fiber fabric	1 layer
Matrix	PDMS
Young’s modulus	109.2 MPa
Density	1.05 Mg/m^3

For characterizing the material properties of the morphing spoiler, a beam-shaped specimen was prepared and tested with the Universal Testing Systems (Instron 5948 Microtester). The specification of the specimen is shown in Table 3. The analytical modeling shown previously for calculating the elastic beam deformation of the morphing spoiler was used with these material properties to predict the deformation shape of the spoiler. The results of the modeling and the experiment with respect to the maximum end-edge deflection are shown in Figure 3-5 which shows the deformation profiles in the Y-Z plane. The predicted maximum end-edge deflection of the model was 149.9° with a maximum error of 16 % and the maximum end-edge deflection of the fabricated morphing spoiler was 127° with an error of 18 %.

3.1.4. Wind tunnel testing with soft morphing spoiler

The aerodynamic properties of the spoiler and of the airfoil were tested in an open-circuit blowing-type wind tunnel. The forces acting on the spoiler and the airfoil were measured through a dynamometer (Kistler, type 9256C1, measuring range: -250 to 250 N) connected through an amplifier (Kistler, type 5070A11100) to a controller board (dSPACE, DS1103 PPC) for measuring three-axis forces and moments. Figure 3-6 shows the experimental setup of the wind tunnel tests. The model was placed at the center of the 3 × 0.6 × 0.6-m test section and the forces were measured through a streamlined aluminum strut attached at the center of gravity of the model. The blowing wind velocity was controlled at a constant value, varying from 5 m/s to 20 m/s in increments in 5 m/s. In the case of the morphing spoiler, a power supply was placed outside of the wind tunnel and connected to the SMA wires through the supporting strut. The x, y, and z axes correspond to the span-wise, stream-wise, and vertical directions, respectively.

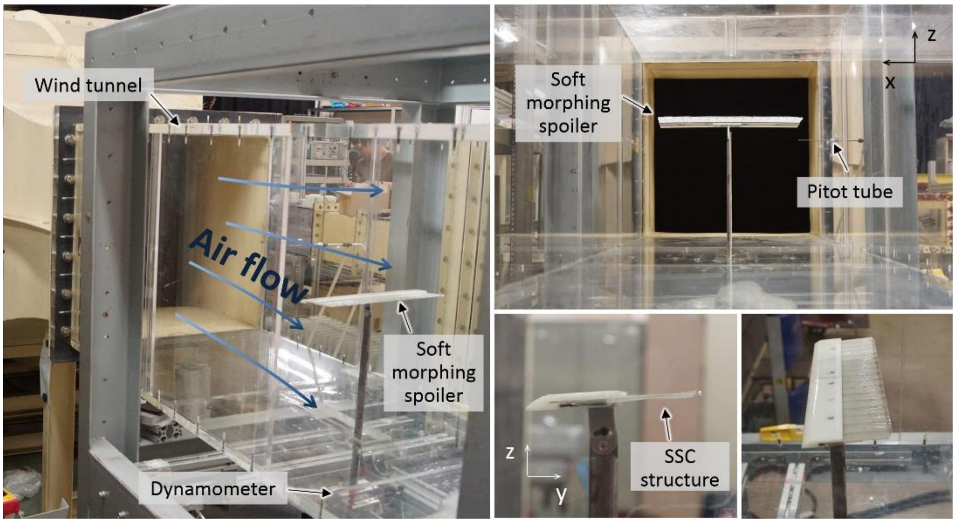

Figure 3-6. Experimental set-up of the wind tunnel test

The spoiler and the airfoil were tested in the wind tunnel at varying angles of attack, from -30° to 10° in increments of 10°. In the case of the airfoil, the flap angle is introduced as an additional variable parameter which gives increased levels of downforce compared with the non-deflecting airfoil. The flap angle was changed from 0° to 45° in increments of 15°, as shown in Figure 3-7. Figure 3-7 also shows the criterion for angle measurement of both testing models. The angle of attack (θ_{at}) and the deflected angle of the end-edge of the spoiler (θ_s) were measured from the horizontal surface of the test section to the edge of the front or rear model part. Also, the flap angle (θ_f) was measured from the angle of attack of the airfoil.

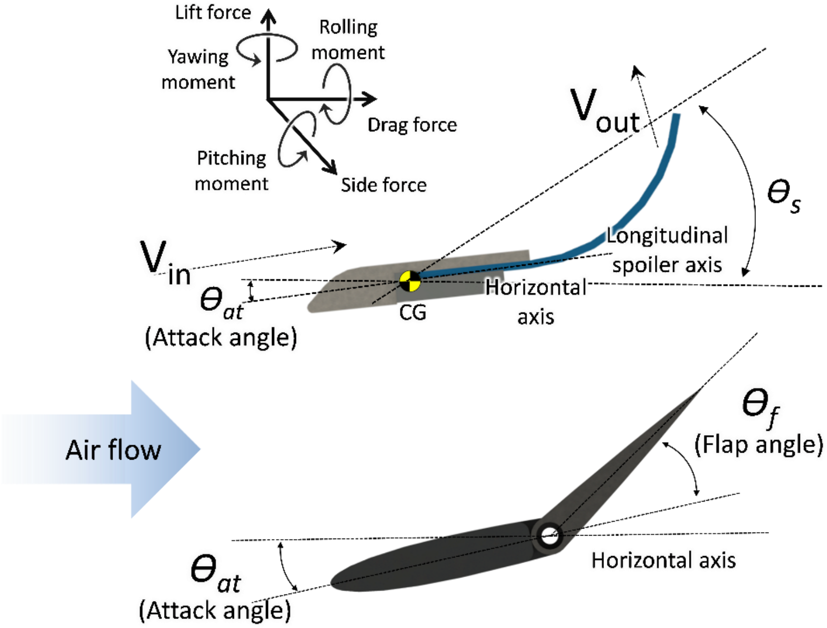

Figure 3-7. Induced forces on the morphing spoiler and airfoil

The soft morphing spoiler is a compliant structure whose deformation degree is altered depending on the induced external forces. As seen in Figure 3-8, when the wind did not blow in the wind tunnel section, the maximum deflection angle (θ_{s0}) was three times greater than the fully actuated spoiler at a wind speed of 20 m/s. Although the deformation was reduced with increasing wind speeds, the measured force with the deformed spoiler increased with increasing wind speeds. In Table 4, the maximum deformed angle of the edge is denoted with morphometric parameters under various conditions of wind speed and angle of attack.

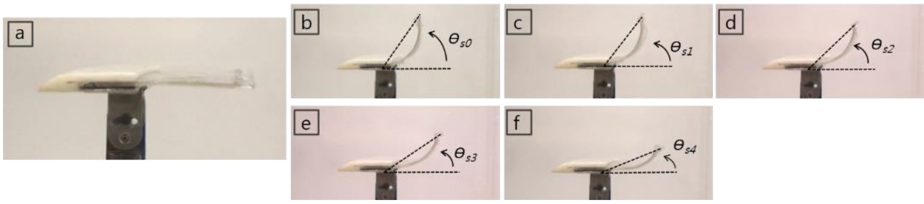

Figure 3-8. Bend-back by external aerial forces at an attack angle of 0°; (a) before actuation, (b) actuation with no air flow, (c) the wind speed of 5 m/s, (d) 10 m/s, (e) 15 m/s, and (f) 20 m/s

Table 4. Morphometric parameters of the morphing spoiler

Wind speed [m/s]			0	5	10	15	20
Max. deformed angle of the end edge [deg.]	AOA [deg.]	**-20**	46	42	39	32	25
		-10	38	33	30	21	19
		0	34	30	26	21	15
		10	27	25	21	16	9
Planform area, A [m^2]		**-20**	1.9e-2	1.9e-2	2.1e-2	2.5e-2	2.7e-2
		-10	2.1e-2	2.1e-2	2.2e-2	2.6e-2	2.7e-2
		0	2.0e-2	2.1e-2	2.1e-2	2.5e-2	2.7e-2
		10	2.5e-2	2.4e-2	2.5e-2	2.6e-2	2.7e-2
Reynolds $\text{Number}_{\text{chord}}$		**-20**	-	3.0e4	6.1e4	9.5e4	1.3e5
		-10	-	2.8e4	5.9e4	9.4e4	1.3e5
		0	-	2.8e4	5.7e4	9.2e4	1.3e5
		10	-	2.7e5	5.8e4	9.1e4	1.2e5
Aspect ratio, AR (=Span^2/A)		**-20**	4.7	4.7	4.3	3.6	3.3
		-10	4.3	4.3	4.1	3.5	3.3
		0	4.5	4.3	4.3	3.6	3.3
		10	3.6	3.8	3.6	3.5	3.3
Chord length, L [m]		**-20**	9.1e-2	9.1e-2	9.1e-2	9.5e-2	9.8e-2
		-10	8.7e-2	8.4e-2	8.8e-2	9.3e-2	9.5e-2
		0	8.2e-2	8.4e-2	8.6e-2	9.2e-2	9.5e-2
		10	8.2e-2	8.2e-2	8.6e-2	9.1e-2	9.2e-2

* Thickness ratio: 1:10; wing span: 0.3 m

* Air density (ρ): 1.22 [kg/m^3]; air viscosity (μ): 1.8×10^{-5} [$N \cdot s/m^2$]

* Reynolds $\text{Number}_{\text{chord}}$: $\rho u_\infty L/\mu$ (u_∞: mean velocity of airflow; L: chord length)

The lift (C_L) and drag (C_D) coefficients are defined as $C_{L,D} = Force_{L,D} / (0.5\rho u_\infty^2 A)$, where ρ is the air density, u_∞ is the wind speed, and A is the reference area. In this case, the reference area is defined as the planform area, i.e., the projected plane from the top of the model onto a horizontal surface. The results of each test were calculated by subtracting the initial force from the measured force, meaning the force measured when the strut alone was tested in the wind tunnel, without a spoiler.

Since the spoiler’s deformation depends both on its actuation state and on the external force applied by the wind, the dimensionless coefficients are changed due to the reference area used to calculate them is also modified by the induced wind speed. The lift coefficients for various angles of attack of the morphing spoiler and airfoil are shown in Figure 3-9. For the morphing spoiler, the maximum negative lift was measured when the angle of attack was 0°. In the case of the airfoil, at a flap angle of 0°, the negative lift coefficient was higher for a decreased angle of attack. Results for the drag coefficient are shown in Figure 3-10. As the angle of attack increased, the drag coefficient of the airfoil decreased, and the morphing spoiler’s drag coefficient was maximal at an angle of attack of 0°.

In Figure 3-11, the C_L/C_D for the spoiler and airfoil are shown with various angles of attack and wind speeds. The minimum value of the C_L/C_D for the morphing spoiler was observed at an attack angle of 0° with a wind speed of 20 m/s. As the negative lift coefficient decreased with higher wind speeds, the drag coefficient also decreased; thus, the negative C_L/C_D was maximized in faster airflows. For the airfoil, the C_L/C_D value ranged from 1.3 to 2.5 for angles of attack below -10°, which is lower than those of the spoiler. However, for angles of attack above -10°, the C_L/C_D increased sharply and reaches positive values for angles of attack of 10° while the spoiler maintained a negative C_L/C_D. The results also showed that the wind speed did not have a significant effect on the performance of the rigid airfoil. However, the coefficients of the morphing spoiler varied with the wind speed since its reference area was affected by the force of the wind flow. As the value of the angle of attack increased, the morphing spoiler requires more force to actuate upward because of the increase in the initial contact surface of the induced air.

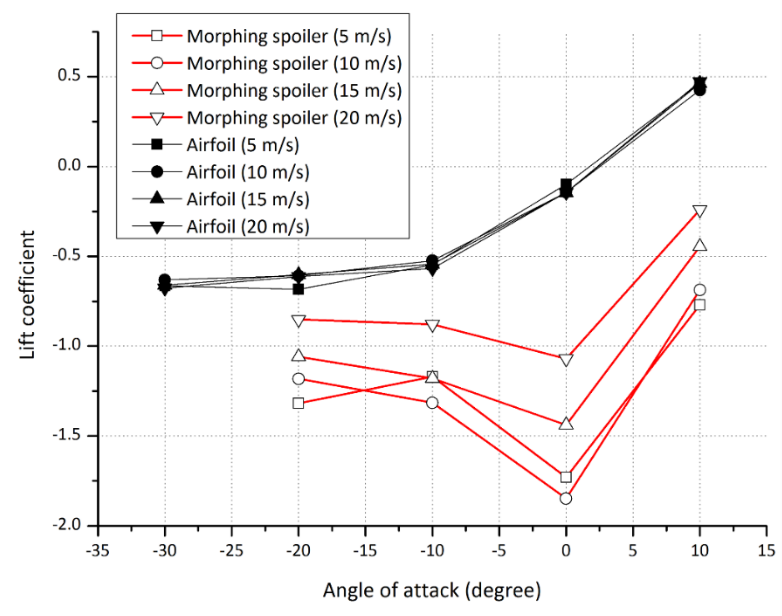

Figure 3-9. Lift coefficient with various wind speeds of the morphing spoiler (red lines) and airfoil at a flap angle of 0° (black lines)

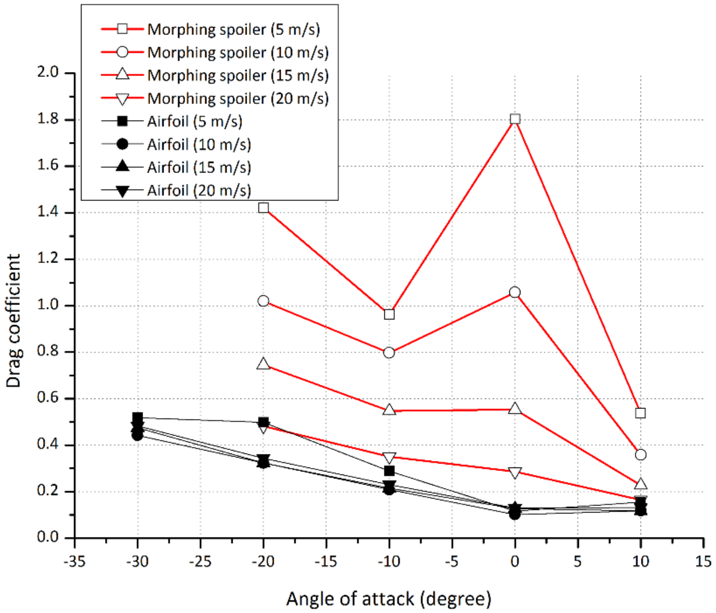

Figure 3-10. Drag coefficient with various wind speeds of the morphing spoiler (red lines) and airfoil at a flap angle of 0° (black lines)

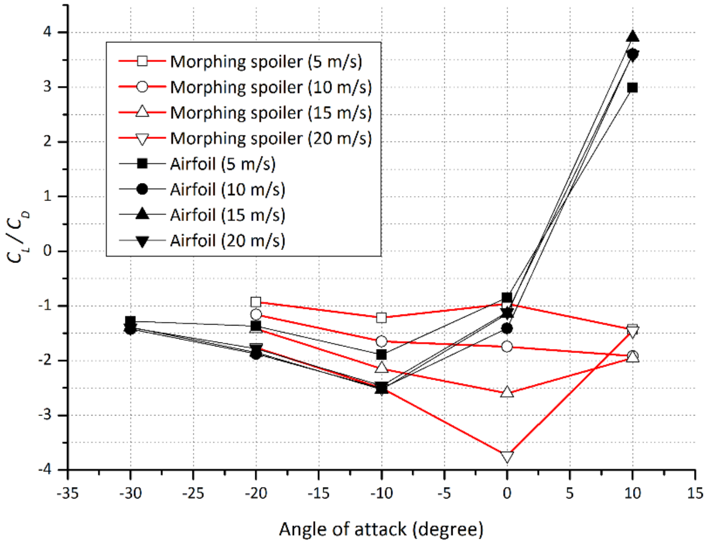

Figure 3-11. C_L/C_D with various wind speeds of the morphing spoiler (red lines) and airfoil at a flap angle of 0° (black lines)

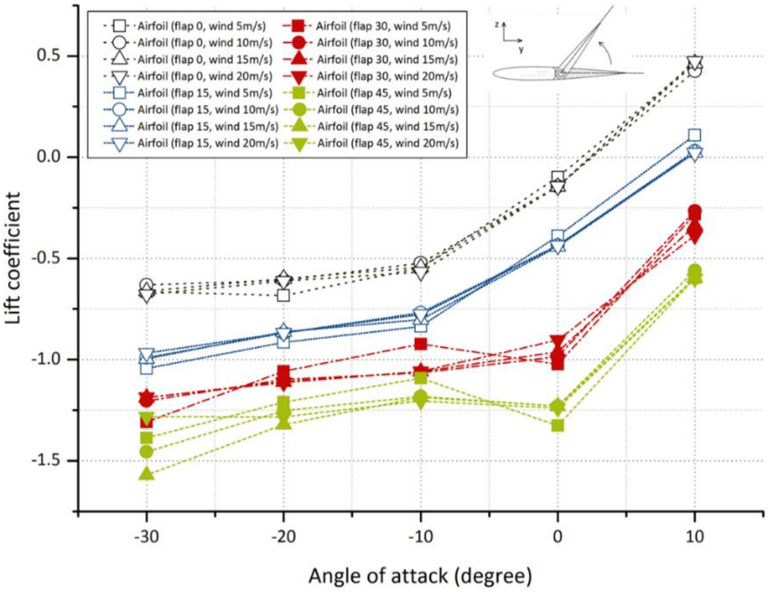

(a) Lift coefficient of the airfoil with various wind speeds and flap angles

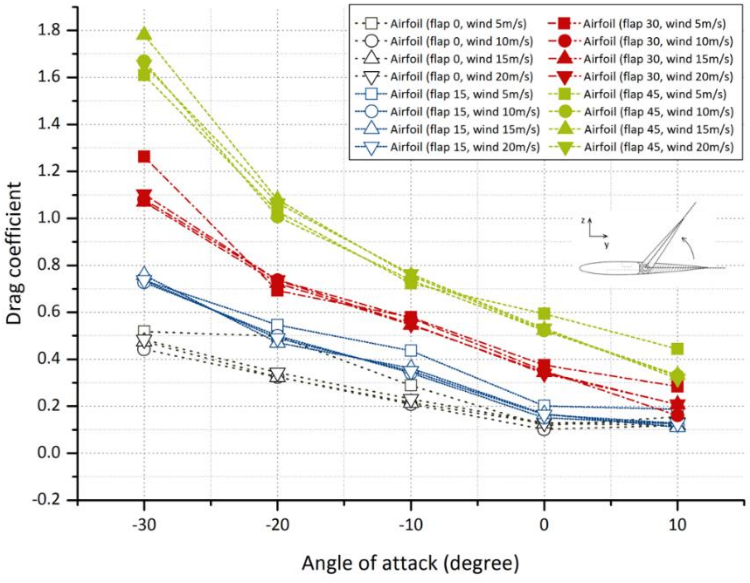

(b) Drag coefficient of the airfoil with various wind speeds and flap angles

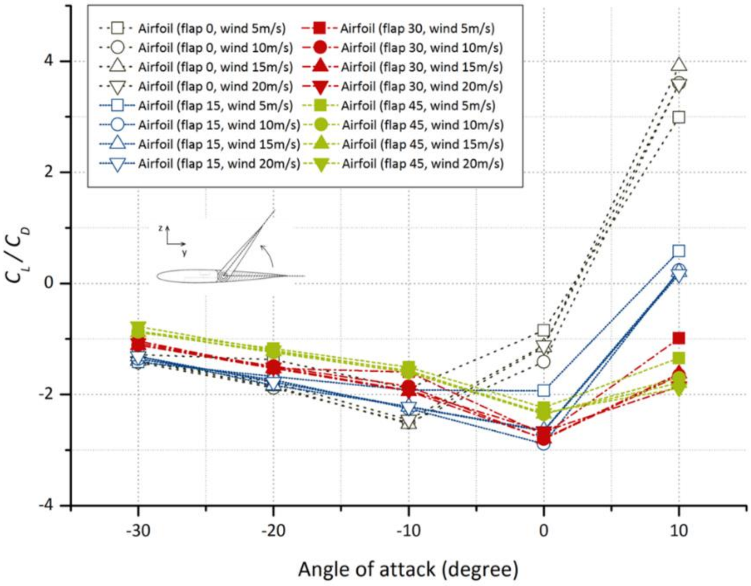

(c) C_L/C_D of the airfoil with various wind speeds and flap angles

Figure 3-12. Results of the wind tunnel test using the airfoil

Figure 3-12 shows the results of wind tunnel tests using the airfoil at various wind speeds and angles of attack. As the flap angle is increased, the value of C_L is lower, as shown in Figure 3-12(a). Each sets of values depend on the flap angle, and they are not affected by the wind speed. Figure 3-12(b) indicates that as the flap angle is increased, the drag coefficient also increases. The values for C_L/C_D are shown in Figure 3-12(c). The minimum value was -2.9 for an angle of attack 0° with a flap angle of 15°. In the case of a symmetric deformation, both the morphing spoiler and the airfoil performed best at an angle of attack of 0°. From all of the results of wind tunnel tests, it is clear that the force is greatly affected by the initial setup of the airfoil in terms of the angle of the leading edge and the flap angle. By changing the orientation of the airfoil, including the angle of attack and the flap angle, the aerodynamic forces of the airfoil can also be changed.

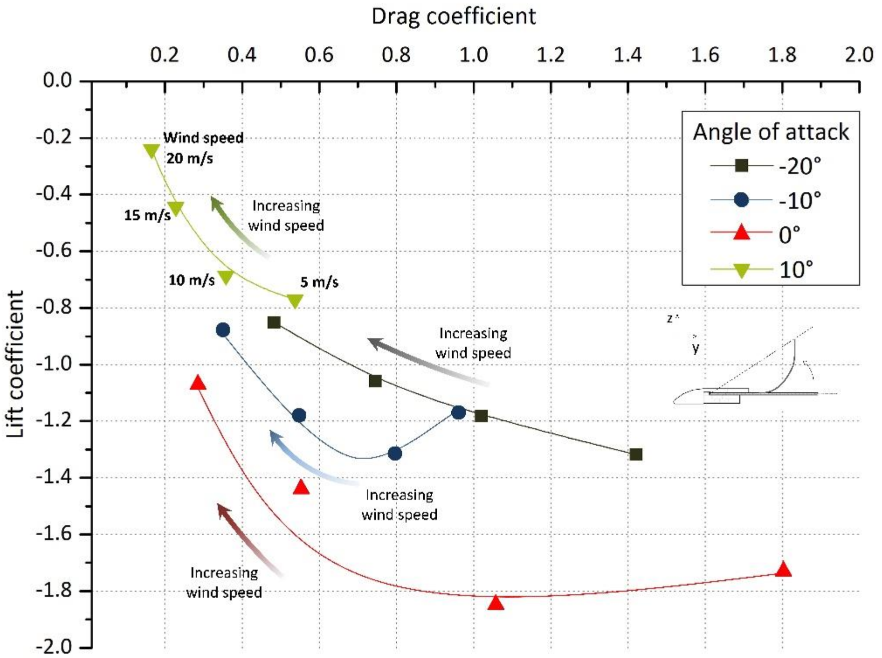

Figure 3-13. Variations of the lift-drag coefficient of morphing spoiler in various wind speeds (from 5 m/s to 20 m/s in increments in 5 m/s) and angles of attack; Each point is connected with same angle of attack: -20° (black), -10° (blue), 0° (red), 10° (green)

Figure 3-13 shows the C_L-C_D curve of the morphing spoiler. Unlike the aerodynamic characteristics of the airfoil based on solid materials, the C_L-C_D value of the morphing spoiler is changed depending on the wind speed as well as angle of attack since it consists of compliant parts. In Figure 3-13, each point is connected with the same wind speed to show the range of aerodynamic performance depending on the wind speed.

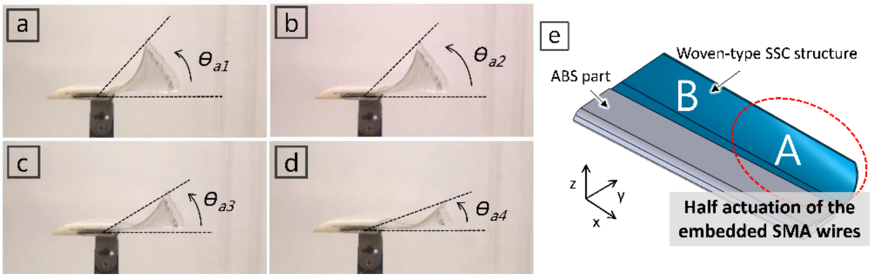

Figure 3-14. Captured images of the fully asymmetrically actuated morphing spoiler in the wind tunnel at various wind speeds; (a) the wind is blowing at a speed of 5 m/s, (b) 10 m/s, (c) 15 m/s, and (d) 20 m/s, (e) concept of the asymmetric motion of the morphing spoiler

To enhance the turning ability of the car, the spoiler was designed to be able to separately actuate both halves of the morphing spoiler as shown in Figure 3-1(c). Its aerodynamic characteristics were tested in the wind tunnel in the same conditions as in the previous experiments. Figure 3-14 shows the motion of the morphing spoiler when only a half-section of the spoiler was actuated. The measured forces are shown in Figures 3-15 and 3-16, and the z-axis moment (yawing moment) is shown in Figure 3-17. In these graphs, the flap angle of the airfoil was set as 30°. The downforces generated by the morphing spoiler were greater than those by the airfoil during asymmetric motion except for a wind speed of 20 m/s. Also, the drag forces generated by the morphing spoiler were smaller than those of the airfoil when the angle of attack was 0° and the wind speed was 20 m/s. The results of the measurement of the moments showed that morphing spoiler generates larger yawing moment than those of the airfoil, except for a wind speed of 20 m/s. The maximum moment was 0.02 Nm at an angle of attack of 10° for the morphing spoiler which is approximately 1.7 times higher than the airfoil.

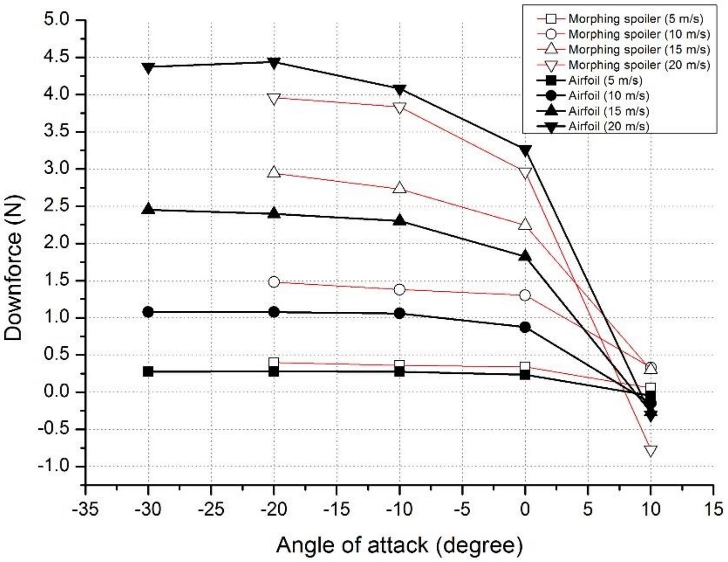

Figure 3-15. Downforce of the morphing spoiler (red lines) and airfoil at a flap angle of 30° (black lines) in asymmetric modes

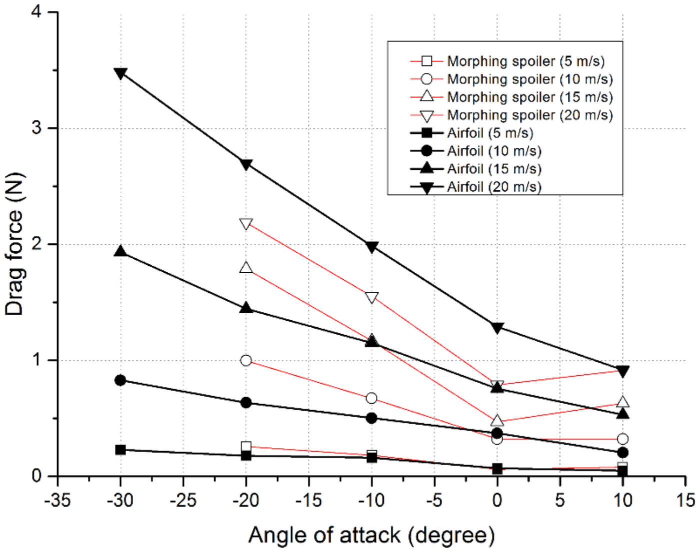

Figure 3-16. Drag force of the morphing spoiler (red lines) and airfoil at a flap angle of 30° (black lines) in asymmetric modes

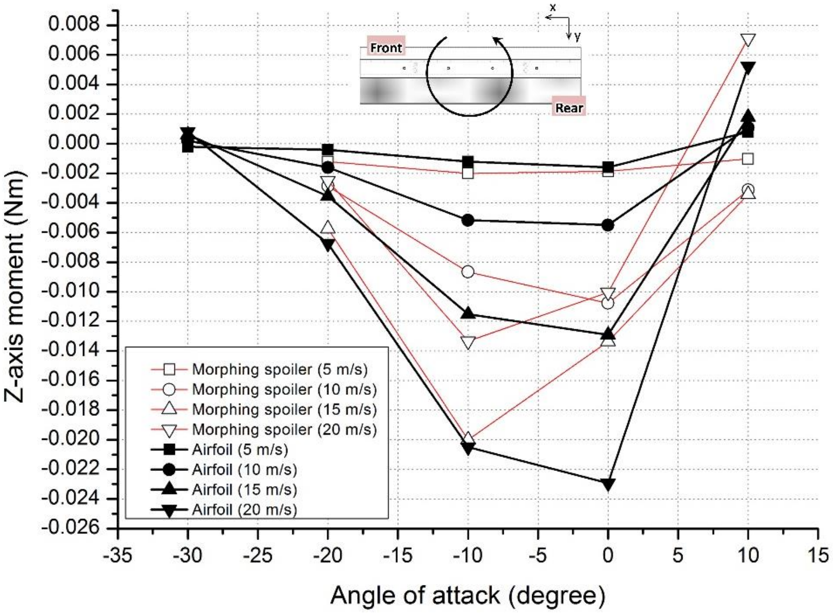

Figure 3-17. *Z*-axis moment of the morphing spoiler (red lines) and airfoil at a flap angle of 30° (black lines) in asymmetric modes

3.1.5. Small-scale vehicle with soft morphing spoiler

To determine the influence of the interaction between the vehicle body and the spoiler, the soft morphing spoiler was mounted on a small-scale vehicle (Audi R8 lms 1/8, kyosho corp.) The overall layout of the vehicle is shown in figure 3-18. For actuation of the spoiler, remote control parts and the battery used to control and apply power to the SMA wires were added on the vehicle. Considering that the shifting of center of gravity (*CG*) from the added components, the spatial distribution of mass within the vehicle body was adjusted to distribute equally the weight of vehicle using additional weights. Through the arrangement of the *CG* location by evaluating the weight of each components, the vehicle will remain stable throughout the actuation of the spoiler and prevent any unpredictable movements of the vehicle. A dynamometer was used to evaluate the weight of each tire as shown in figure 3-19 with results showing approximately 10 N for each tire.

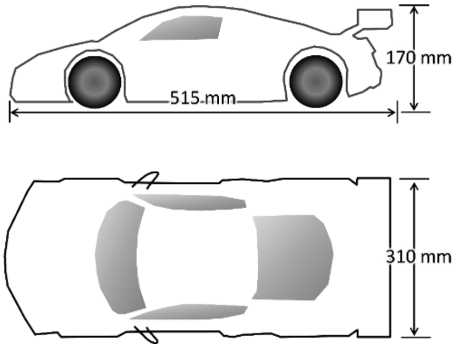

Figure 3-18. Dimension of small-scale car

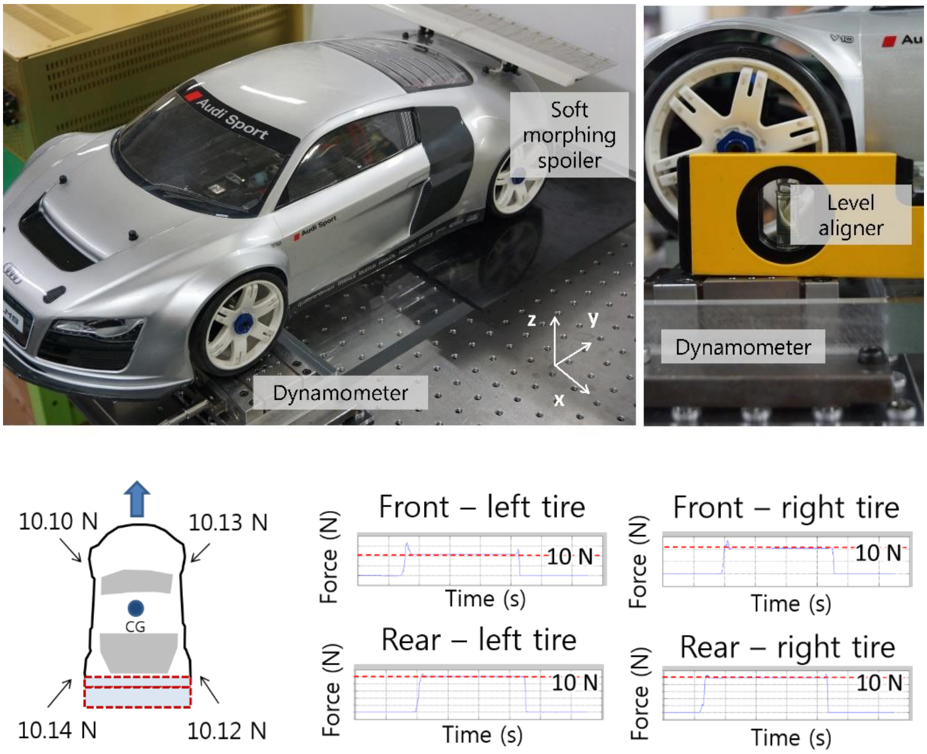

Figure 3-19. Arrangement of center-of-gravity

Table 5. Morphometric parameters of small-scale vehicle with morphing spoiler

Parameter	Value
Length [mm]	515
Width [mm]	310
Height [mm]	170
Frontal area [mm^2]	43821
* Air density (ρ): 1.22 [kg/m^3]; air viscosity (μ): 1.8 × 10^{-5} [N·s/m^2] * Mean velocity of airflow (u_∞): 15.8 [m/s]	

Wind tunnel testing using small-scale vehicle was conducted in a closed-type wind tunnel (test section of 900 × 900 mm). A streamline bar was attached on the bottom of the vehicle, and the dynamometer used for measuring the forces was fixed outside of the wind tunnel assembled on the other end of the streamline bar. To provide support for holding the vehicle’s position, thin strings were tied to the wheel of each tires. The lift and drag forces were measured with an angle of attack of the spoiler of 0° and a wind speed of 15.8 m/s in the streamline direction (Y-direction). The morphological parameters of the small-scale vehicle with the spoiler are shown in table 5. Also, the experimental set-up for wind tunnel testing and the captured images of the spoiler before and during actuation are shown in figure 3-20 and 3-21.

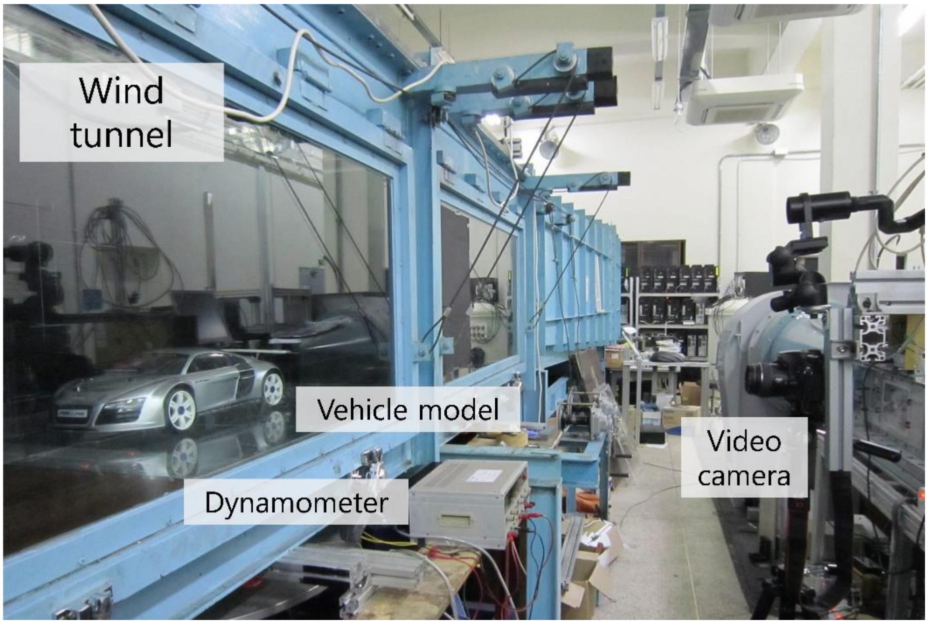

(a) Wind tunnel set-up overview

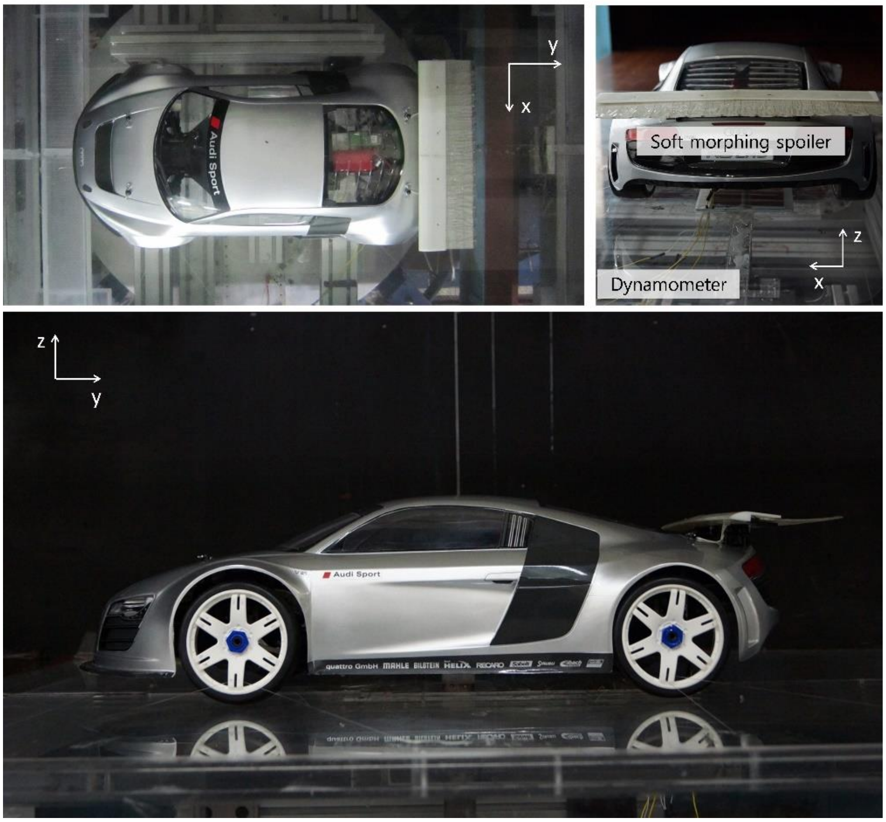

(b) Small-scale vehicle in wind tunnel

Figure 3-20. Experimental set-up for wind tunnel test

(a) Before actuation (b) Actuation of the spoiler

Figure 3-21. Small-scale vehicle with morphing spoiler at 15.8 m/s

The variations of coefficients for lift and drag forces are shown in figure 3-22, which were calculated from data obtained by wind tunnel testing. In figure 3-22(a), at the maximum wind speed of 15.8 m/s, the vehicle shows an increase of a negative lift coefficient of -198 % during spoiler actuation, but the drag coefficient is also increased by about 41 % compared with the non-actuated condition. Polar representation of the force coefficients which show the relation between two dimensionless quantities (coefficients of the lift and drag) is shown in figure 3-22(b). The space between two data points indicates a time interval of 5 sec for C_L and C_D. In drag polar, the performance characteristics of the morphing spoiler mounted on the small-scale car shows that the drag coefficient increases as the negative lift coefficient increases during actuation, but that inversely the drag coefficient decreases as the negative lift coefficient decreases during cooling of the spoiler. Thus, C_D reaches its highest point when C_L reaches its lowest value.

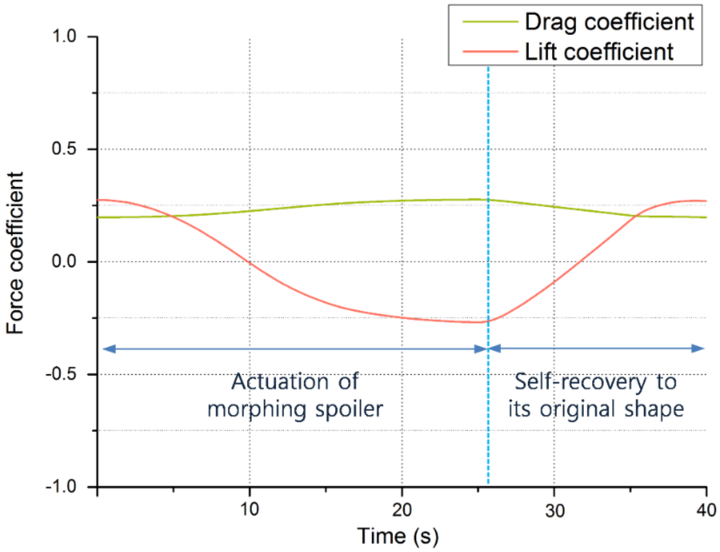

(a) Variation of force coefficients of soft morphing spoiler with the course of time

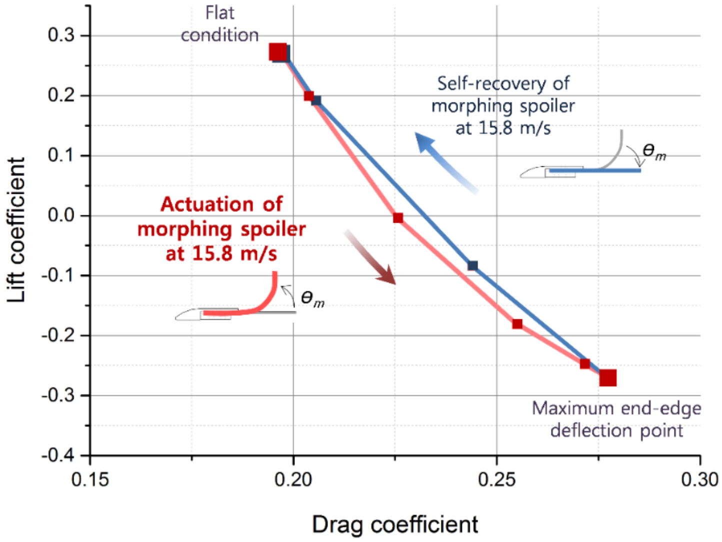

(b) C_L - C_D curve for soft morphing spoiler

Figure 3-22. Results of wind tunnel test at 15.8 m/s with angle of attack of 0°

The range of Reynolds number is 2.8e4 – 1.3e5 when wind tunnel testing is conducted using the small-scale morphing spoiler. Based on the force coefficients at the low range of Reynolds number, Reynolds independence value is assumed including the force coefficients at real-scale vehicle (Fig. 3-23). The aerodynamic forces on real vehicle is calculated under consumptions of Reynolds independence conditions using below equations ($C_{L_P} = -0.35$, $C_{D_P} = 0.28$).

$$Re_P = \frac{\rho_P u\infty_P W_P}{\mu_P}$$

$$F_{L,\,D_P} = \frac{1}{2}\rho_P u\infty_P^2 A_P C_{L,\,D_P}$$

where Re_P is Reynolds number at real-scale vehicle, ρ is air density, $u\infty$ is the wind speed, μ is air viscosity, W is the width of the vehicle, A is the reference area. Subscripts P represents the real-scale model.

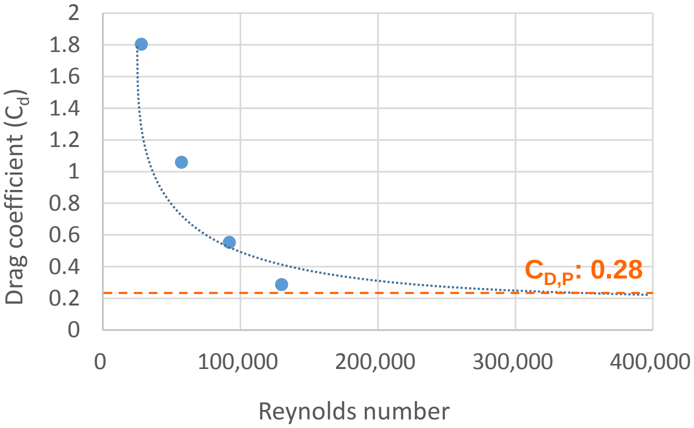

(a) C_D curve for soft morphing spoiler

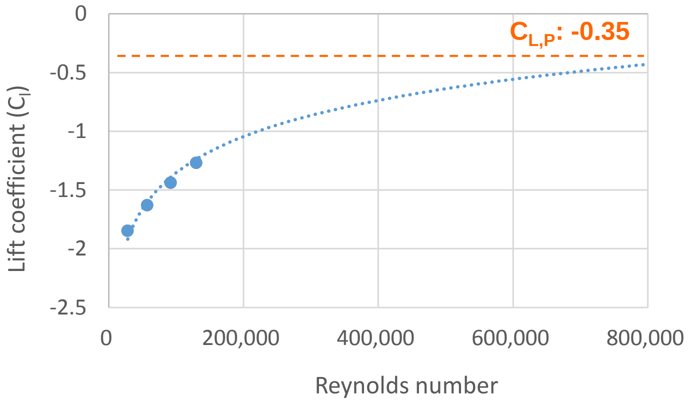

(b) C_L curve for soft morphing spoiler

Figure 3-23. Force coefficients of morphing spoiler

To verify the calculated values of the force coefficients and aerodynamic forces which are occurred by actuation of the morphing spoiler at real-scale model, computational fluid dynamics has been conducted using the fluent in solidworks (Figure 3-24). The simulation and calculation have been conducted in conditions of 40 m/s in vehicle speed. As results, the drag forces (662.01 N at simulation and 661.79 N at calculation) and lift forces (-800.64 N at simulation and -809.89 N at calculation) are showed which has a margin of error of 1 % approximately.

(a) Simulation model for real-scale vehicle

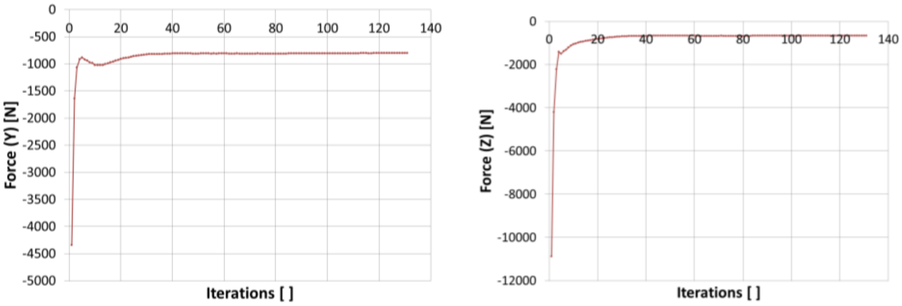

(b) Lift force data

(c) Drag force data

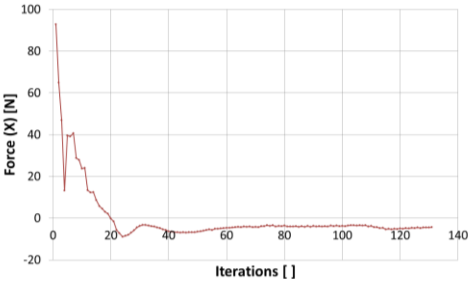

(d) Side force data

Figure 3-24. Details of flow simulations

3.1.6. Conclusions

A woven type smart soft composite (SSC) was fabricated and implemented as a soft morphing spoiler in order to adjust its aerodynamic performance by transforming its shape using a compact mechanism. The woven type SSC which consists of SMA wires for actuation and anisotropic materials to obtain directional properties were embedded together in a flexible polymeric matrix was designed for application in a trailing edge for the rear-spoiler. In this structure, SMA wires were interwoven perpendicularly with glass fibers using a plain weave method. Before curing the soft matrix, to enhance the stiffness of the actuator and to determining the eccentric ratio of the embedded SMA wires, additional lamina of glass-fiber fabric were layered on the woven structure.

The proposed shell-type structure was implemented as the trailing edge of the spoiler of a small-scale car ($\frac{1}{8}$-scale). In this case, one cross-ply glass-fiber fabric was layered on the woven structure in the same direction as the woven fibers to induce an upward directional bending deformation to the woven type SSC for increasing the downforce of the vehicle. Also, the embedded SMA wires were divided into two different current channels to generate a bend-twist deformation intended to increase the yawing moment. To find the effects of the airflow on the generated forces by the morphing spoiler, wind tunnel tests were conducted in an open-circuit bowing-type wind tunnel. The drag force, downforce, side force and yawing moment were measured before and during actuation of the morphing spoiler using a dynamometer connected through a streamlined bar attached at the center of gravity of the model. Test results showed that the proposed structure is capable of large deformations, self-recovery to its original shape, and withstanding the external forces applied through the airflow surrounding the morphing spoiler. Also, for comparison, an airfoil (NACA 0010 shape) was fabricated and tested under the same conditions for various wind speeds, angles of attack, and flap angles. As results of the measurement of the generated forces, the proposed morphing spoiler has better performances in some cases; the negative lift coefficients were higher for most conditions, and the negative C_L/C_D was greater when the angle of attack was larger than 0° for wind speeds ranging from 5 m/s to 20 m/s, even though the drag coefficient was higher than with the airfoil for a flap angle of 0°. Also, the maximum negative C_L/C_D and negative lift coefficient of the morphing spoiler were higher than those of the airfoil.

Lastly, in order to observe the performance characteristics of the spoiler when mounted on the small-scale vehicle, the force coefficients throughout the actuation of the spoiler were measured using wind tunnel experiments at an angle of attack of 0° with a wind speed of 15.8 m/s. The tests showed that the downforce was increased by about -198 % from the spoiler actuation while increasing the drag coefficient by about 41 %.

3.2. Morphing winglets for unmanned aerial vehicles (UAV)

3.2.1. Introduction

Unmanned aerial vehicles (UAVs) are aircraft that are either unpiloted or remotely piloted, and are often used to carry out dangerous or particularly straightforward work. As UAVs are generally designed for specialized missions, unique designs to realize unconventional solutions are often used [66, 67]. Most UAVs operate with a low Reynolds number, and one particular aerodynamic characteristics is that becoming sensitive to airflow when it comes to decreasing its scale because the laminar separation, transition, and turbulence reattachment were occurred within a limited small spaces. To advance the current limits of aerodynamic performance at small scales, various approaches have been reported to improve the aerodynamics of UAVs with low Reynolds numbers, especially using biomimetic, lightweight, adaptive and multifunctional materials and structures [68].

Winglets are known to improve the aerodynamic efficiency by diffusing wing-tip vortices, which generate lift-induced drag. Furthermore, winglets can make the wings non-planar, and act as anterior-most primary feathers of flying birds, which reduce the drag that is induced by spreading out vortices on the wing edge [69, 70]. In the case of UAVs, winglets can be designed for additional functionality, such as yaw control and/or vertical stabilization, as well as to improve efficiency [71, 72].

Richard Whitcomb is credited with identifying the potential practical applications of winglets. His research indicates that fixed winglets exhibit superior performance compared with an extended wing [73]. To minimize tip vortices, a number of studies on the fixed winglet have been reported, considering the geometry, root/tip chord, height (length), taper ratio, and a toe-out (twist), sweep, cant and blend angle [74-77]. Weierman *et al.* [71], and Guerrero *et al.* [74] reported detailed work on the aerodynamic efficiency of various winglet shapes. Nazarinia *et al.* [75] reported an experimental study on changes in the flow field depending on the types of winglet (i.e., spiroid, blended, and winggrid). Multidisciplinary approaches for winglets design were conducted to determine their complex effects on aerodynamic forces in terms of induced profile and total drag, as well as lift and takeoff weight [76, 77].

Variable winglets to control vortex flow have been investigated [47], including active control of multiple winglets [78], where coupled motion resulted in gust alleviation, and hence increased maneuverability. Falcao *et al.* [79] investigated motor-driven winglets capable of rotating independently in two different axes (toe and cant angles), which produced an adjustable response to external aerodynamic loads. Other studies of motor-based deformable winglets investigated the real-time pressure on the upper surface of the wing during actuation of a single wing tip [80] and split wing tips [81] using wind tunnel tests. Daniele *et al.* reported [82] an inflatable system that was fed by pressurized air to realize an adaptable structure.

The desire to adjust to the external environment has led to the concept of morphing structures. Morphing is the continuous change in shape of a single structure with no discrete parts, which can lead to aerodynamic losses due to gap openings in the structure [83]. Most shape-morphing systems consist of smart actuators, which are inspired by the compliant mechanisms of hingeless creatures. This can minimize the stress concentration, and allow multiple functionalities within a single structure [84, 85]. Smart actuators are non-conventional actuators capable of reacting to external stimuli. These devices include shape memory alloys (SMAs) [86] and piezoelectric materials [87], which have both been investigated for applications as variable winglets to improve cruising efficiency. To realize a soft-morphing actuator, a composite actuator combining an SMA, anisotropic materials, and a soft matrix was proposed, which could morph into complex shapes utilizing coupling effects for in-plane, out-of-plane, and twisting deformations [8, 13, 17, 21]. Using the soft-morphing actuator, a variety of new biomimetic applications have been developed at a system level [58, 59].

In this research, smart soft morphing winglets inspired by the tip feathers of gliding birds were designed and implemented on an UAV to observe their effect on the aerodynamic properties of the vehicle. A woven smart soft composite (SSC) material, consisting of SMA wires and glass fibers within a soft polymeric matrix, was used to create a self-actuating soft morphing winglet. To measure the performance characteristics of the morphing structure, beam-type and winglet-shaped actuators made from the woven SSC were built. The end-edge deflection of the composite actuator was measured for various SMA wire diameters and volume fractions of embedded SMA wires, and numbers of glass-fiber fabric lamina. Finally, the resulting winglets were mounted on both wing tips of a small-scale UAV, and the aerodynamic coefficients were measured using an open-blowing type wind tunnel testing for different angles of attack.

3.2.2. Concept of soft morphing winglet

The primary feathers of bird wings contribute to enhanced gliding performance by reducing the drag force, as with winglet systems [88-93]. Among the drag force factors, the induced drag is related to the downwash around the wing caused by the lift force, and typically results in 30–40% of the total drag; a well-designed winglet can have a significant effect on the induced drag [73, 75]. Figure 3-25 shows the aerodynamic forces on a bird during flight.

The soft-morphing winglet was implemented using an SSC wing tip consisting of SMA wires and glass fibers embedded in a soft polymeric matrix. During actuation, the SSC winglets mounted on the wing tips of the UAV bend upwards while the wing body and root are fixed, as shown in Figure 3-26. The advantage of the proposed design is to increase lift with less increase in the induced drag force during flight, given that the unmorphed (flat) and morphed (curved) winglet in various angles of attack. This model allows for a variety of design factors to be controlled, including the tip-chord, height, and taper ratio, depending on the geometry of the winglet. Also, the cant and toe-out angles can be varied depending on the arrangement of the SMA wires and glass fibers in the winglet.

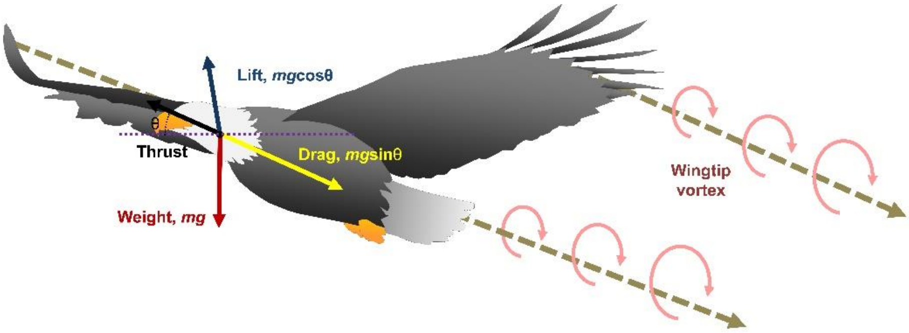

Figure 3-25. Gliding bird with trailing wing-tip vortices

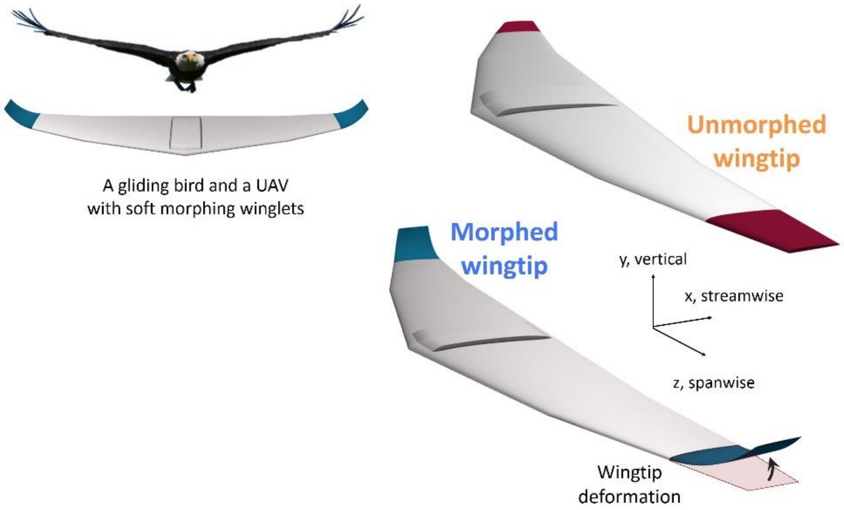

Figure 3-26. Concept of an unmanned aerial vehicle (UAV) with morphing winglets

For actuation of the soft morphing winglet, the woven SSC proposed by Ahn *et al.* was used [17], in which SMA wires are woven with anisotropic fibers and multiple woven layers stacked together. The deformation of the woven SSC can be controlled by varying the stacking conditions, such as the orientation of each ply relative to a reference axis, the number of lamina, and stacking sequence. Figure 3-27 shows the cross-section of the woven SSC used for the soft morphing winglet. Woven SSC actuators have multiple advantages since they form a high-strength structure using a lightweight assembly from being a fiber-reinforced composite consisting of continuous fibers to enhance the strength/stiffness. Also, the soft polymer-based composite resin to make the structure flexible and elastic under bend deflections.

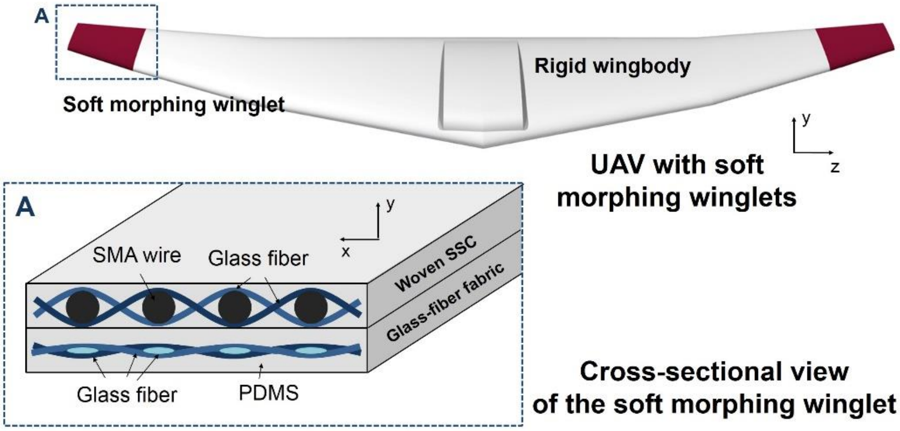

Figure 3-27. Schematic diagram of the morphing winglet and its cross-section

3.2.3. Materials and fabrication

In this study, the glass fibers and the SMA wires were woven together using a handloom which is a weaving device to hold the warp threads (SMA wires) under tension while interweaving the weft threads (glass fibers) by passing them through a space between the fixed threads.

SMA wires (FLEXINOL (Ni: 55 wt%, Ti: 45 wt%) by Dynalloy, Inc.) were used to deform the winglet structure using their phase change properties induced by Joule heating. The contraction and recovery motions of the SMA wires results in a linear strain (4-6%) of the SMA wire [94], which can be converted to a bending deflection depending on the eccentricity ratio of the embedded SMA wires. Table 6 lists the specifications of the SMA wires. Polydimethylsiloxane (PDMS) (Sylgard 184, Dow Corning) was used as the polymer matrix due to its high elasticity, low cost, and fast simple fabrication [95]. To fabricate the actuator, the liquid PDMS was degassed in a vacuum chamber, and poured onto the woven structure. And then, the assembly was placed in a vacuumed bag, and cured at a temperature of 55 ℃. According to its mechanical and thermal properties, it can sustain the mechanical and thermal loads caused by the actuation of the SMA wires without thermoplastic deformation caused by ohmic heating and preventing the separation between the cured PDMS and the embedded fibers caused by the large deflections of the structure. Furthermore, PDMS is electrically insulating, making it suitable as a matrix material to cover the SMA wires. Glass fibers (KN2100 type, KPI Co. Ltd.) were used as an anisotropic material, which were woven with the

SMA wires.

Table 6. Material properties of the SMA wires

Parameter		Value
Young’s modulus [GPa]	Martensite (E_M)	28
	Austenite (E_A)	75
Phase change temperature [°C]	Martensite start (M_s)	52
	Martensite finish (M_f)	42
	Austenite start (A_s)	68
	Austenite finish (A_f)	78

3.2.4. Design and evaluation

To utilize the woven SSC as a soft morphing winglet, its shape trimmed following the taper angle of a rigid wingbody of a small-scale UAV (WASP 4/7 scale). The embedded SMA wires were connected in series, and all components used to form the winglet were covered with PDMS. The fabricated soft morphing winglet is shown in Figure 3-28.

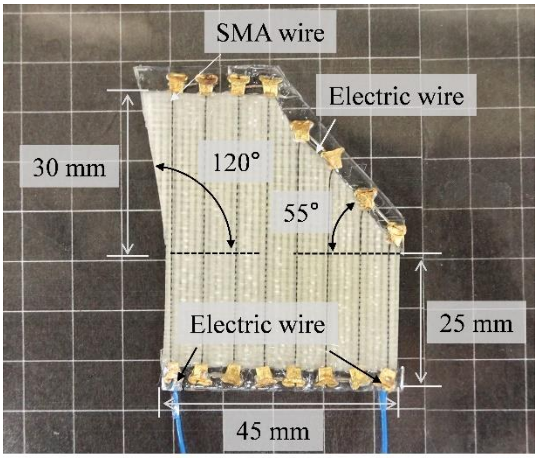

Figure 3-28. Soft morphing winglet formed of the woven SSC with a PDMS matrix

The design parameters that were varied included the number and diameter of embedded SMA wires, and the number of layers of glass fiber fabric lamina in this research. Figure 3-29 shows the initial unmorphed shape of the winglet, as well as the morphed shape following actuation of the SMA wires. When a current was applied to the SMA wires, the tip of the winglet curved upward. After the current was switched off, the winglet recovered to its original shape due to the elastic recovery force of the structure. To investigate the effect on the deformation characteristics of changing the diameter of the SMA wires, actuation tests for the morphing winglet were carried out for three different diameters of SMA wires (200, 250, and 300 μm). The composite actuator was fabricated with four embedded SMA wires with one glass-fiber fabric lamina. Figure 3-30(a) shows the results of the maximum end-edge deflection. The end-edge deflection increased with increasing diameter of the SMA wires; the maximum deflection was 98.6º for the 300-μm-diameter SMA wires.

Also, to achieve a stiffer structure, two layers of glass-fiber fabric lamina were added to the woven structure incorporating 300-μm-diameter SMA wires. The number of embedded SMA wires used for the test is 4 and 8 respectively. Figure 3-30(b) shows the testing results of two layer of glass fiber fabric specimen, and the maximum end-edge deflection was 93º.

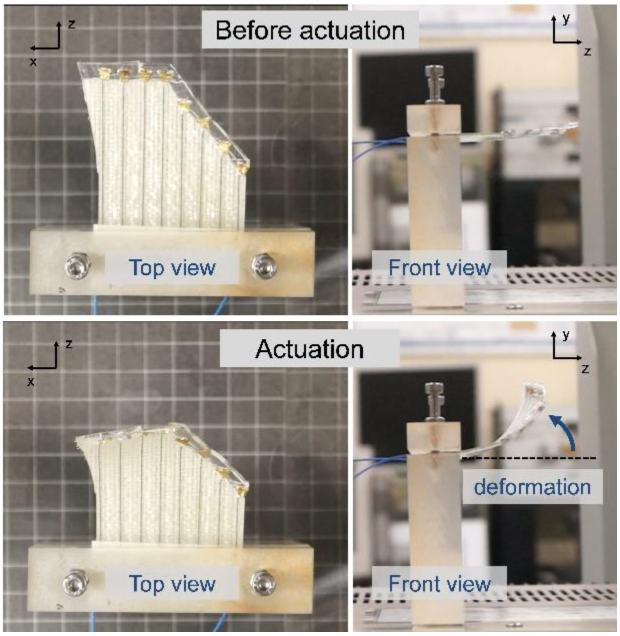

Figure 3-29. Soft morphing winglet with and without a current of 1.0 A;
8 SMA wires embedded in the matrix with two additional layers of glass-fiber fabric

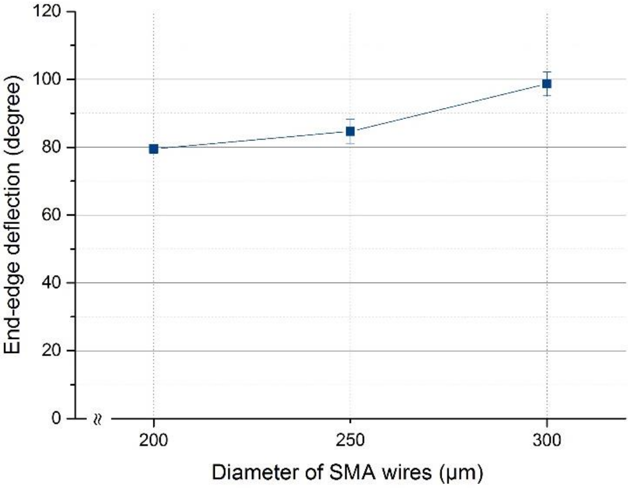

(a) Maximum end-edge deflection as a function of the diameter of the SMA wires with one additional layer of glass-fiber fabric

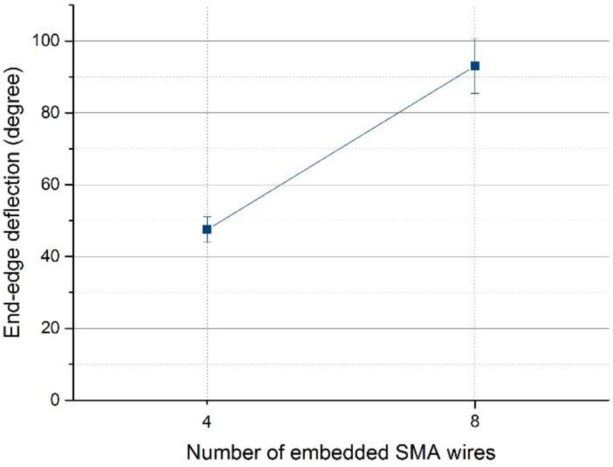

(b) Maximum end-edge deflection as a function of the number of embedded SMA wires with two additional layers of glass-fiber fabric incorporating 300-μm-diameter SMA wires

Figure 3-30. End-edge deflection of the soft morphing winglet

3.2.5. UAV with soft morphing winglets

The aerodynamic forces were measured by mounting the soft morphing winglets on the UAV in a wind tunnel. Experiments were carried out in an open-blowing type wind tunnel and the angle of attack was varied from 2^o to 13^o, in increments of 1^o. The coordinate system was defined as follows: the positive X-axis was in the streamwise direction, the Y-axis was in the vertical direction, and the Z-axis was in the spanwise direction, with the origin was at the center of gravity of the UAV, as shown in Figure 3-31. The winglets were attached to both wing tips, and a load cell for measuring the forces induced by the airflow was connected at the bottom of the UAV via a streamlined bar. The load cell was placed outside of the wind tunnel test section, as shown in Figure 3-32. The dimensions of the test section of the wind tunnel were 0.6 m × 0.6 m. The wind speed for the testing was 15 m/s resulting in a Reynolds number of 9×10^4 based on the chord length. Table 7 lists the dimensions and test parameters used in the wind tunnel experiments.

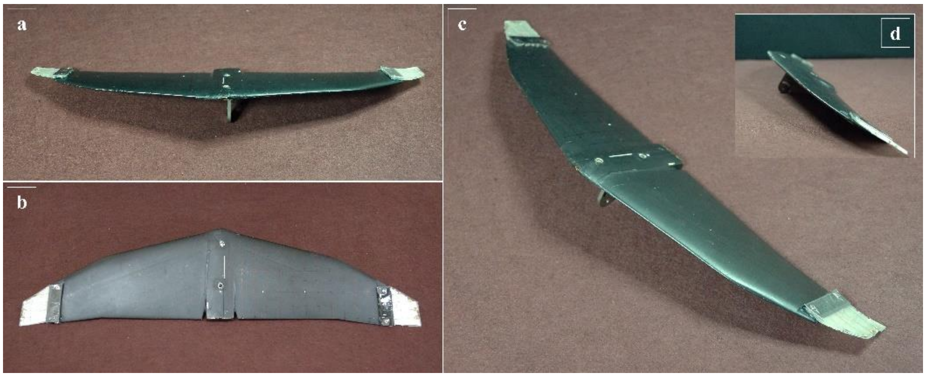

UAV with the mounted morphing winglets; (a) Front, (b) Top, (c) Perspective, and (d) Side view

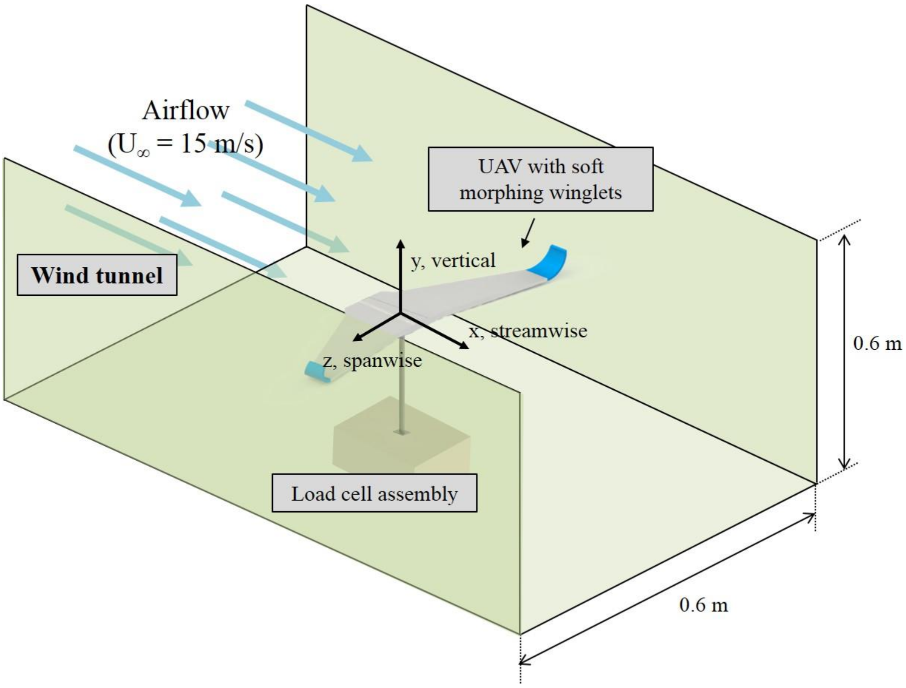

(e) A schematic diagram showing the setup of the wind tunnel test

Figure 3-31. Wind tunnel tests with soft morphing winglets mounted UAV

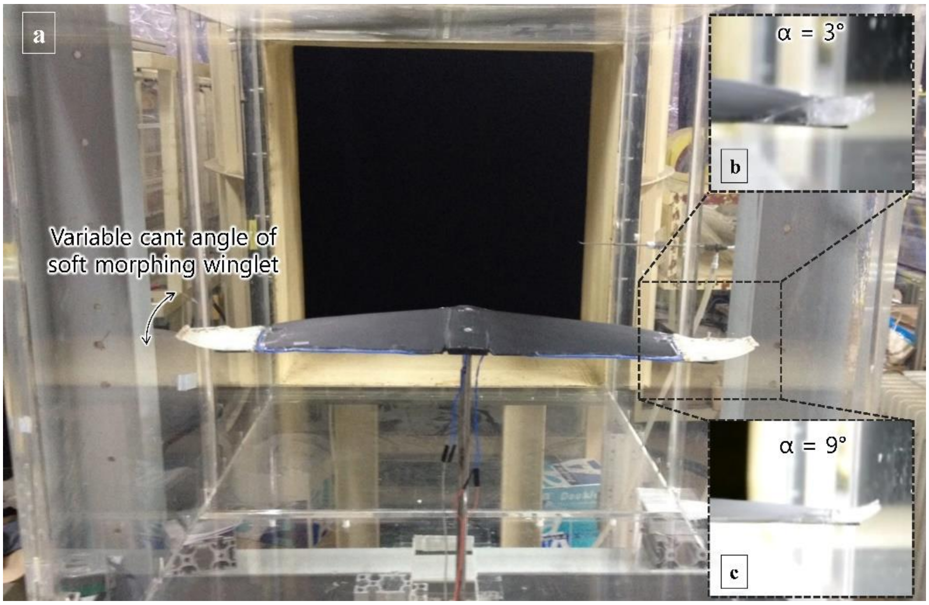

Figure 3-32. UAV with soft morphing winglets (a) Wind tunnel test setup (b,c) Actuating behavior of the morphing winglet with (b) $\alpha = 3^{\circ}$ and (c) $\alpha = 9^{\circ}$ ($U_{\infty} = 15$ m/s, $Re_{chord} = 9\times10^4$)

Table 7. Dimensions and test parameters of the UAV

Parameter	Value
Wing span [mm]	410
Average chord length [mm]	84.7
Mean planform area (unmorphed) [mm^2]	36,959
Mean planform area (morphed) [mm^2]	35,479
Wind speed [m/s]	15
Reynolds number$_{chord}$	9×10^4

The coefficients of the lift and drag forces were calculated as follows:

$$C_{L,D} = \frac{Force_{L,D}}{0.5\rho u_\infty^2 A} \qquad (10)$$

where L is the lift force, D is the drag force, ρ is the density of air, U_∞ is the wind speed, and A is the reference area. Figure 3-33(a) shows the drag coefficients as a function of the angle of attack. As the angle of attack increased, the drag coefficients become steadily larger for both the unmorphed and morphed shape, and the results show that the morphed wingtip has a lower drag coefficient for $\alpha \geq 4°$. By actuating the morphing winglet, the drag coefficients of the UAV decreased by 1.2–4.3% in comparison with the initial geometry, and the maximum difference was 4.3% at $\alpha = 12°$. Figure 3-33(b) shows the lift coefficient as a function of the angle of attack, which increased approximately linearly as the angle of attack increased. The unmorphed wingtip exhibited a larger lift coefficient for $\alpha < 9°$, whereas the morphed winglet showed higher lift coefficients (by up to ~1.6%) for $\alpha \geq 9^o$.

The lift-to-drag ratios (*L/D*) calculated from the lift and drag coefficients of the UAV for the different angles of attack are shown in Figure 3-33(c). For smaller angles of attack, the winglet in the initial geometry exhibited better performance. However, for $\alpha \geq 5^o$, the aerodynamic efficiency was higher with the morphed wingtip. The largest lift-to-drag ratio occurred at $\alpha = 6°$ for both the unmorphed and the morphed geometries, and the maximum *L*/*D* was 14.16 for the morphed wingtip. The largest difference between the unmorphed and the morphed wingtip occurred at $\alpha = 12°$, in which the morphed wingtip showed an L/D approximately 5.8% greater than the unmorphed wingtip.

In the wind tunnel tests, the L/D of the UAV was strongly affected by the angle of attack; however, the morphing winglet provides potential for enhanced efficiency by selecting better efficient wingtip geometry based on the angle of the UAV. Although, the wind tunnel tests consider only the case of gliding flight of the UAV, whereby the airflow is in the steady state, the morphing winglets provide the scope to regulate the aerodynamic performance by choosing either the unmorphed or morphed geometry. Based on these wind tunnel tests, we may conclude that the efficiency of the UAV may be enhanced through the use of the unmorphed (flat) wingtip geometry for $\alpha < 5^{o}$, and the morphed geometry for $\alpha \geq 5^{o}$. By selecting the shape of the wing tips considering the flight angle, soft morphing winglets mounted on a UAV shows a better performance in comparison to a UAV with fixed winglets.

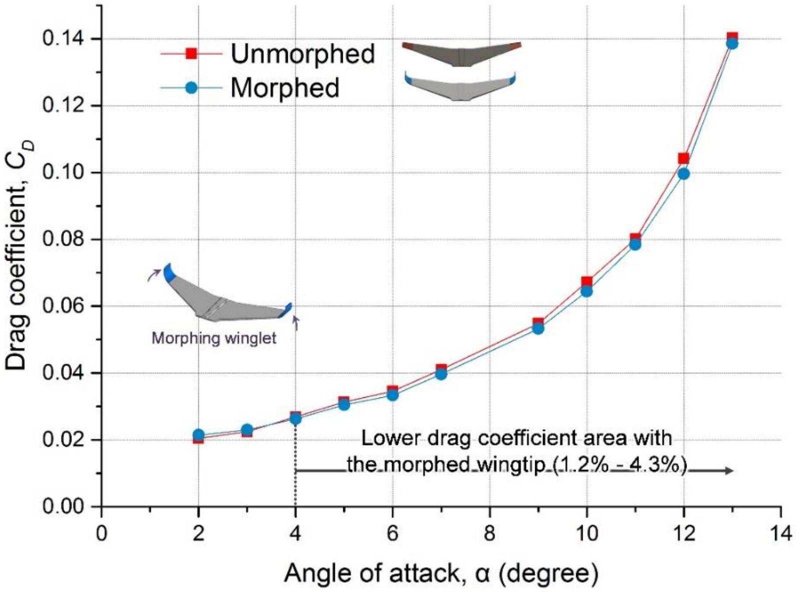

(a) Drag coefficient as a function of the angle of attack

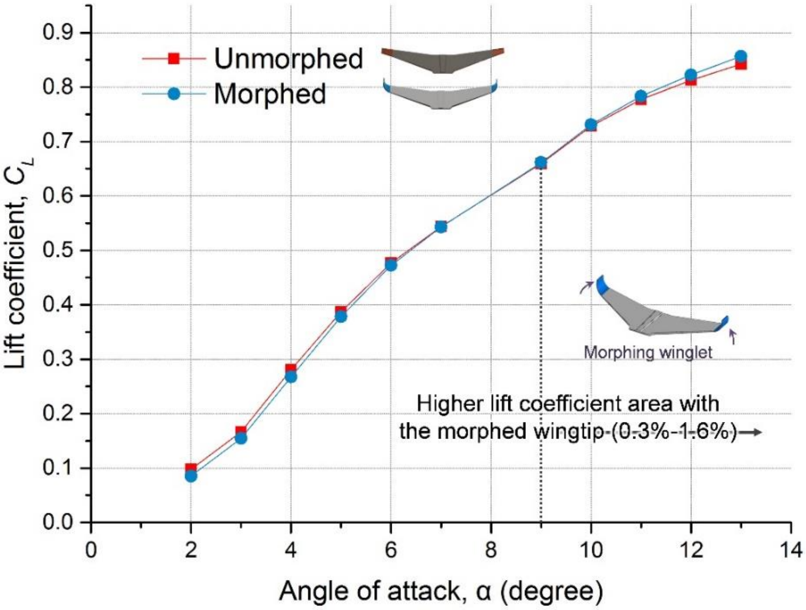

(b) Lift coefficient as a function of the angle of attack

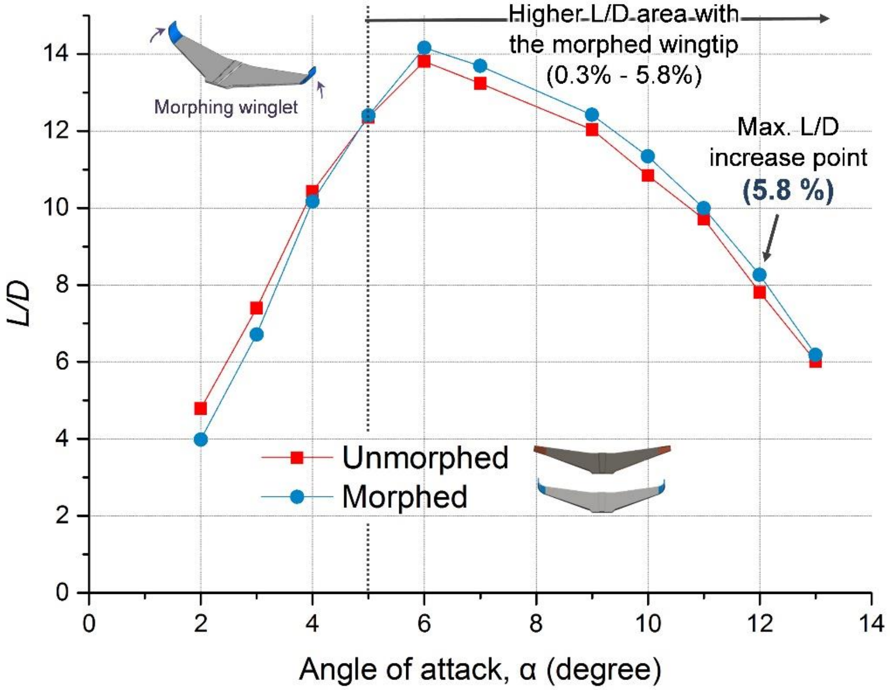

(c) Lift-to-drag ratio as a function of the angle of attack

Figure 3-33. Wind tunnel test results of UAV

3.2.6. Conclusions

Winglets are an aerodynamic devices capable of reducing the lift-induced drag left in the vortex by spreading vortices at the edge of the wingtip both horizontally and vertically. By utilizing the variation of the air flow caused by the winglet, aerial vehicle have improved flight efficiency with regards to fuel consumption, flight speed and flight range. In particular, winglets with a variable cant angle are considered for optimizing the aerodynamic efficiency for a wide range of flight conditions.

In this study, soft morphing winglets were developed using a woven SSC structure incorporating SMA wires, and the structures were mounted on both wingtips of a small-scale UAV. The winglet was designed for morphing its shape smoothly between the unmorphed (flat) and morphed (curved) geometries to adjust itself for optimized flight conditions by mimicking the primary wing-tip feathers of gliding birds.

To determine the flexural stress–strain relation of the woven SSC, three-point bending tests were carried out for different beam-type actuator configurations in terms of the diameters of SMA wires and the number of layers of glass fiber fabric. Also, winglet-shaped composite structures were fabricated, and tests were carried out with various diameters of SMA wire, numbers of embedded SMA wires, and numbers of glass-fiber fabric lamina. Furthermore, to investigate the aerodynamic forces, wind tunnel experiments were conducted with the soft morphing winglets mounted on a small-scale UAV in various angles of attack (2° -13°). The wind tunnel tests showed that the morphed wingtip exhibited a lower drag coefficient for angles of attack $\geq$4° and a larger lift coefficient for angles of attack $\geq$ 9°. These aerodynamic forces resulted in an improvement in the *L/D* ratio of up to 5.8% with an angle of attack of 12°, using the morphed geometry. Both wing-tip geometries exhibited maximum *L/D* ratio with angle of attack of 6°, and the morphed geometry provided a higher *L/D* ratio with angles of attack of $\alpha \geq$ 5°, indicating that aerodynamic performance of the UAV can be improved by controlling the wing tip geometry considering the inclined angle of the UAV.

The power supply implementation in an actual UAV will be investigated in future work, which needs to be capable of generating enough power to actuate the soft morphing winglet. Using either or both an independent centimeter-scale battery integrated in the body of the UAV or the same power which powers the UAV will be considered for implementation in a UAV for actual flights.

Chapter 4.

Smart morphing knit*

4.1. Introduction

Soft morphing systems can adapt to external conditions through structural reconfiguration or variation of their mechanical properties [96]. This is because soft morphing structures exhibit curvilinear shape changes, compliant body mechanisms, and continuous movements. The major features are the compliance and softness that allow them to mimic muscle-like biological locomotion, achieving many degrees of freedom compared to traditional robots, and thus defining a new class of soft morphing structures [97, 98].

Recent work has explored the possibility of generating soft morphing actuation based on the methods for designing a structural volume made of : 1) transformable rigid elements that can demonstrate the soft-morphing motion, [99-101] or 2) elastomeric materials in whole or in part [7, 9, 102-110].

These approaches to volume design methods are capable of executing intuitive form of morphing, but are limited in their capabilities of making complex geometries or being mass produced. In rigid mechanical systems, multiple joints or actuators are usually accompanied by a complex control

---

*Chapter 4 and 5 were published as a regular article:
Han, M.-W. and Ahn, S.-H., 2017, "Blooming Knit Flowers: Loop-linked Soft Morphing Structures for Soft Robotics," Adv. Mater., Vol. 29, No. 13, 1606580.

system or feedback sensors. Elastomers typically require custom-designed molds and are made by time-consuming processes, such as casting or multiple assembly steps [106].

In nature, the biological systems often perform the complex soft morphing by self-organization of their hierarchical architectures. Some of the plants generate movements, such as flexing-packing motions, depending on swellable cell layers. This hydro-responsive motion is mediated by the expansion and collapse of each cell [111]. This bottom-up approach, from the cellular activity to the blooming petals, allows the manufacturing of cost-effective soft morphing systems through a simple process.

Here, we introduce a new type of soft morphing structure, in which loop-linked cell structures made from functional fibers allow the creation of three-dimensional morphologies without auxiliary parts or an elastomeric matrix. The structures are entirely made of fibers based on the design methodology of loop patterning, which are distinguished from the existing approaches for volumetric design. The proposed morphing structures enable three-dimensional volumetric transformation through the reconfiguration of the loop geometries using a thermally responsive fiber. A knitting method, in which yarn loops were used to create subsequent loops, was used in the manufacturing process of the smart textile structure. Each of the knitting patterns, which originate from common methods used in the textile industry, demonstrates unique capabilities of generating deformations through smart fiber actuation.

4.2. Design

Knitting, one of the most common fabric production techniques and a process that is useful in the mass-production of three-dimensional figures, is comprised of consecutive rows of interconnected yarn loops that can be stretched in different directions for high elasticity [112, 113]. The characteristics of knitted structures are related to the fiber properties, loop shapes, and loop patterns, all of which affect the elasticity, flexibility, strength, and stiffness of the finalized structure.

In this study, smart fibers were used to form needle and sinker loops, constructed through a combination of the polyester fibers wrapped around a smart material core made of a thermally reactive shape memory alloy (55 wt% Ni and 45 wt% Ti). The wrapped fibers were used to prevent short-circuiting at the points of contact in the looping yarn and to increase the friction coefficient for a stable actuation and fabrication of the complex geometries using knitting methods (Figure 4-1A).

Both knit (*K*) and purl (*P*) loops were used (Figure 4-1B). These loop types are defined by the stitching path of the subsequent loop, either below (*K*) or above (*P*) the previous loop; when the knit structure is flipped and seen from the opposite side, the loop types become reversed. The knitted loops were arranged by suspension in the horizontal (course) or vertical (wale) direction, known as the weft knitting method (Figure 4-1C). The knitted structures showed the outstanding elasticity compared to other types of textiles due to the number of the interdependent loops, in which the space in each loop allows them to be elongated, widened, or distorted by external or internal forces (Figure 4-1D).

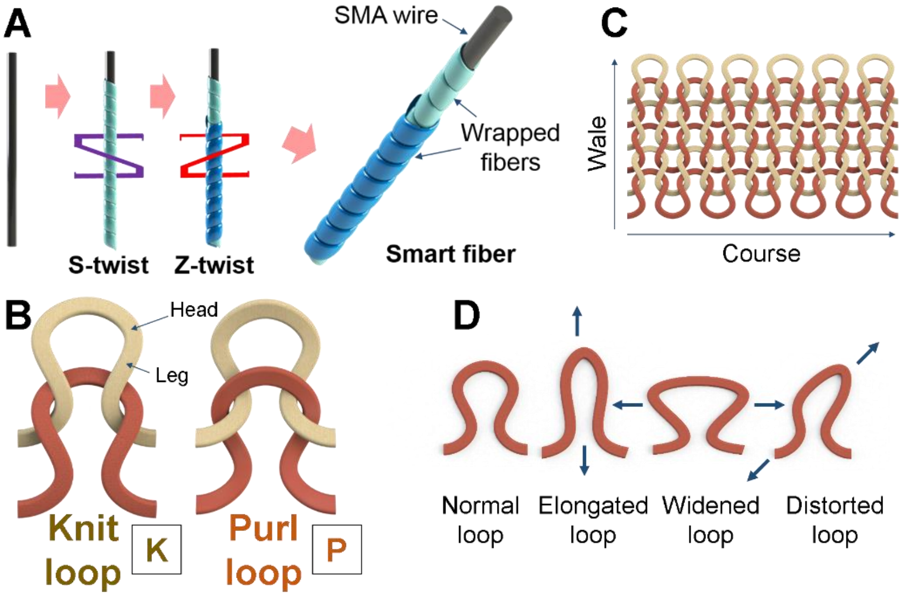

Figure 4-1. Loop-linked soft morphing structure. (A) The smart fiber consists of the polyester fibers wrapped around a SMA core wire. The initial twist for the smart fiber is an S-twist, then the wrapping strands are twisted together in a final Z-twist thread. (B) Knit (*K*) and purl (*P*) loop defined by the subsequent loop passing through from below (*K*) or above (*P*). (C) Knitting fabric with top-side of knit loops. (D) Loop allowing it for elongated, widened, or distorted geometry.

4.3. Materials and methods

Thermally reactive shape memory alloy (SMA) wires (55 wt% Ni and 45 wt% Ti) of 200 μm in diameter were used for the loop-linked soft morphing structures, which were wrapped in commercial polyester fibers (Table 8). By applying an electric current, approximately 0.3 A, the SMA wires were activated, and the SMA materials were transformed from the martensite state to the austenite state. The phase transition allows them to regain their original structural configuration, which causes the lengthwise contraction of the SMA wire of about 4 %. To make the smart fiber, the polyester yarn was rotated in a counterclockwise direction (S-twist) around the SMA wire and then wrapped over the Z-twist fiber with the other polyester yarn in a clockwise direction (Z-twist) (Figure 52A). This double covering, wound in opposite directions, provides the fiber with an equilibrium condition of internal forces [97, 102]. The SMA wire has a consistent resistance per length following its inherent properties. In this study, the SMA wire, which has a resistance of 29 Ω per meter, was used for the proposed configuration and the total energy consumed is estimated to be approximately 80 J for the cylinder model consisting of 132 loops.

Table 8. Material properties of polyester yarn

Specification	Unit	Value
Melting point	[K]	490
Tensile Strength	[MPa]	210
Linear mass density	[Denier] (Weight in grams of 9,000 meters)	150

4.4. Modeling of a unit loop

To observe the deformation of a unit loop, the loop deformation has been simulated using the constitute model for SMA material. The loop-linked structure has an operational states by deciding the material phase and its transformation rate. By transformation of shape memory alloy wire, the knitted loop generates a moment and tension forces which are related with the looping geometry. To determine stress-strain relations during phase transformation from austenite state to martensite state, Brinson model and reverse kinematics are used based on following equations (Figure 4-2 and Figure 4-3).

$$\sigma = E\varepsilon + \theta_T T + \Omega\xi$$

$$\xi = \frac{\xi_0}{2}\left\{\cos\left[\alpha_A\left(T - A_S - \frac{\sigma}{C_A}\right)\right] + 1\right\} \quad \text{for } C_A\left(T - A_f\right) < \sigma < C_A(T - A_S)$$

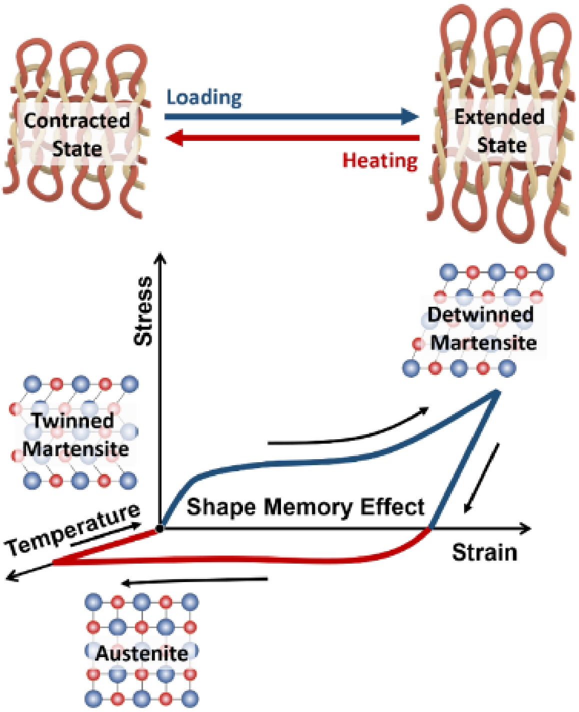

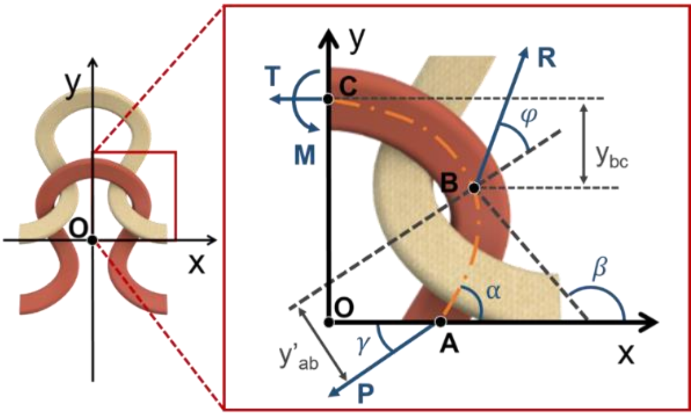

Figure 4-2. Geometry of a knitted loop

$$R_Y = R\sin(\beta - (\pi/2) + \varphi) = P\sin\gamma,\ \ R_X = R\cos(\beta - (\pi/2) + \varphi)$$

$$k_1 = \cos\gamma + \sin\gamma \cdot \tan\beta, \quad k_1' = \cos\gamma + \sin\gamma \cdot \tan(\beta + \varphi)$$

$$M = P(y_{AB}' + k_1' y_{BC})$$

$$T = -Pk_1'$$

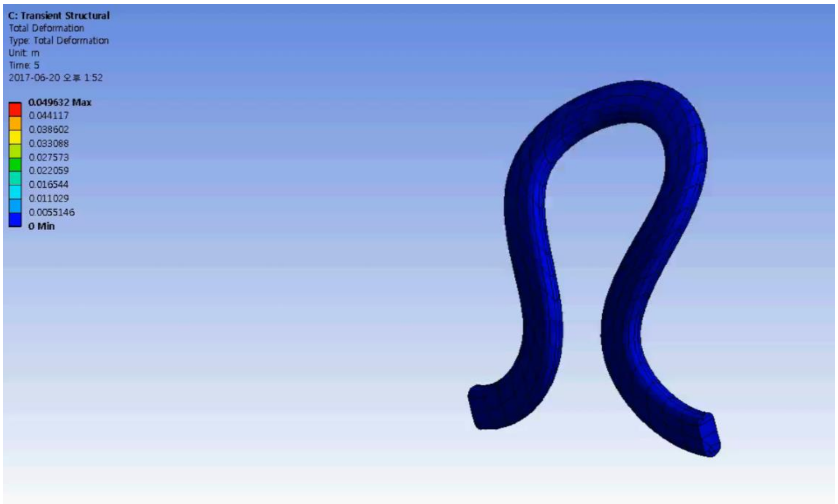

C: Transient Structural
Total Deformation
Type: Total Deformation
Unit: m
Time: 5
2017-06-20 오후 1:52

(a) Before actuation

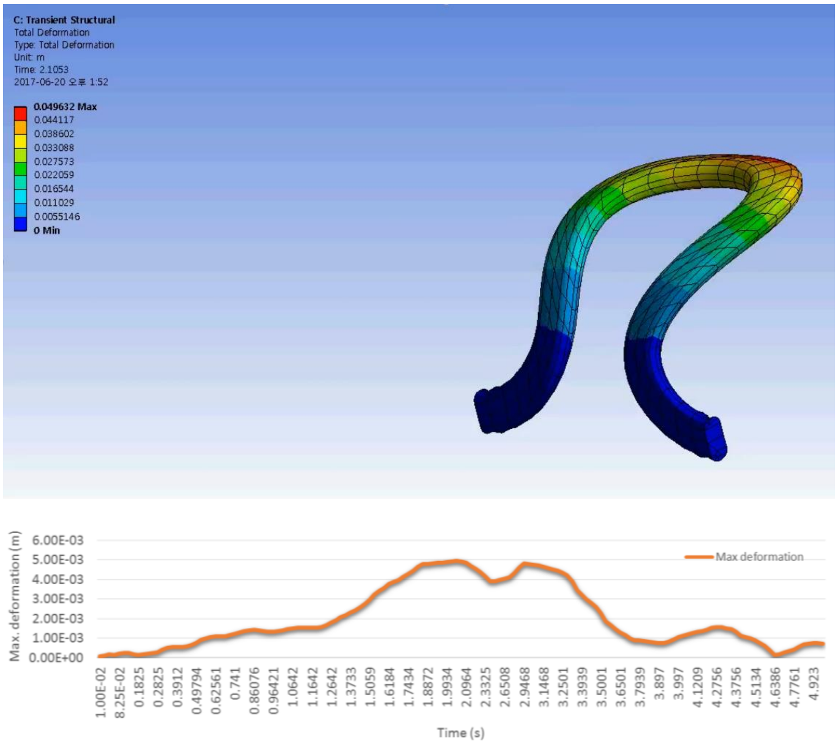

(b) Maximum actuation

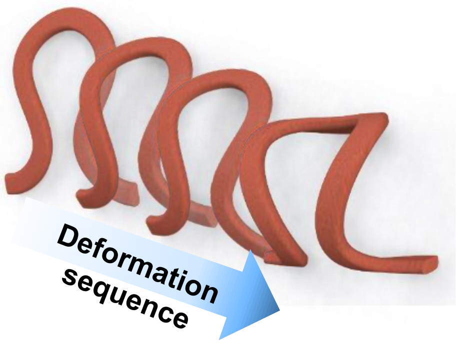

(c) Deformation sequence

Figure 4-3. Simulation result of a unit loop

4.5. Performance evaluation

The application of electric current, approximately 0.3 A, to an SMA wire causes it to transition its phase from martensite state to austenite state, resulting in the contraction of the wire. This phase transition allows the wire to regain its original structural configuration, which causes the lengthwise contraction by about 4 % of its total length. The shape of the loop-linked soft morphing structure was reconfigured by the lengthwise contraction and the morphed shape was defined in conjunction with the loop conditions.

4.5.1. Modes of actuation

The two basic knitted loop types (knit and purl) were used to make four knitting patterns (plain, garter, rib and seed patterns), each comprising of different stitch combinations: The plain pattern was made by a single type of loop (knit or purl). The garter pattern had one or more wales that alternated knit and purl loops. The rib pattern was produced by alternating courses of knit and purl loops. The seed pattern alternated knit and purl loops in the wale and course directions, similar to a checkerboard pattern. From these four primary patterns, two-dimensional open-geometric shapes of loop-linked soft morphing structures with unconstrained edges were fabricated as shown in Figure 4-4.

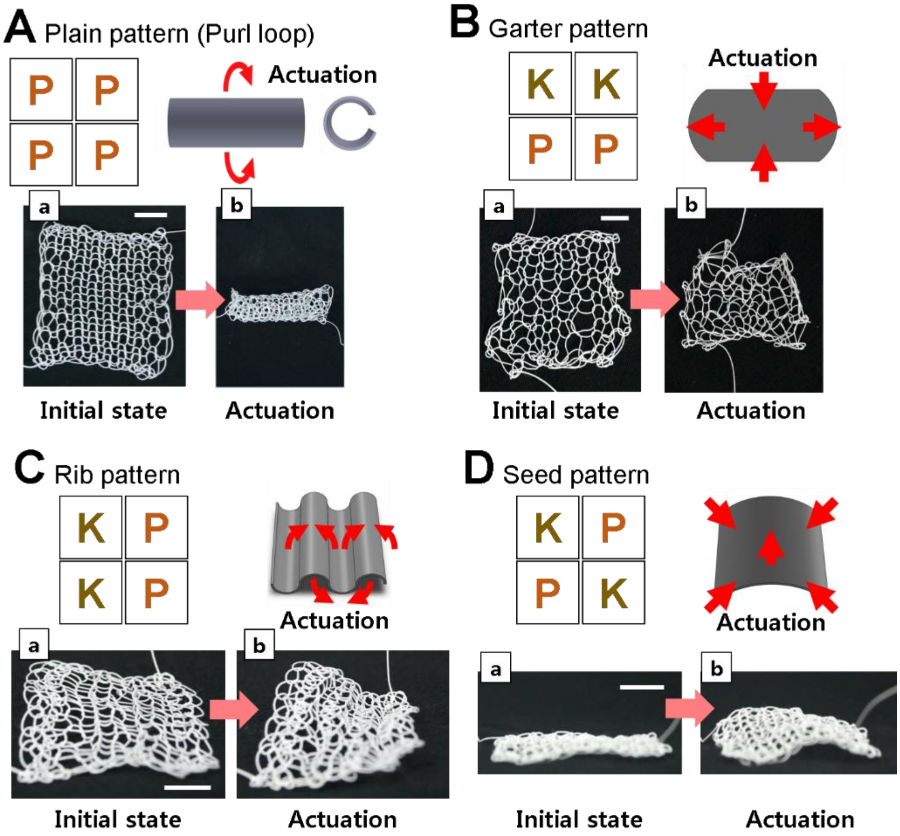

Figure 4-4. Two-dimensional open-geometry. The four types of knitting patterns (plain, garter, rib, and seed patterns). (A) Knitting code for plain pattern with purl loops facing upper side. The structure deforms in a rolling motion after heating the SMA wire. (B) Garter patterned structure and its deformation shows planar deformation. (C) 1 X 1 ribbing pattern has vertical stripes alternating with columns of each loops type. (D) 1 X 1 seed pattern has little bumps on the surface created by alternating knit and purl loops horizontally and vertically. It deforms in a convex geometry. Scale bars, 10 mm.

The loop-linked soft morphing structures that were produced using a plain pattern are shown in Figure 4-4A. The knitted structures had a single loop type (knit or purl) on each side of the fabric and was able to demonstrate a curling motion with purl loops facing outwards when the SMA was heated above the austenite temperature. This is due to the inherent tendency to curl inwards when the purl face is pointing outwards due to the asymmetry of the loop arrangement. When forming knit loops by the plain method, the head of each loop tended to curve towards its legs due to the yarn twisting as the loop passed through the upper side of the previous loop in the wale direction, whereas the legs of the loop tended to curve toward the knit loop side in the course direction. In addition, the elasticity of the loop structure that allowed the expansion or contraction of the SMA wire was greater in the wale direction than in the course direction. As a result, the plain pattern was deformed in a rolling motion after the SMA wire was heated.

The garter patterned structure exhibited planar deformation, as shown in Figure 4-4B. The knit and purl loops were linked alternately in the wale direction, in which the symmetric architecture caused the compensation of the deformation in the out-of-plane direction. Furthermore, owing to the difference in the elastic capacity between the loop orientations, the structure showed a larger contracted length in the wale direction when the SMA wire was actuated.

The rib structure, which has a vertically striped appearance due to the alternating columns of knit and purl loops, demonstrated a waved surface in the course direction as shown in Figure 4-4C. In the seed pattern, a convex shape was induced at the center of the knitted patch through the stress concentration caused by synchronous contraction of the SMA wire (Figure 4-

4D).

Three-dimensional structures based on the previously introduced patterns were created to verify the extent to which the volume of a cylinder could be changed. The basic patterns were connected in horizontal (Figure 4-5) or vertical orientations (Figure 4-6) to create ten closed-shape models, in which the edges of the loops were linked perpendicularly to the ground.

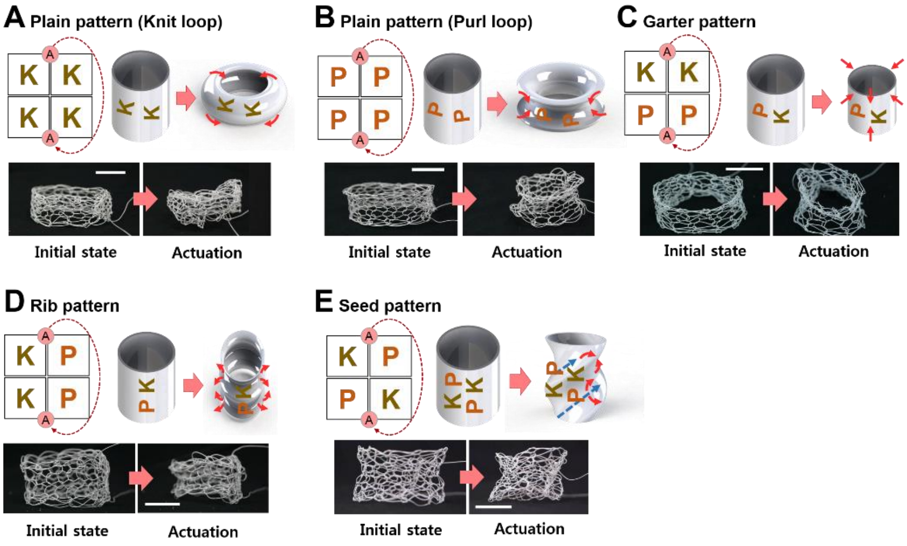

Figure 4-5. Three-dimensional closed-geometry. Cylindrical shape consisting of 132 loops linked horizontally (6 loops in the course and 22 loops in the wale direction). (A) Plain patterns with knit loops on the outside surface deforms in toroidal shape. (B) Hourglass figure shows in plain patterns with purl loops on the outside. (C) Garter cylinder reduced both the diameter and height. (D) 1X1 ribbing cylinder shows the waving surface in vertical direction. (E) The valleys in diagonal direction is shown in seed structure.

The plain knitted structures, in which the loops were connected horizontally, deformed to a toroidal shape with knit loops on the outside surface, and to an hourglass figure when the purl loops on the outside were contracted around the centerline of the cylinder (Figure 4-5A and 4-5B). Both diameter and height of the garter pattern cylinder reduced to the extent that it was dependent on the direction of the loops, as shown in Figure 4-5C. The rib-stitched models, comprising of alternating loop types in the course direction, showed the repeating surface in the vertical directions with alternating arches in the course direction (Figure 4-5D). Figure 4-5E shows the diagonal transformation behavior of the seed patterned cylinder structures.

The behaviors of the knitted structures comprising of consecutive rows of interlocked loops in two-dimensional plain, garter, rib, and seed patterns were investigated. Based on these patterns, three-dimensional morphing modes were realized through various combinations of patterned architectures. To fabricate the three-dimensional geometries using looping patterns, the basic patterns were connected in horizontal (Figure 4-5) or vertical (Figure 4-6) orientations.

As results of the SMA transformation, the vertically connected model formed an hourglass when knit loops were on the outside (Figure 4-6A), and a toroid when the purl loops were on the outside (Figure 4-6B). The garter pattern structures showed the reduction in the diameter and height of the cylindrical structure by contraction of the SMA wire, as shown in Figure 4-6C. The cylinder with ribbing patterns demonstrated the repeating waves in horizontal direction following the alternating arches made from the valleys resulting from different shapes of knit and purl loops (Figure 4-6D). The embossed surface created by the stress concentration of the ridges of the loops is shown in the seed patterns (Figure 4-6E).

The total length of the smart fiber to fabricate the cylinders was not significantly different among the five patterns (Figure 4-7); however, the direction of the loop connection affected the required length of the fiber depending on the loops linked either horizontally (Figure 4-5) or vertically (Figure 4-6), owing to the closing line for knotting the open-shaped loops.

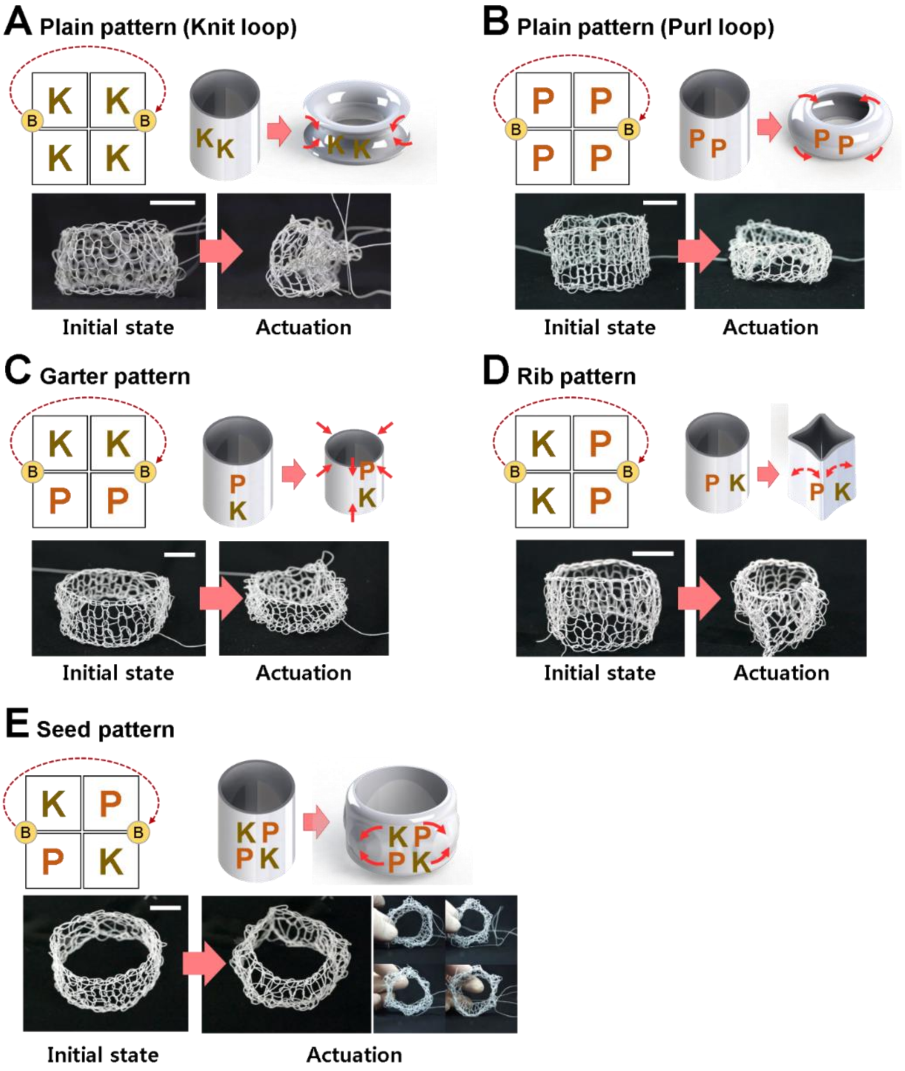

Figure 4-6. Three-dimensional closed-geometry for the loop-linked soft morphing structures in which the loops are connected vertically. Cylinder models consisting of 132 loops linked vertically (22 loops in the course and 6 loops in the wale direction). (A) Plain patterns with knit loops on the outside surface deformed in hourglass shape. (B) Toroidal figure shown in plain patterns with purl loops on the outside. (C) Garter cylinder reduced both the diameter and height. (D) 1X1 ribbing cylinder shows the waving surface in horizontal direction. (E) The embossed surface is shown in seed structure. Scale bars, 20 mm.

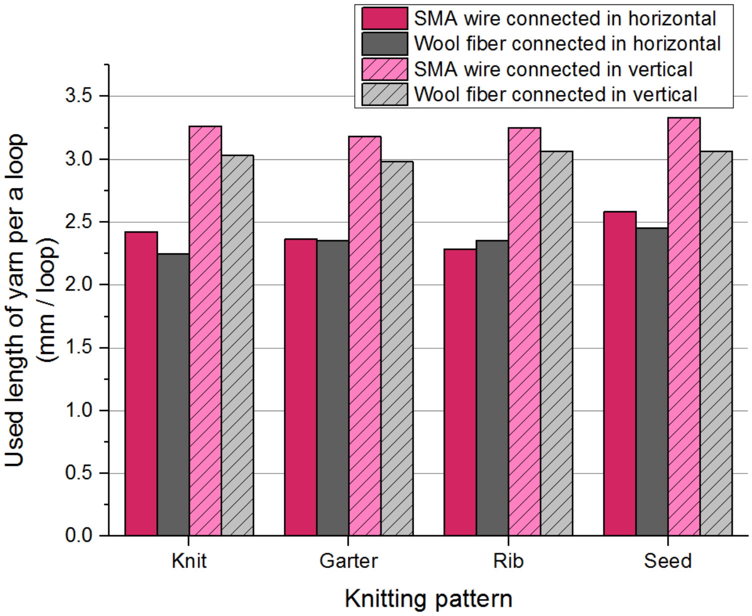

Figure 4-7. Length required to make the loop structures using SMA wire and knitting wool fiber

4.5.2. Actuating force

The cylindrical structures have the characteristic of reconfiguring their shape consistently at austenite state as shown in Figure 4-5A – 4-5E. Even if the structure is deformed at martensite level, the folded structures try to find their memorized geometries at austenite state (Figure 4-8A). This is due to the shape memory effects of the SMA generating the recovery force of the folded structure, which is associated with the looping arrangement. Based on these properties, axial expansion force and axial compressive load of the cylindrical structures (total number of loops was 132, 6 of which were in the course direction and 22 in the wale direction) were measured. The structures were compressed to a height of 1 mm with a compression speed of 10 mm/min.

While maintaining the compressed state, the specimen was returned to a stable point in the martensite state. After reaching the stable states, the electric current was applied to reorganize the shape in the austenite phase. After going through the cooling step, the specimen was reheated using Joule heating. The repeatable blocking force was then measured across heating and cooling states (Figure 4-8B). During the testing, the garter pattern showed the highest blocking force of 10.5 N and the knit pattern showed the lowest force of 5.7 N, which corresponds to a ratio of approximately 0.5 times (Figure 4-8C). These results are related with the expansion force of the loops in the course direction, resulting in upward deployment. The largest compression load, i.e., the force required to compress the cylindrical structure, was measured for the garter and rib patterns (Figure 4-8D). Moreover, the compression tests using various course–wale ratios between 0.25 and 1.00 were conducted with a purl looping structure with the total number of loops equaling about 64 (Figure 4-9).

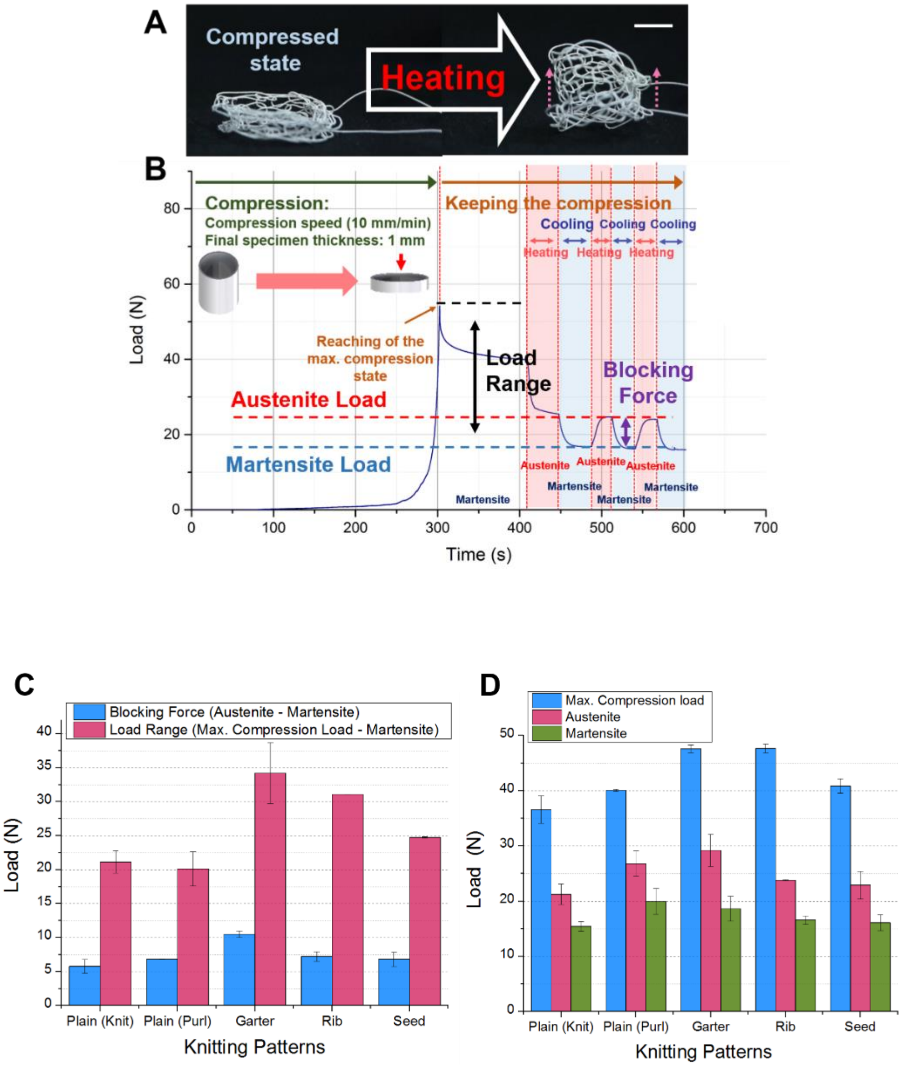

Figure 4-8. (A) Compressed cylinder recovers to its memorized geometry at austenite state (B) Axial expansion forces and axial compressive load are measured by repeating the phase transformation (C) Blocking forces are calculated by subtracting martensite load from austenite load. The load range is calculated by subtracting the martensite load from maximum compressive load. (D) Maximum compressive load for compressing the cylinder to height of 1 mm, stable actuation state at austenite and martensite phase are measured. Scale bars, 20 mm.

The axial expansion force and axial compressive load of the cylindrical structures were measured using an electromechanical universal testing system (Instron, Microtester 5948) (Figure 4-9). The compression tests using various diameter–height ratios were conducted with a purl looping structure fabricated by plain knitting method. The loops of the specimen were linked in the horizontal direction; the course–wale ratios were between 0.25 and 1.00 (A: 0.25, B: 0.38, C: 0.56, D: 0.77, and E: 1.00) with the total number of loops equaling around 64 (Figure 4-9A). To measure the actuating force and the compressive load, the cylindrical structures were placed on a flat fixture and compressed to a height of 1 mm, with a compression speed of 10 mm/min. In the compressed state, an electric current was applied to the specimen to heat the structure and deform the shape, allowing the pressed structure to morph to the memorized shape at austenite state (Figure 4-9B). The detailed steps for measuring the force of the cylindrical specimen are shown in Figure 4-9C, which are the same as the experiment for the force measurement using the cylindrical models with different configurations of the knitting patterns (Figure 4-9).

The maximum blocking force was measured to be 13.6 N for the E-type specimen and the range of the load for A-type was approximately 12.6 N, which was lower than the E type (approximately 4 times) as shown in Figure 4-9D. The A type required the smallest force to compress its own structure, approximately 3 times lower than the E type, while the lowest martensite force of 10.9 N and austenite force of 13.3 N which corresponds to a ratio of approximately 2.5 times and 3 times lower. The results are shown in Figure 4-

9E.

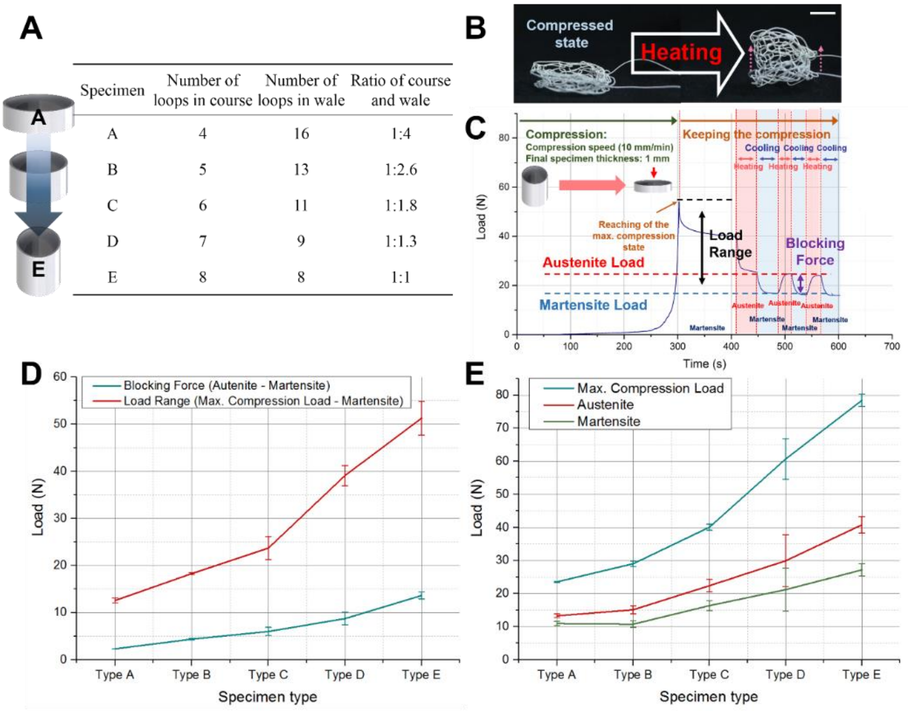

Specimen	Number of loops in course	Number of loops in wale	Ratio of course and wale
A	4	16	1:4
B	5	13	1:2.6
C	6	11	1:1.8
D	7	9	1:1.3
E	8	8	1:1

Figure 4-9. Force measurement of three-dimensional closed-geometry with different ratios of the course-wale. (A) Cylindrical shape consisting of around 64 loops linked in horizontally. The course–wale ratios are between 0.25 and 1.00 (A: 0.25, B: 0.38, C: 0.56, D: 0.77, and E: 1.00). (B) Shape recovery of the compressed cylinder to the memorized shape by the shape memory effect. Scale bar, 20 mm. (C) Testing procedure for the force measurement (D) Measurement of the blocking forces and the range of the load. (E) Maximum compression load and forces at the austenite and martensite phase.

4.5.3. Long-term actuation

The knit actuator consisting of 132 loops linked horizontally is prepared to observe the performance behaviors in the long-term actuation. The loops of the knit actuator are arranged in the course of 6 loops and 22 loops in the wale direction. The detailed steps for measuring the repeatable forces of the cylindrical specimen are the same as the experiment for the force measurement using the cylindrical models with different configurations of the knitting patterns. As results, the average load range in response to heating the actuator was seen to be constant over the 12,000 cycles with a decrease of average load approximately 8%. The average load range is calculated by subtracting the martensite load from austenite load, which is occurred by the phase transformation. Furthermore, the application of the electrical heating caused a reduction of the average generating forces in the larger number of the actuation cycles, which decrease with actuation cycles to 21% at 12,000 cycles. Figure 4-10 shows the testing results of long-term actuation.

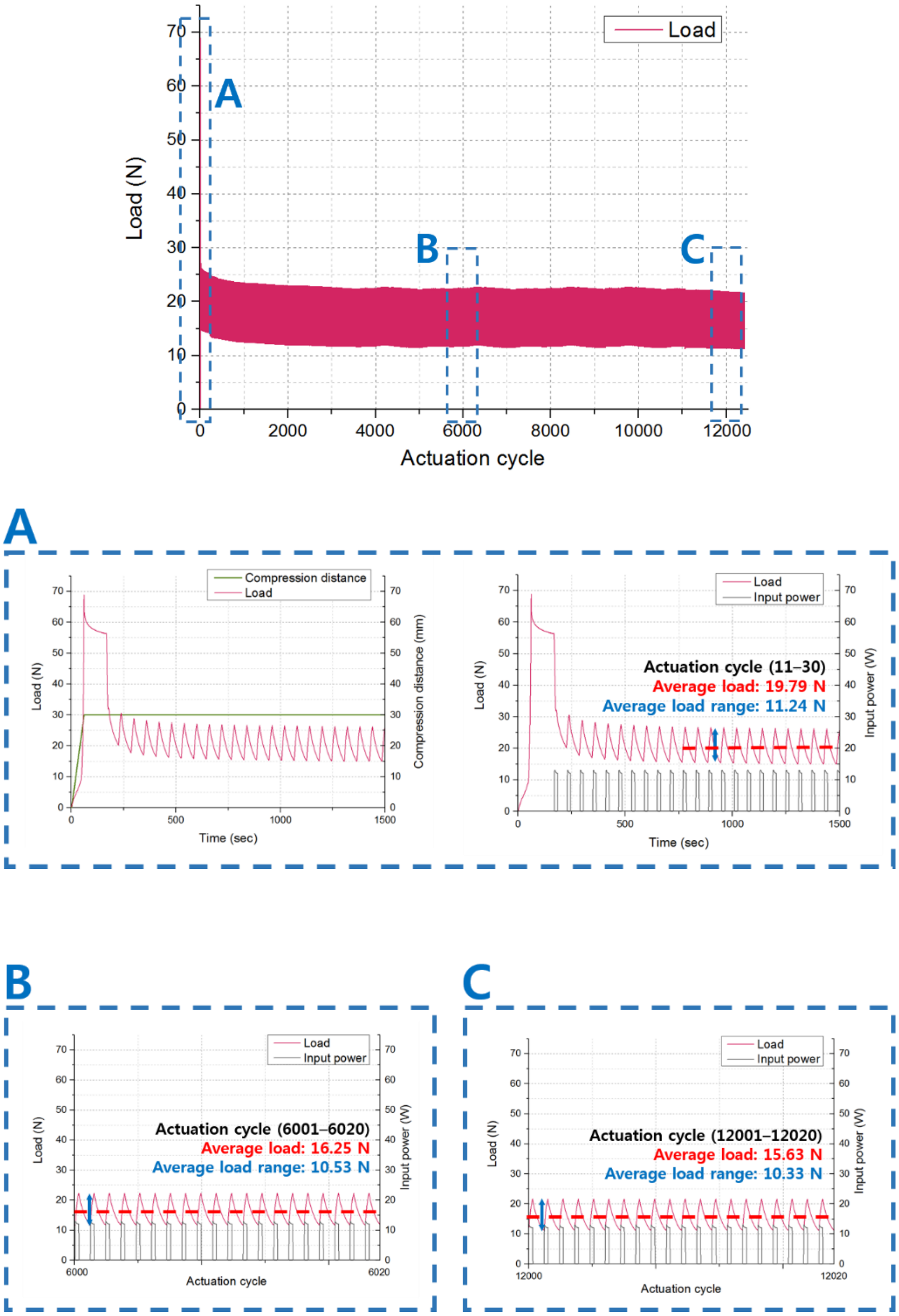

Figure 4-10. 12,000 actuation cycles of knit actuator

Chapter 5.

Applications of knit actuators*

5.1. Blooming knit flowers

The loop-linked method enables the volumetric geometry to be portrayed in a two-dimensional drawing using coded topology. A three-dimensional morphing petal structure (Figure 5-1), comprising of smart and traditional fibers, was designed to verify the ability to actuate a specific area in the knitted structure based on the knitting codes. The center vein of each petal was comprised of purl loops made of smart fibers, with the remainder being fabricated from knit loops of traditional fibers, as shown in Figure 5-1A and 5-1B. When the SMA wire was heated above its austenite temperature, the morphable section made of smart fiber bent downwards, resulting in a concave deformation around the center of the vein, as shown in Figure 5-1B. The morphing flower was comprised of five petals that were used to mimic a lily flower as shown in Figure 5-1C and 5-1D. Each of its petals was able to be actuated by controlling the applying current selectively. By using the knitting methods, other types of flowers, such as a daffodil-like (Figure 5-1E and Figure 5-2,), a gamopetalous (Figure 5-1F and Figure 5-3), and a calla-

---

*Chapter 4 and 5 were published as a regular article:
Han, M.-W. and Ahn, S.-H., 2017, "Blooming Knit Flowers: Loop-linked Soft Morphing Structures for Soft Robotics," Adv. Mater., Vol. 29, No. 13, 1606580.

like flower (Figure 5-1G and Figure 5-4), were made and their blooming motion was demonstrated. Furthermore, morphing flowers were actuated by blowing hot air, about 200ºC, without applying the electric current (Figure 5-5). The SMA is capable of repeated operation, but it has a limited range of actuation such that when implemented to the proposed knitting structure, it is not possible to recover to the original shape by itself. However, by pulling the deformed structure manually, it can recover to its original state, where the actuation cycle can start again from the martensite state. In this study, the proposed knit structures have been designed for one-way deformation, but more experiments would be required to determine their repeatable actuation based on the design strategy for bidirectional motion using antagonistic knit patterns.

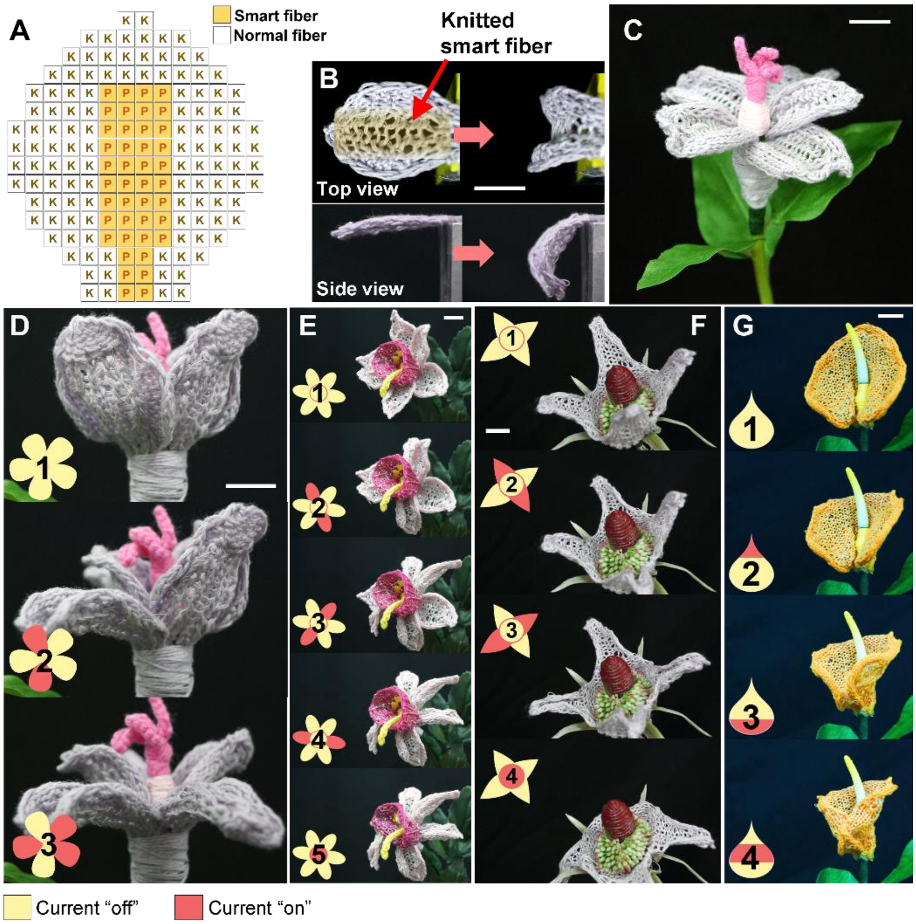

K K
K K K K K K
K K K K K K K K
K K K K K K K K K K
K K K K P P P P K K K K
K K K K P P P P K K K K
K K K K K P P P P K K K K K
K K K K K P P P P K K K K K
K K K K K P P P P K K K K K
K K K K K P P P P K K K K K
K K K K P P P P K K K K
K K K K P P P P K K K K
K K K P P P P K K K
K K K P P K K K
K K P P K K
K K P P K K

Figure 5-1. Morphing flowers. (A) Knitting codes for morphing petal. (B) Deformation of the morphing petal, comprising of smart and normal fibers. (C) A lily-like morphing flower. (D) Deformation sequence of the morphing flower by applying electric current selectively to morph each petal. Each petal has an independent current channel (total of five channels). Step 1 shows the stable state before actuation. Step 2 shows the two petals that are actuated by Joule heating. Step 3 shows that the other three petals are actuated. (E) A daffodil-like morphing flower consisting of six petals and one ovary in a total of seven electrical channels. (F) A gamopetalous morphing flower consisting of six electric channels. Two petals are actuated at once and the electric current is applied to two channels in the receptacle after blooming petals. (G) A calla-like morphing flower having three current channels at the top, middle, and bottom within one petal. Scale bars, 20 mm.

To be expressed in a two-dimensional drawing, the volumetric geometry is enabled using coded knitting topology. Based on the knitting codes, flower-mimic knitting structures, comprising of smart and traditional fibers, were developed and their blooming motions were demonstrated. To fabricate the morphing flower, the knitted structures were made by hand knitting following the knitting codes.

In Figure 5-2, a daffodil-like morphing flower consisting of six petals and one ovary with a total of seven electrical channels was shown with its morphing sequence actuated by the electric current for heating the petals and the ovary. Each of the six petals have their own electric current channel through the knitted smart fiber, which is positioned at the center of the petal to morph the petal backwards with concave deformation around the center of the vein. The ovary is composed of the smart fiber and traditional fiber in cylindrical shape in which the loops were connected vertically. In the morphing sequence, step 1 shows the state before actuation. Steps 2 to 4 demonstrate the petal deformation by actuating two petals at a time. Step 5 shows the ovary actuation, which forms an hourglass figure when contracted around the centerline of the ovary.

A gamopetalous morphing flower consisting of six electric channels, four petals, and one receptacle is shown in Figure 5-3. This flower was made from a single knitted structure. The petals, composed of smart and traditional fibers and knitted by the plain method, were extended from the receptacle structure. The receptacle has two electrical channels divided by different smart fibers, which were arranged in wale direction. Morphing step 1 shows the flower without actuation. In steps 2 to 3, the electric current was applied to two opposite side of petals, resulting in a concave deformation around the vein centerline. Step 4 shows the deformation results by heating the receptacle to make a motion for a full bloom.

The Figure 5-4 shows a calla-like morphing flower comprising three current channels at the top, middle, and bottom within one petal, which consist of a single type of loop patterned by plain knitting with smart fibers. Even if the loops were patterned in the same knitting method, the deformation behaviors of each morphable section were defined in conjunction with the loop conditions such as the ratio of course and wale loops, the constraint points affecting the loop actuation, open edge conditions, and balance with the non-actuating fibers. In this flower, the upper side of the morphing section tended to bend backwards due to SMA contraction, while the middle and bottom of the morphable section were deformed in a rolling motion around the stigma. Morphing sequence depended on the order in which the current was applied as shown in Figure 5-4C and 5-4D. The first step describes the morphing flowers without actuation. Step 2 shows the morphing of the second channel, middle of the flower (Figure 5-4C) and upper side of the flower (Figure 5-4D). Steps 3 to 4 show the deformation results by applying current to the rest of the morphing sections.

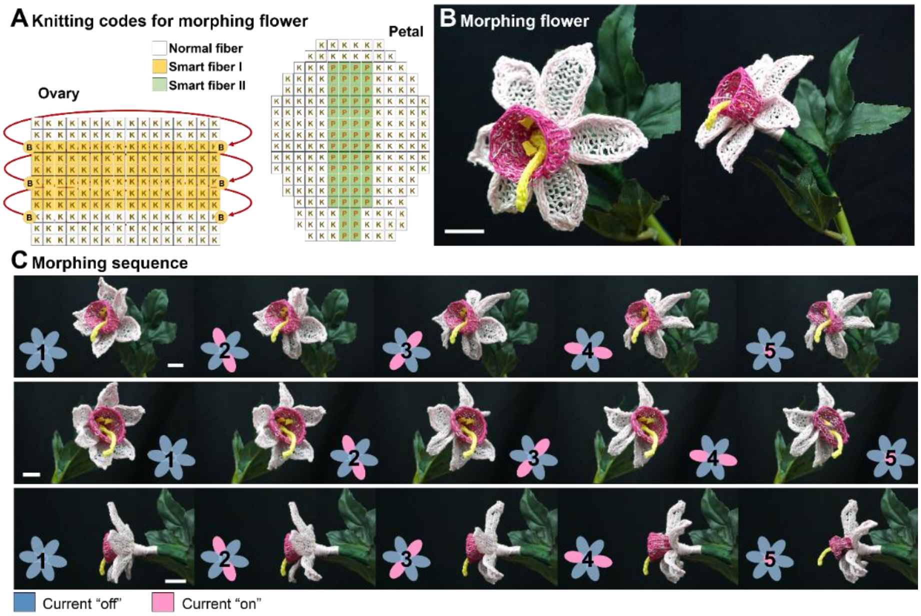

Figure 5-2. A daffodil-like morphing flower consisting of six petals and one ovary. (A) Knitting codes for morphing petal and ovary. (B) A daffodil-like morphing flower. (C) Morphing sequence: before actuation (step 1), actuation of two petals at once (step 2 to 4) and the ovary actuation (step 5). Scale bars, 30 mm.

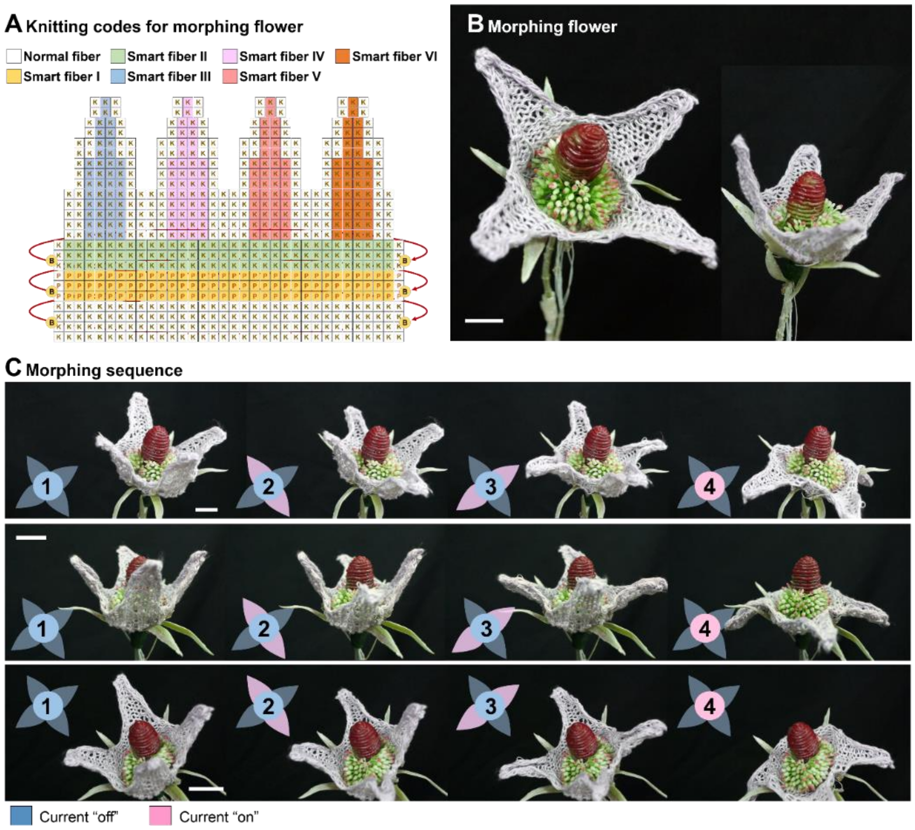

Figure 5-3. A gamopetalous morphing flower consisting of six electric channels, each petal has its own channel and two channels exist in the receptacle. (A) Knitting codes for morphing flower. (B) A gamopetalous morphing flower. (C) Morphing sequence: before actuation (step 1), actuation of two opposite petals at once (step 2 to 3) and the receptacle actuation (step 4). Scale bars, 30 mm.

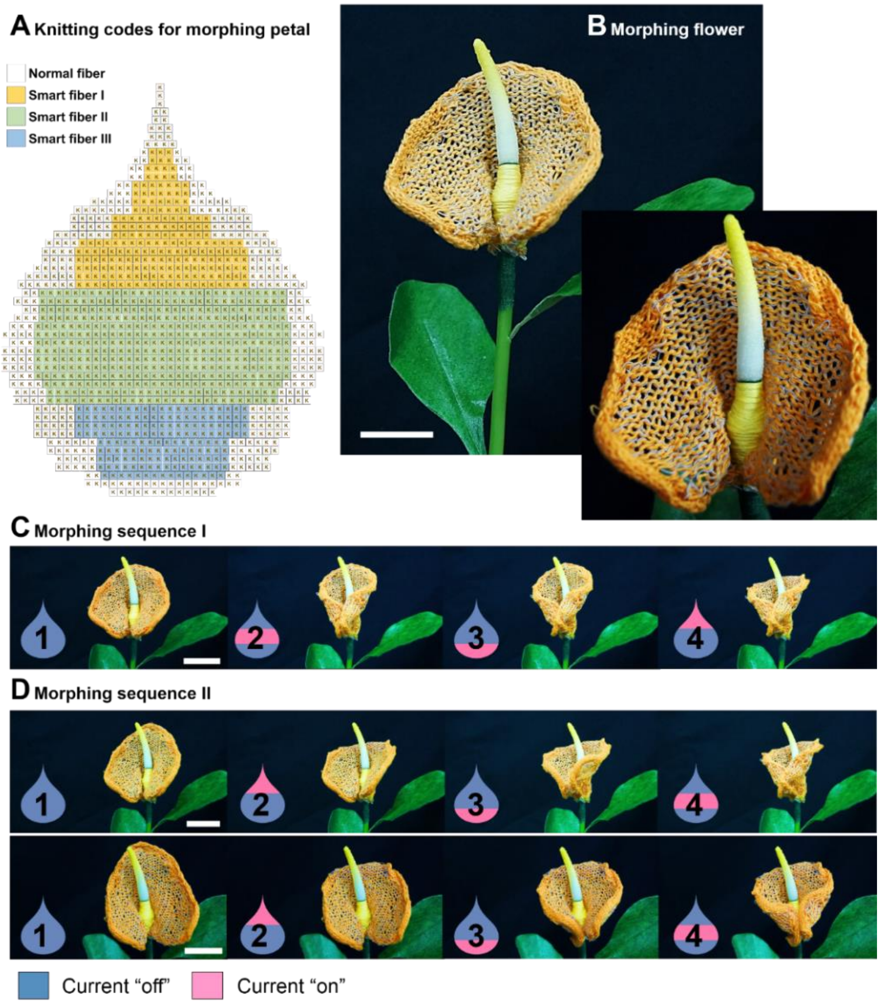

Figure 5-4. A calla-like morphing flower having three current channels at the top, middle, and bottom within one petal. (A) Knitting codes for morphing petal. (B) A calla-like morphing flower. (C) Morphing sequence: before actuation (step 1). actuation of the middle (step 2), bottom (step 3), and upper side of the petal (step 4). (D) Morphing sequence: before actuation (step 1). actuation of the upper (step 2), bottom (step 3), and the middle of the petal (step 4). Scale bars, 30 mm.

The deformation capacity of the SMA wire, which was used for the fabrication of the morphing flower, depends on the phase transition between the martensite and the austenite state, which is affected by temperature and stress. In order to create a morphing motion, a heat gun was used to realize the shape memory effect instead of a current. Around 200ºC of hot air was blown around the flowers and the blooming motions were demonstrated as shown in Figure 5-5.

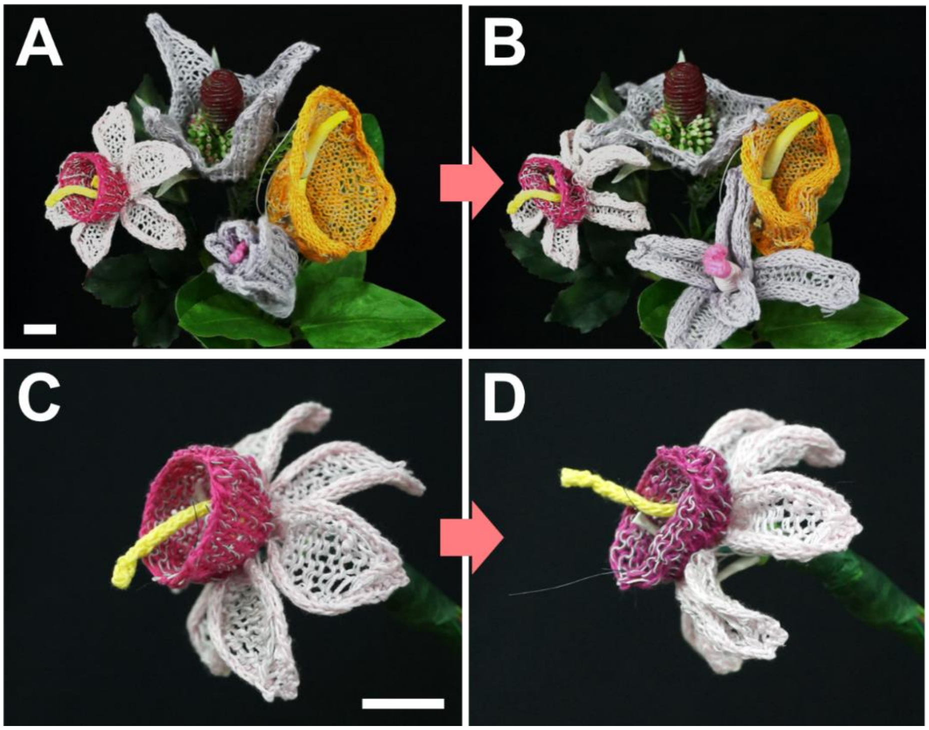

Figure 5-5. Blooming motion of the morphing flowers by hot air blowing. Scale bars, 30 mm.

The loop linked morphing structures show the ability to morph in various modes which can not only be used for bending, twisting, and torsional deformation, but also be used for volumetric transformation. The use of these morphing concepts that rely on the one-dimensional smart fiber and the looping architecture is advantageous in the field of soft actuators in these regards: i) a high degree of flexibility, as knitted structures are formed through looping sequences, with transformable spaces that allow deformation. ii) multi-dimensional continuous morphing, which can be used to create easily deformed surfaces that adapt to planar or spatial features. The range of possible motions includes various transformation modes available in different loop pattern combinations. iii) simple composition with a structure comprising of only fibers without subsidiary elements such as an elastomeric matrix or kinematic parts. iv) one-step fabrication by knitting the fibers, which enables rapid mass production of the morphing structure. v) a wide variety of applications exist in fiber-based structures, including wearable devices, exosuits, and soft robots.

5.2. Wearable applications

A loop-linked structure capable of morphing in various modes including volumetric transformation was developed based on the knitting methods. This loop-based technology is a methodology for soft robotics relying on the entirely one-dimensional fiber without auxiliary parts or elastomeric materials, allowing them to generate morphological transformation including bending, twisting, and torsional deformation. Because a knitting method, in which yarn loops are used to create subsequent loops, was used in the manufacture of a smart textile structure, the looping architecture make it possible to explore applications in the field of wearable applications; for example, the gloves, wrist sleeve, elbow guard, and finger gloves. Figure 5-6 shows the wearable applications using the smart morphing knit actuator.

Figure 5-6. Wearable applications using knit actuators

Chapter 6.

Conclusions

The purpose of this study was to design, fabricate, and evaluate soft morphing textile actuators based on woven and knitted textile structures. Stable and strong modes of actuation were achieved using woven type SSCs as soft morphing wings of a ground vehicle spoiler and as winglets for an unmanned aerial vehicle, allowing control over aerodynamic performance. To confirm the effects of the airflow on forces generated by the morphing wings, wind tunnel tests were conducted with various conditions of angle of attack and wind speed. Also, soft morphing structures capable of morphing into various modes, including volumetric transformation, were developed using a smart morphing knit made from functional fibers, allowing the creation of 3D morphologies. A knitting method was used in the manufacturing process of the smart textile structures, and morphing flowers were fabricated to verify the design methodology of the proposed knit actuation. This new morphing concept, relying on a one-dimensional smart fiber and a looping architecture, is advantageous in the field of soft actuators in terms of i) the high degree of flexibility, ii) multi-dimensional continuous morphing, iii) simple composition, iv) one-step fabrication, and v) a wide variety of fiber-based structure applications, including wearable devices, exosuits, and soft robots.

Bibliography

1. Barbarino, S., et al., *A review of morphing aircraft.* Journal of intelligent material systems and structures, 2011. **22**(9): p. 823-877.
2. Kuder, I.K., et al., *Variable stiffness material and structural concepts for morphing applications.* Progress in Aerospace Sciences, 2013. **63**: p. 33-55.
3. Schultz, M.R. and M.W. Hyer, *A morphing concept based on unsymmetric composite laminates and piezoceramic MFC actuators.* AIAA Paper, 2004. **1806**: p. 19-22.
4. Ossadzow-David, C. and M. Touratier, *A multilayered piezoelectric shell theory.* Composites science and technology, 2004. **64**(13): p. 2121-2137.
5. Kögl, M. and E.C. Silva, *Topology optimization of smart structures: design of piezoelectric plate and shell actuators.* Smart materials and Structures, 2005. **14**(2): p. 387.
6. Lee, J.-G., et al., *Saddle-shaped, bistable morphing panel with shape memory alloy spring actuator.* Smart Materials and Structures, 2014. **23**(7): p. 074013.
7. Chu, W.-S., et al., *Review of biomimetic underwater robots using smart actuators.* International journal of precision engineering and manufacturing, 2012. **13**(7): p. 1281-1292.
8. Rodrigue, H., et al., *Cross-shaped twisting structure using SMA-based smart soft composite.* International Journal of Precision Engineering and Manufacturing-Green Technology, 2014. **1**(2): p. 153-156.
9. Wang, W., H. Rodrigue, and S.-H. Ahn, *Deployable soft composite structures.* Scientific reports, 2016. **6**.
10. Zhou, G. and P. Lloyd, *Design, manufacture and evaluation of bending behaviour of composite beams embedded with SMA wires.* Composites Science and Technology, 2009. **69**(13): p. 2034-2041.
11. Du, X., G. Sun, and S. Sun, *A study on the deflection of shape memory alloy (SMA) reinforced thermo-viscoelastic beam.* Composites science and technology, 2004. **64**(9): p. 1375-1381.
12. Lee, H.J. and J.J. Lee, *A numerical analysis of the buckling and postbuckling behavior of laminated composite shells with embedded shape memory alloy wire actuators.* Smart Materials and Structures, 2000. **9**(6): p. 780.
13. Rodrigue, H., et al., *A shape memory alloy–based soft morphing actuator capable of pure twisting motion.* Journal of Intelligent Material Systems and Structures, 2015. **26**(9): p. 1071-1078.

14. Rodrigue, H., et al., *Effect of twist morphing wing segment on aerodynamic performance of UAV.* Journal of Mechanical Science and Technology, 2016. **30**(1): p. 229-236.
15. Rodrigue, H., et al., *Comparison of mold designs for SMA-based twisting soft actuator.* Sensors and Actuators A: Physical, 2016. **237**: p. 96-106.
16. Rodrigue, H., et al., *SMA-based smart soft composite structure capable of multiple modes of actuation.* Composites Part B: Engineering, 2015. **82**: p. 152-158.
17. Ahn, S.-H., et al., *Smart soft composite: An integrated 3D soft morphing structure using bend-twist coupling of anisotropic materials.* International Journal of Precision Engineering and Manufacturing, 2012. **13**(4): p. 631-634.
18. Song, S.-H., et al., *35 Hz shape memory alloy actuator with bending-twisting mode.* Scientific reports, 2016. **6**.
19. Pinto, F., et al., *Multifunctional SMArt composite material for in situ NDT/SHM and de-icing.* Smart Materials and Structures, 2012. **21**(10): p. 105010.
20. Daghia, F., et al., *Shape memory alloy hybrid composite plates for shape and stiffness control.* Journal of Intelligent Material Systems and Structures, 2008. **19**(5): p. 609-619.
21. Wu, R., et al., *Woven type smart soft composite beam with in-plane shape retention.* Smart Materials and Structures, 2013. **22**(12): p. 125007.
22. Wang, W., H. Rodrigue, and S.-H. Ahn, *Smart soft composite actuator with shape retention capability using embedded fusible alloy structures.* Composites Part B: Engineering, 2015. **78**: p. 507-514.
23. Roh, J.-H. and J.-H. Kim, *Adaptability of hybrid smart composite plate under low velocity impact.* Composites Part B: Engineering, 2003. **34**(2): p. 117-125.
24. Lee, H.-T., et al., *Shape memory alloy (SMA)-based head and neck immobilizer for radiotherapy.* Journal of Computational Design and Engineering, 2015. **2**(3): p. 176-182.
25. Huang, W., *On the selection of shape memory alloys for actuators.* Materials & design, 2002. **23**(1): p. 11-19.
26. Bodaghi, M., et al., *Active shape/stress control of shape memory alloy laminated beams.* Composites Part B: Engineering, 2014. **56**: p. 889-899.
27. Dawood, M., M. El-Tahan, and B. Zheng, *Bond behavior of superelastic shape memory alloys to carbon fiber reinforced polymer composites.* Composites Part B: Engineering, 2015. **77**: p. 238-247.
28. Kim, D.J., et al., *Pullout resistance of straight NiTi shape memory alloy*

fibers in cement mortar after cold drawing and heat treatment. Composites Part B: Engineering, 2014. **67**: p. 588-594.

29. Rosen, A. and O. Gur, *A transfer matrix model of large deformations of curved rods.* Computers & Structures, 2009. **87**(7): p. 467-484.
30. Villanueva, A., et al., *A bio-inspired shape memory alloy composite (BISMAC) actuator.* Smart Materials and Structures, 2010. **19**(2): p. 025013.
31. Smith, C., et al., *Working principle of bio-inspired shape memory alloy composite actuators.* Smart Materials and Structures, 2010. **20**(1): p. 012001.
32. Lu, P., F. Cui, and M. Tan, *A theoretical model for the bending of a laminated beam with SMA fiber embedded layer.* Composite Structures, 2009. **90**(4): p. 458-464.
33. Katz, J., *Aerodynamics of race cars.* Annu. Rev. Fluid Mech., 2006. **38**: p. 27-63.
34. Hucho, W.-h. and G. Sovran, *Aerodynamics of road vehicles.* Annual review of fluid mechanics, 1993. **25**(1): p. 485-537.
35. Zerihan, J. and X. Zhang, *Aerodynamics of a single element wing in ground effect.* Journal of aircraft, 2000. **37**(6): p. 1058-1064.
36. Pelletier, A. and T.J. Mueller, *Low Reynolds number aerodynamics of low-aspect-ratio, thin/flat/cambered-plate wings.* Journal of Aircraft, 2000. **37**(5): p. 825-832.
37. Jung, K.H., H.H. Chun, and H.J. Kim, *Experimental investigation of wing-in-ground effect with a NACA6409 section.* Journal of marine science and technology, 2008. **13**(4): p. 317-327.
38. Ahmed, M.R. and S. Sharma, *An investigation on the aerodynamics of a symmetrical airfoil in ground effect.* Experimental Thermal and Fluid Science, 2005. **29**(6): p. 633-647.
39. Marqués-Bruna, P., *Engineering the race car wing: application of the vortex panel numerical method.* Sports Engineering, 2011. **13**(4): p. 195-204.
40. Zhang, X. and J. Zerihan, *Turbulent wake behind a single element wing in ground effect.* transition, 2002. **1**(1.5): p. 1.6.
41. Ahmed, N. and J. Goonaratne, *Lift augmentation of a low-aspect-ratio thick wing in ground effect.* Journal of Aircraft, 2002. **39**(2): p. 381-384.
42. Plotkin, A. and S. Dodbele, *Slender wing in ground effect.* AIAA journal, 1988. **26**(4): p. 493-494.
43. Zhang, X. and J. Zerihan, *Aerodynamics of a double-element wing in ground effect.* AIAA journal, 2003. **41**(6): p. 1007-1016.
44. Zhang, X., W. Toet, and J. Zerihan, *Ground effect aerodynamics of race cars.* Applied Mechanics Reviews, 2006. **59**(1): p. 33-49.
45. Myose, R., M. Papadakis, and I. Heron, *Gurney flap experiments on airfoils,*

wings, and reflection plane model. Journal of Aircraft, 1998. **35**(2): p. 206-211.

46. Ranzenbach, R., et al. *Multi-element airfoil in ground effect-An experimental and computational study*. in *15th Applied Aerodynamics Conference*. 1997.
47. Cho, S. and H. Choi. *Control of wing-tip vortex using winglets at low Reynolds number*. in *APS Meeting Abstracts*. 2014.
48. Thill, C., et al., *Morphing skins.* The Aeronautical Journal, 2008. **112**(1129): p. 117-139.
49. Hwang, S.-H., H.W. Park, and Y.-B. Park, *Piezoresistive behavior and multi-directional strain sensing ability of carbon nanotube–graphene nanoplatelet hybrid sheets.* Smart Materials and Structures, 2012. **22**(1): p. 015013.
50. John, A., Y. Chen, and J. Kim, *Synthesis and characterization of cellulose acetate–calcium carbonate hybrid nanocomposite.* Composites Part B: Engineering, 2012. **43**(2): p. 522-525.
51. Hou, Y., et al., *Graded conventional-auxetic Kirigami sandwich structures: Flatwise compression and edgewise loading.* Composites Part B: Engineering, 2014. **59**: p. 33-42.
52. Van Humbeeck, J., *Shape memory alloys: a material and a technology.* Advanced Engineering Materials, 2001. **3**(11): p. 837-850.
53. Hartl, D.J. and D.C. Lagoudas, *Aerospace applications of shape memory alloys.* Proceedings of the Institution of Mechanical Engineers, Part G: Journal of Aerospace Engineering, 2007. **221**(4): p. 535-552.
54. Icardi, U. and L. Ferrero, *Preliminary study of an adaptive wing with shape memory alloy torsion actuators.* Materials & Design, 2009. **30**(10): p. 4200-4210.
55. Coutu, D., et al., *Lift-to-drag ratio and laminar flow control of a morphing laminar wing in a wind tunnel.* Smart Materials and Structures, 2011. **20**(3): p. 035019.
56. Manzo, J. and E. Garcia, *Demonstration of an in situ morphing hyperelliptical cambered span wing mechanism.* Smart Materials and Structures, 2010. **19**(2): p. 025012.
57. Dong, Y., Z. Boming, and L. Jun, *A changeable aerofoil actuated by shape memory alloy springs.* Materials Science and Engineering: A, 2008. **485**(1): p. 243-250.
58. Kim, H.-J., S.-H. Song, and S.-H. Ahn, *A turtle-like swimming robot using a smart soft composite (SSC) structure.* Smart Materials and Structures, 2012. **22**(1): p. 014007.
59. Wang, W., et al., *Locomotion of inchworm-inspired robot made of smart soft composite (SSC).* Bioinspiration & biomimetics, 2014. **9**(4): p. 046006.

60. Lagoudas, D., et al., *Constitutive model for the numerical analysis of phase transformation in polycrystalline shape memory alloys.* International Journal of Plasticity, 2012. **32**: p. 155-183.

61. Khan, A.S. and S. Huang, *Continuum theory of plasticity*. 1995: John Wiley & Sons.

62. Lagoudas, D.C. and Z. Bo, *Thermomechanical modeling of polycrystalline SMAs under cyclic loading, Part II: Material characterization and experimental results for a stable transformation cycle.* International Journal of Engineering Science, 1999. **37**(9): p. 1141-1173.

63. Lagoudas, D.C., et al., *Shape memory alloys, Part II: Modeling of polycrystals.* Mechanics of Materials, 2006. **38**(5): p. 430-462.

64. Peraza-Hernandez, E.A., D.J. Hartl, and R.J. Malak Jr, *Design and numerical analysis of an SMA mesh-based self-folding sheet.* Smart Materials and Structures, 2013. **22**(9): p. 094008.

65. Rosen, A. and O. Rand, *Numerical model of the nonlinear behavior of curved rods.* Computers & structures, 1986. **22**(5): p. 785-799.

66. Mueller, T.J. and J.D. DeLaurier, *Aerodynamics of small vehicles.* Annual Review of Fluid Mechanics, 2003. **35**(1): p. 89-111.

67. Torres, G.E. and T.J. Mueller, *Low aspect ratio aerodynamics at low Reynolds numbers.* AIAA journal, 2004. **42**(5): p. 865-873.

68. Pines, D.J. and F. Bohorquez, *Challenges facing future micro-air-vehicle development.* Journal of aircraft, 2006. **43**(2): p. 290-305.

69. Tucker, V.A., *Drag reduction by wing tip slots in a gliding Harris' hawk, Parabuteo unicinctus.* Journal of Experimental Biology, 1995. **198**(3): p. 775-781.

70. Tucker, V.A., *Gliding birds: reduction of induced drag by wing tip slots between the primary feathers.* Journal of Experimental Biology, 1993. **180**(1): p. 285-310.

71. Weierman, J. and J. Jacob. *Winglet design and optimization for UAVs*. in *28th AIAA Applied Aerodynamics Conference*. 2010.

72. Eppler, R., *Induced drag and winglets.* Aerospace science and Technology, 1997. **1**(1): p. 3-15.

73. Whitcomb, R.T., *A design approach and selected wind tunnel results at high subsonic speeds for wing-tip mounted winglets.* 1976.

74. Guerrero, J.E., D. Maestro, and A. Bottaro, *Biomimetic spiroid winglets for lift and drag control.* Comptes Rendus Mecanique, 2012. **340**(1-2): p. 67-80.

75. Nazarinia, M., M. Soltani, and K. Ghorbanian, *Experimental study of vortex shapes behind a wing equipped with different winglets.* Journal of Aerospace Science and Technology, 2006. **3**(1): p. 1-15.

76. Ning, A. and I. Kroo. *Tip extensions, winglets, and c-wings: conceptual design and optimization*. in *26th AIAA Applied Aerodynamics Conference*. 2008.
77. Takenaka, K., et al., *Multidisciplinary design exploration for a winglet.* Journal of Aircraft, 2008. **45**(5): p. 1601-1611.
78. Shelton, A., et al., *Active multiple winglets for improved unmanned-aerial-vehicle performance.* Journal of aircraft, 2006. **43**(1): p. 110-116.
79. Falcão, L., A.A. Gomes, and A. Suleman, *Aero-structural design optimization of a morphing wingtip.* Journal of Intelligent Material Systems and Structures, 2011. **22**(10): p. 1113-1124.
80. Gatto, A., P. Bourdin, and M. Friswell, *Experimental investigation into articulated winglet effects on flying wing surface pressure aerodynamics.* Journal of Aircraft, 2010. **47**(5): p. 1811-1815.
81. Bourdin, P., A. Gatto, and M. Friswell. *Potential of articulated split wingtips for morphing-based control of a flying wing*. in *25th AIAA Applied Aerodynamics Conference*. 2007.
82. Daniele, E., A. De Fenza, and P.D. Vecchia, *Conceptual adaptive wing-tip design for pollution reductions.* Journal of Intelligent Material Systems and Structures, 2012. **23**(11): p. 1197-1212.
83. Dayyani, I., et al., *The mechanics of composite corrugated structures: a review with applications in morphing aircraft.* Composite Structures, 2015. **133**: p. 358-380.
84. Du, H., et al., *Shape memory polymer S-shaped mandrel for composite air duct manufacturing.* Composite Structures, 2015. **133**: p. 930-938.
85. Fonseca, M., et al., *Shape memory polyurethanes reinforced with carbon nanotubes.* Composite Structures, 2013. **99**: p. 105-111.
86. Sankrithi, M.M. and J.B. Frommer, *Controllable winglets*. 2010, Google Patents.
87. Tajeddini, V. and A. Muliana, *Nonlinear deformations of piezoelectric composite beams.* Composite Structures, 2015. **132**: p. 1085-1093.
88. Tobalske, B.W., *Biomechanics of bird flight.* Journal of Experimental Biology, 2007. **210**(18): p. 3135-3146.
89. Lockwood, R., J.P. Swaddle, and J.M. Rayner, *Avian wingtip shape reconsidered: wingtip shape indices and morphological adaptations to migration.* Journal of Avian Biology, 1998: p. 273-292.
90. Tucker, V.A., *Gliding birds: the effect of variable wing span.* Journal of Experimental Biology, 1987. **133**(1): p. 33-58.
91. Fluck, M. and C. Crawford, *A lifting line model to investigate the influence of tip feathers on wing performance.* Bioinspiration & biomimetics, 2014.

9(4): p. 046017.

92. Henningsson, P. and A. Hedenström, *Aerodynamics of gliding flight in common swifts.* Journal of Experimental Biology, 2011. **214**(3): p. 382-393.

93. Hummel, D., *The aerodynamic characteristics of slotted wing-tips in soaring birds.* Acta Congressus Internationalis Ornithologici, 1980. **1**: p. 391-396.

94. Han, H., et al., *Buckling enhancement of epoxy columns using embedded shape memory alloy spring actuators.* Composite structures, 2006. **72**(2): p. 200-211.

95. Wang, W., et al., *Smart phone robot made of smart soft composite (SSC).* Compos Res, 2015. **28**(2): p. 52-57.

96. Ilievski, F., et al., *Soft robotics for chemists.* Angewandte Chemie, 2011. **123**(8): p. 1930-1935.

97. Rus, D. and M.T. Tolley, *Design, fabrication and control of soft robots.* Nature, 2015. **521**(7553): p. 467-475.

98. Gladman, A.S., et al., *Biomimetic 4D printing.* Nature materials, 2016.

99. Robinson, G. and J.B.C. Davies. *Continuum robots-a state of the art*. in *Robotics and Automation, 1999. Proceedings. 1999 IEEE International Conference on*. 1999. IEEE.

100. Jones, B.A. and I.D. Walker, *Kinematics for multisection continuum robots.* IEEE Transactions on Robotics, 2006. **22**(1): p. 43-55.

101. Crespi, A. and A.J. Ijspeert, *Online optimization of swimming and crawling in an amphibious snake robot.* IEEE Transactions on Robotics, 2008. **24**(1): p. 75-87.

102. Marchese, A.D., R.K. Katzschmann, and D. Rus, *A recipe for soft fluidic elastomer robots.* Soft Robotics, 2015. **2**(1): p. 7-25.

103. Seok, S., et al., *Meshworm: a peristaltic soft robot with antagonistic nickel titanium coil actuators.* IEEE/ASME Transactions on mechatronics, 2013. **18**(5): p. 1485-1497.

104. Kim, S., C. Laschi, and B. Trimmer, *Soft robotics: a bioinspired evolution in robotics.* Trends in biotechnology, 2013. **31**(5): p. 287-294.

105. Wehner, M., et al., *Pneumatic energy sources for autonomous and wearable soft robotics.* Soft Robotics, 2014. **1**(4): p. 263-274.

106. Bartlett, N.W., et al., *A 3D-printed, functionally graded soft robot powered by combustion.* Science, 2015. **349**(6244): p. 161-165.

107. Shepherd, R.F., et al., *Multigait soft robot.* Proceedings of the National Academy of Sciences, 2011. **108**(51): p. 20400-20403.

108. Martinez, R.V., et al., *Soft actuators and robots that are resistant to mechanical damage.* Advanced Functional Materials, 2014. **24**(20): p. 3003-3010.

109. Lee, Y., et al., *High-performance perovskite–graphene hybrid photodetector.* Advanced materials, 2015. **27**(1): p. 41-46.
110. Morin, S.A., et al., *Using "Click-e-Bricks" to Make 3D Elastomeric Structures.* Advanced Materials, 2014. **26**(34): p. 5991-5999.
111. Harrington, M.J., et al., *Origami-like unfolding of hydro-actuated ice plant seed capsules.* Nature communications, 2011. **2**: p. 337.
112. Kadolph, S.J. and S.B. Marcketti, *Textiles*. 2016: Pearson.
113. Spencer, D.J., *Knitting technology: a comprehensive handbook and practical guide*. Vol. 16. 2001: CRC Press.

국문 초록

형상 기억 효과를 활용한 소프트 모핑 섬유 구동기

한민우
서울대학교 공과대학원
기계항공공학부 기계공학전공

소프트 모핑 구조물은 유연한 메카니즘을 사용하여 기존의 강체 기반 구조물보다 효율적으로 생물체의 동작을 모사하는 것이 가능하다. 유연하고 환경에 순응가능한 특성은 생물체의 근육 움직임을 모사하는 것이 가능할 뿐만 아니라 단순한 구조물로도 다자유도의 움직임을 발생시킬 수 있다. 이러한 소프트 모핑 구동을 구현하기 위하여 본 연구에서는 직물과 편물 형태의 섬유를 기반으로 하는 소프트 모핑 직물 구동기를 제시하고자 한다.

먼저, 직조 형태의 지능형 연성 복합재료는 형상 기억 합금 와이어와 유리섬유가 직조된 직물 구조를 유연 기지 재료에 함침시킨 복

합재 형태의 구동기로 직물 구조의 치밀한 조직을 기반으로 하여 상대적으로 큰 변형을 발생시키는 것이 가능하다. 제작된 구동기는 직조된 형상 기억 합금 와이어에 선택적으로 전류 인가 조건을 달리하여 대칭/비대칭 구동을 발생시키는 것이 가능하다. 뿐만 아니라, 형상 기억 합금 와이어의 지름, 직조에 사용된 섬유의 비율, 유리섬유의 적층 조건과 같은 구동기의 구성 요소를 달리한 뒤의 구동 특성을 살펴보았다. 개발된 직조 형태의 지능형 연성 복합재료를 활용하여 자동차 축소 모델의 가변 후방 스포일러, 소형 무인항공기의 가변 윙렛의 형태로 제작하였다. 이들의 공력 특성을 확인하기 위한 풍동 실험을 수행하였으며, 풍속, 받음각, 구동 모드 등을 달리하여 발생하는 가변 날개의 특성과 효과를 측정하였다.

또한, 3차원 체적 변형을 포함한 다양한 구동 모드를 구현하기 위하여 지능형 편물 구동기를 개발하였다. 개발한 구동기는 구동을 보조하기 위한 파트 혹은 탄성 구조체 없이 섬유만으로 구성되었으며 일반적으로 사용되는 편물 제작 방식을 활용하여 대량 생산이 가능토록 하였다. 구동기의 제작에는 형상 기억 합금 와이어를 이종 섬유로 감은 형태의 지능형 섬유가 사용되었으며 이는 전류의 인가 혹은 외기의 온도에 반응하여 구동을 발생시키는 것이 가능하다. 개발된 지능형 편물 구동기는 편물 구조의 특성을 활용하여 복잡한 3차원 형태의 구조물로 제작이 용이하고, 편물 패턴에 따라 각기 다른 구동 모드를 발생시키는 것이 가능하다. 네 종류의 기본 편물 패

턴 (plain, garter, rib, and seed) 을 기반으로 총 14가지의 구동 모드를 개발하였으며, 이들 구동 모드를 조합하여 3차원 구조물의 구동 양상을 조절하는 것이 가능하였다. 본 연구에서는 네 종류의 꽃 (백합, 수선화, 통꽃, 칼라) 을 모사한 구조물을 제작하고 이들 꽃의 꽃잎을 전류 및 외기 온도로 제어하여 개화 동작을 모사가 가능하도록 구동기를 설계하였다.

주요어 : 지능형 유연 복합재 구동기, 스마트 섬유, 소프트 로봇, 인공 근육, 형상 기억 합금, 생체모사 구동기, 모핑 윙, 소프트 엑소 슈트

학 번 : 2013-30954